Abstract

Title of Dissertation: Integrated Measurement Technique To Measure Curing Process-dependent Mechanical And Thermal Properties Of Polymeric Materials Using Fiber Bragg Grating Sensors

Yong Wang, Doctor of Philosophy, 2009

Dissertation directed by: Professor Bongtae Han
Department of Mechanical Engineering

An innovative technique based on a fiber Bragg grating (FBG) sensor is proposed to measure the critical mechanical and thermal properties of polymeric materials. The properties include (1) chemical shrinkage evolution during curing, (2) modulus evolution during curing, (3) glass transition temperature (4) coefficient of thermal expansion (CTE), and (5) visco-elastic properties. Optimum specimen configurations are proposed from the theoretical analysis. Then an efficient numerical procedure is established to determine the material properties from the measured Bragg wavelength (BW) shift. The technique is implemented with various polymeric materials. The measured quantities are verified through a self-consistency test as well as the existing testing methods such as a warpage measurement of a bi-material strip, and a TMA measurement. The evolution properties obtained at a curing temperature are extended further by combining them with

the conventional isothermal DSC experiments. Based on the existing theories, the evolution properties can be predicted at any temperatures.

The proposed technique greatly enhances the capability to characterize the mechanical properties and behavior of polymeric materials. Since the specimen preparation is very straightforward, the proposed method can be routinely practiced and the measurement can be completely automated. It will provide a much-needed tool for rapid but accurate assessment of polymer properties, which, in turn, will enhance the accuracy of predictive modeling for design optimization of a microelectronics product at the conceptual stage of product development.

Integrated Measurement Technique to Measure Curing

Process-dependent Mechanical and Thermal Properties of

Polymeric Materials Using Fiber Bragg Grating Sensors

By

Yong Wang

Dissertation submitted to the Faculty of the Graduate School of the

University of Maryland, College Park, in partial fulfillment

of the requirements for the degree of

Doctor of Philosophy

2009

Advisory Committee:

Professor Bongtae Han, Chair/Advisor

Professor Avram Bar-Cohen

Professor Hugh Bruck

Assistant Professor Miao Yu

Professor Kyu Yong Choi

Acknowledgements

Table of Contents

List of Figures

Chapter 1 Motivation and Objective

Electronic packaging is a critical issue in the semiconductor industry, which determines the reliability and performance of electronic systems. It includes (1) the packaging of the integrated circuit chips, (2) the interconnections for signal and power transmission, and (3) the encapsulations for protecting the chips and interconnections from the environment. One of the key aspects behind electronic packaging is materials consideration, which pertains to the development of improved materials allowing more demanding packaging schemes to be possible [1].

Polymeric materials are involved in almost every aspect of the electronic packaging. The applications include but not limited to:

(1) In order to enhance the reliability of a flip-chip package, underfill material is used to redistribute the thermo-mechanical stress caused by the coefficient of thermal expansion (CTE) mismatch between the silicon chip and the substrate; the underfill materials are usually composed of epoxy resins and fused silica particles.

(2) For protection of semiconductor chips from external physical forces and external chemical forces, epoxy molding compounds (EMC) have been used extensively as an encapsulation, which are based on thermosetting polymers.

(3) As one of the alternatives for lead-bearing solders, electrically conductive adhesives are being widely employed. They are composites of electrically conductive fillers and polymeric matrices, normally based on epoxy resins, epoxy-phenolic resins, epoxy-silicone compositions, silicone resins, acrylic resins, or polyimides.

(4) Even in print circuit board fabrication, resins are largely used and the majority of them are thermosetting resins such as epoxies, polyimide, polyphenylene ether and polyester.

(5) Die attach materials are used between a silicon die and a substrate to provide mechanical support and thermal path. They consist of fillers and basic resins such as epoxy resins, polyimide, polyacrylate and silicone resins.

Since polymeric materials are so widely used, knowledge of the properties of those materials becomes critical, for the performance and reliability assessment as well as for the design optimization of electronic systems. Five representative examples are mentioned here.

(1) Although alleviating the stress on the solder material, the use of underfill materials can result in large stress on the silicon chip. The stress is induced by the chemical shrinkage occurred during curing and the CTE mismatch during cooling after curing, resulting in die crack in some cases. Its magnitude has been found to be strongly dependent on the underfill's CTE, modulus, chemical shrinkage and glass transition temperature (T_g). Therefore, accurate measurement of those properties is essential for the optimization purpose.

(2) Recently, the copper metallurgy and low-K interlayer dielectric (ILD) has been successfully implemented in small feature integrated circuits to increase device speed and reduce power consumption. The right choice of proper underfill material used in those products becomes extremely important since the underfill not only protects the solder joints by stress redistribution, but also protects the low-K ILD and its interface with the

silicon. Material properties including T_g, CTE, and modulus are needed for the selection guideline.

(3) In order to decrease the warpage in surface-mount packages, it is always desired to have an EMC material with small cure shrinkage and residual thermal shrinkage. In other words, an EMC system with a high T_g and low curing shrinkage is preferred. In addition, reducing the elastic modulus of an EMC at a high temperature above the T_g is also effective.

(4) In the printed circuit board (PCB) fabrication, higher T_g epoxies are commonly used. For thick board constructions, the use of higher T_g polymers lower z-axis expansion properties for enhanced plated via reliability. For thinner board constructions, the use of higher T_g polymers can achieve greater thermal stability to prevent sag during assembly. Unfortunately, polymers with higher T_g are usually more brittle and decrease mechanical performance and processibility. The development of advanced materials becomes necessary and the assessment of material properties is an inevitable step.

(5) In order to maintain the electrical conductivity during thermal cycling, conductive adhesives with high T_g is commonly used. This is because the metal particles move back and forth during the thermal cycling and the dielectric polymer matrix gradually flow to fill the area left behind the moving metal particles. As the number of thermal cycles increases, the contact resistance between adjacent particles increases and thus the interconnection joint resistance increases. Characterization of the properties of the polymers will provide guidance in the selection of a matrix material.

The testing methods for characterization of the mechanical and thermal properties of polymeric materials have been developed for many decades and some of them are

routinely practiced using commercially available instruments such as the thermo-mechanical Analyzer (TMA), the dynamic mechanical analyzer (DMA), the digital scanning calorimeter (DSC), the universal testing machine (UTM), etc. However, all the techniques focus on one or two properties of the material and different techniques are employed when different properties are to be measured. The specimen preparation and the testing conditions can be very critical to reliable and repeatable measurements by non-experts.

New polymeric materials are introduced every day, but less time is allowed to characterize them due to the shrinking product development cycle time. Design engineers cannot rely on the proprieties provided by polymer manufacturers since the testing conditions and other testing details associated with the properties are not always available. In addition, very limited material property data are available for new polymeric materials. Even in the case of well-known polymeric materials, the published property data can often vary by an order of magnitude. The significant variations in the published data are caused by inherent differences and the complexity involved in specimen preparation and testing procedures.

To cope with the above problems, an integrated measurement technique is proposed to measure the critical properties of polymeric materials. The method is based on a fiber Bragg grating (FBG) sensor and it can provide the material properties rapidly and accurately. Those properties include (1) chemical shrinkage evolution during curing, (2) modulus evolution during curing, (3) glass transition temperature, T_g, (4) coefficient of thermal expansion (CTE), and (5) visco-elastic properties. The proposed method is implemented with several different polymeric materials and the results are verified in

several aspects. The proposed technique is expected to be routinely practiced and the measurement can be completely automated.

Chapter 2 Background and Literature Review

2.1 Introduction

The existing techniques which measure the mechanical and thermal properties of polymeric materials are reviewed in this chapter. Those properties include chemical shrinkage, modulus evolution, coefficient of thermal expansion (CTE), glass transition temperature (T_g) and visco-elastic properties. The principle and implementation of fiber Bragg gratings (FBGs) in the measurement of strain or temperature is also reviewed. All of the information serves as the background for this study.

2.2 Chemical Shrinkage

Polymeric materials are those materials composed of molecules with very high molecular weight. Specifically, they can be divided into three categories: thermoplastic, thermoset, or elastomer [2]. Thermoplastics and un-vulcanized elastomers are uncrosslinked, whereas vulcanized elastomers and thermosets are cross-linked. Thermosetting polymers, which are the most commonly used polymeric materials in electronic packaging, solidify by being cured chemically. During the curing, the long macromolecules cross-link with each other, resulting in a network of molecules that can not slide past each other. As the curing progresses, volumetric shrinkage of a thermosetting polymer occurs because molecules move from a van der Waals distance of separation to a covalent distance of separation. This shrinkage induced by the curing is called chemical shrinkage. The specific volume change, v^{ch}, can be used to quantify the shrinkage which is defined as

$$v^{ch} = \frac{\Delta V}{V_0}$$ (2-1)

where ΔV is the volume change during the curing and V_0 is the original volume before the curing. Depending on the chemical composition and the polymerization reaction, the specific volume shrinkage can reach from 10% to 20% [3]. In mechanical modeling, *chemical shrinkage strain* is more straightforward to use and it can be expressed in terms of specific volume shrinkage as [4]

$$\varepsilon^{ch} = \sqrt[3]{1 + v^{ch}} - 1$$ (2-2)

where ε^{ch} is the chemical shrinkage strain and v^{ch} is specific volume shrinkage. When the chemical shrinkage is small, it can be approximated by the equation

$$\varepsilon^{ch} \approx \frac{v^{ch}}{3}$$ (2-3)

Since the chemical shrinkage strain can be thought of as a mechanical strain, residual stresses can be generated due to the curing of polymeric materials. This issue has interested electronic packaging researchers for several years and it has been identified to be important in some cases. When polymers are cured at high temperatures, the residual stresses developed in packages are usually believed to be negligible due to the small modulus of polymers. The phenomenon has previously been observed in several experiments [5-8]. However, when polymers are cured at low temperature especially below T_g, the modulus of cured polymers can be sufficiently large to considerable residual stresses. In 1996, Kelly etc. studied the behavior of EMC used in plastic quad flat packs (PQFP) and found that the chemical shrinkage can largely affect product's performance by inducing warpage and delamination [9]. In 2000, Yang etc. studied the curing process of underfills in flip-chip packages and concluded that neglecting the

7

chemical shrinkage induced stresses can result in an erroneous prediction for the position of a vertical die crack [10]. In 2001, Oota etc. studied the warpage of ball grid array (BGA) packages due to the curing shrinkage of EMC [11]. They established the small shrinkage strain as the guideline for choosing candidate materials. In 2005, Larson etc. studied the effect of residual compression, which is induced by the shrinkage of underfills, on the fatigue life of a package [12]. Interestingly, they found the underfill shrinkage can be a possible source for obtaining beneficial residual compression in solder grid array interconnects.

Except for the mechanical and reliability consideration, people are interested in measuring the chemical shrinkage of polymers because it affects the functionality. For example, electrically conductive adhesives contain polymeric matrices and conductive fillers. Normally, the adhesives exhibit low electrical conductivity before curing, but the conductivity increases dramatically after they are cured. This is because good conductivity is achieved during the curing process, mainly through intimate contact among conductive fillers caused by the shrinkage of polymer binder [13]. Accordingly, adhesives with higher curing shrinkage generally exhibit higher conductivity. Therefore, increasing the chemical shrinkage of a polymer matrix becomes a method for improving electrical conductivity of adhesives.

Although it can be fairly difficult, it is important to understand and measure the chemical shrinkage for development of new polymers and improvement of the performance of electronic packaging products. Figure 2.1 [14] illustrates the volumetric change of polymeric materials during a typical polymerization (curing) process.
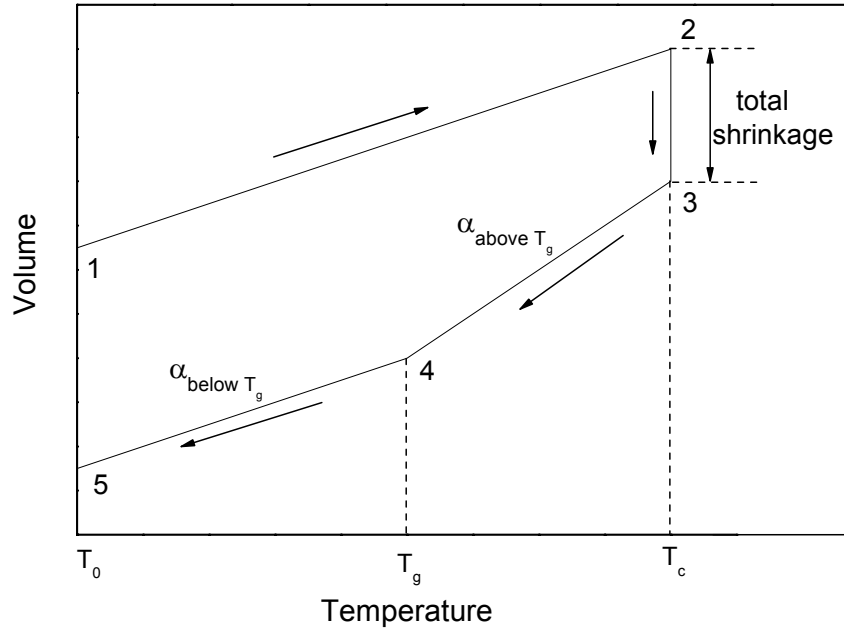
Fig. 2.1 Illustration of volumetric change of polymeric materials during a typical curing

process [14]

The temperature of the monomer or pre-polymer is ramped from the initial value T_0 to

the curing temperature T_c, and correspondingly the volume increases from point 1 to 2

due to the thermal expansion. During curing, the volume decreases from point 2 to 3

which is caused by the cross-linking. After the curing completes and temperature is

decreased back to the initial value, the volume of the cured polymer decreases from point

3 to 4, which happens above T_g, and then from point 4 to 5, which happens below T_g. In

the standard ASTM method, monomer or pre-polymer is poured into a mold with known

dimensions, heated to the curing temperature, cured, taken out of the mold, and measured

with the final volume [15]. In this way, ASTM method measures the volumetric change

before and after the curing at the initial temperature, which is the difference between

points 1 and 5 in Fig. 2.1. However, true polymerization induced shrinkage should be the

difference between points 2 and 3 which occurs at the curing temperature. Thus, strictly speaking, the result obtained by standard ASTM method incorporates the chemical shrinkage and thermal shrinkage and it does not represent the true chemical shrinkage. Instead, in-situ measurement of the shrinkage at the curing temperature should be utilized.

Numerous testing methods have been developed to measure the chemical shrinkage of polymeric materials. Russell studied the cure shrinkage of typical aerospace resins including Hercules 3501-6 epoxy, Hercules 8551-7A toughened epoxy and BASF 5250-4 bismaleimide using a pressure-volume-temperature (PVT) volumetric dilatometer [16]. A schematic drawing of the PVT dilatometer is shown in Fig. 2.2. The sample was enclosed in a piezometer cell and a stainless steel container closed off with flexible metal bellows and filled with mercury. The piezometer cell was placed in a pressure vessel. The hydrostatic pressure of silicone oil was produced in the vessel by a pump and was transferred to the contents of the piezometer cell by the bellows. The bellows expanded until the pressure in the vessel equaled the pressure in the cell. A linear variable differential transducer (LVDT) measured the length change of the bellows. And then the volume change of the sample was calculated using the cross-sectional area data of the bellows. In fact, the volumetric dilatometer is widely used to measure the cure shrinkage of polymers and numerous similar studies can be found [17-20]. The benefit of using a dilatometer is its capability of measuring volume change as functions of temperature and pressure. The drawback of volumetric dilatometers is that mercury which is used as the confining fluid in the dilatometers is highly toxic. In addition, the direct contact with fluid affects the curing of the polymers in the test.
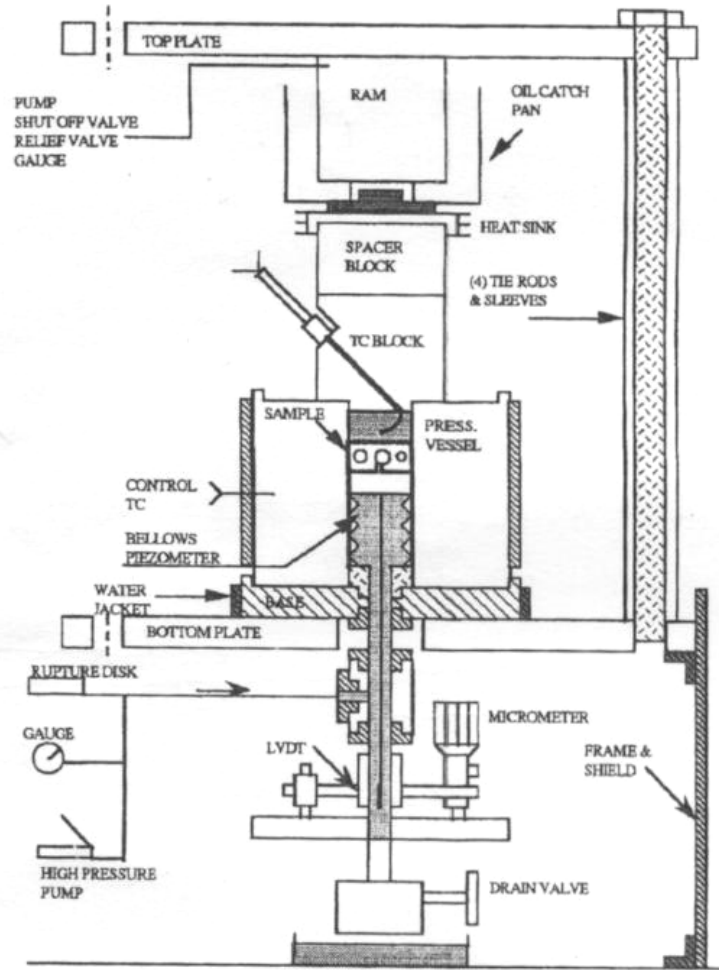
Fig. 2.2 Schematic drawing of a PVT apparatus [16]

Using a similar concept, Snow etc. designed a simple capillary and bulb mercury dilatometer for specific volume monitoring of polymeric materials during the curing [21]. A schematic drawing of the dilatometer is shown in Fig. 2.3.

The dilatometer consists of three main parts: a detached bulb, a graduated precision bore capillary, and a filling apparatus. In his experiment, dicyanate resin was immersed in the mercury and its volume was determined by subtracting the constant mercury volume from the sum of the capillary and bulb volumes. Bulb volume was

measured before the experiment and capillary volume was determined by the height of the mercury in the capillary. In addition to the drawbacks of a PVT volumetric dilatometer employed by Russell, this capillary dilatometer lacks of digital output, and the precision of the measurement is largely limited by the accuracy of visual observation.
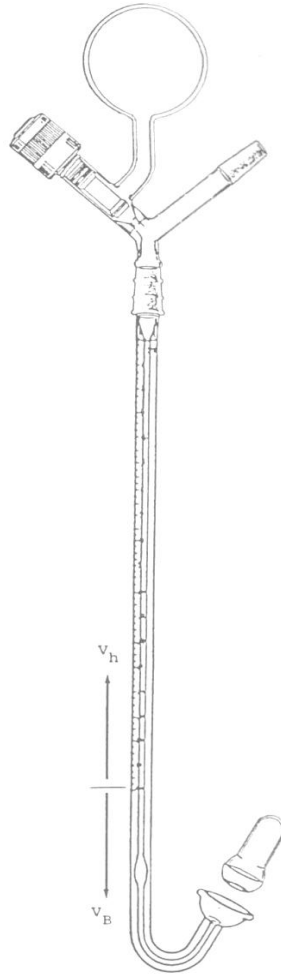
Fig. 2.3 Schematic drawing of a capillary and bulb mercury [21]

In 1997, Fano used a laser scanning micrometer to monitor the length of a polymer specimen during curing [22]. As shown in Fig. 2.4, a parallel scanning laser beam was sent onto the specimen and then collected by a photoelectric element. A

voltage was generated which corresponded to the intensity of the light. This voltage allowed the number of pulses generated while the beam was obstructed by the specimen to be counted. The number of the pulses was then determined by a counter which was proportional to the length of the specimen. Linear shrinkage strain was then calculated. Although this technique has high accuracy in the length determination, it only applies for light-cured polymers due to the complex optical setup.
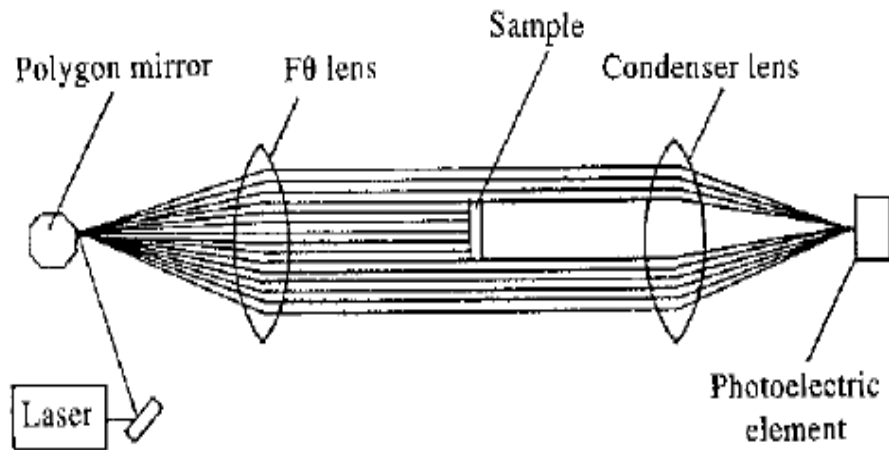
Fig. 2.4 Diagram of a laser scanning micrometer [22]

Cook etc. used a gas pycnometer to measure the shrinkage of dental composites [23]. They measured the volumes of specimens prior to and after photopolymerization, from which the total volumetric shrinkage was determined. The principle of a gas pycnometer is based on the ideal gas law. One can determine the volume of a specimen placed in the specimen chamber by measuring the pressure change of helium when helium under a known pressure in the pressurized expansion chamber is opened up to the specimen chamber. Cook studied four commercial dental composites and the volumetric

shrinkage was measured to be in the range between 1.6% and 2.5%. Compared with the liquid based dilatometer method, this technique is less labor intensive. However, the instrument does not have active temperature control system and it can not maintain the constant curing temperature. Each volume measurement usually takes more than ten minutes, which makes it impractical for real-time monitoring of the curing process.

Thomas used an optical fiber sensor to in-situ monitor the curing shrinkage during injection molding [24]. The experiment setup is illustrated in Fig. 2.5. The optical sensor, consisted of a bundle of optical fibers with a sapphire window at its end, was positioned in the ejector pin channel of the mold so that the sapphire window sat flush with the inside wall of the mold cavity. The optical view with this sensor was through the thickness (3.175 mm) of the molded polymer. The fiber bundle was divided into light excitation fibers and light collection fibers. Light from a helium neon laser was transmitted to the resin via the excitation fibers and light that reflected from any interface was detected. When the molded polymer shrank, it separated from the wall and sapphire window, and established the geometry of a Fabry-Perot interferometer. By counting fringes, the magnitude of movement of the molded polymer away from the mold wall was measured and then the shrinkage was determined. This method achieves the real-time monitoring. However, it is only suitable for transparent or translucent polymers and is not applicable for opaque materials.
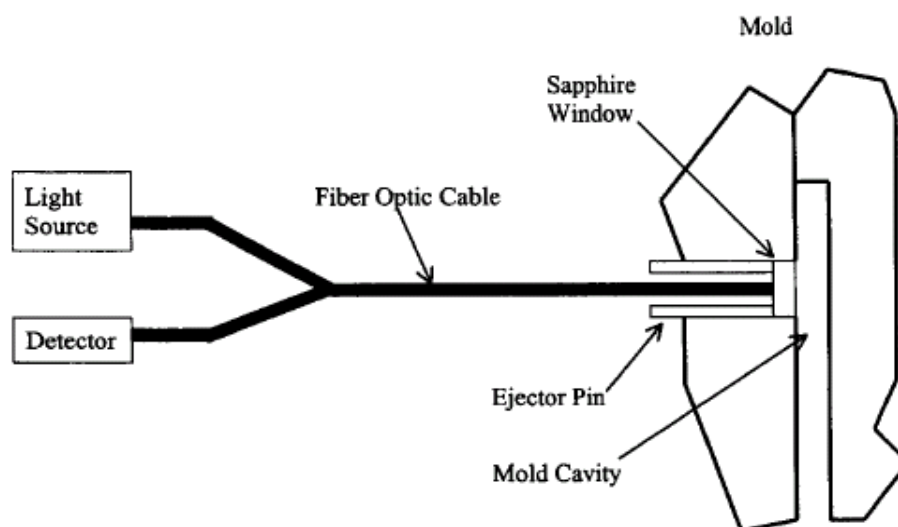
Fig. 2.5 Schematic drawing of the optical sensor and its connection to the mold, light

source and detector [24]

In 1999, Park built up a linometer which can measure the linear polymerization strain of polymers [25]. This method has been employed by other researcher such as Rosin [26]. The design of a linometer is illustrated in Fig. 2.6. In the experiment, the polymer was poured on the aluminum disk, which was coated with separating glycerin gel. The polymer was then covered with a slide glass and an aluminum shield. After the shield was covered and fastened under constant pressure, the position of the disk was adjusted to its zero position with the height adjustment. The amount of displacement of the disk was measured using an infrared micrometer and the linear strain was calculated. This setup achieved real-time monitoring. However, as noted by the designer, the measurement accuracy will be affected if the measuring time extends for hours because separation between the polymer and disk will occur.
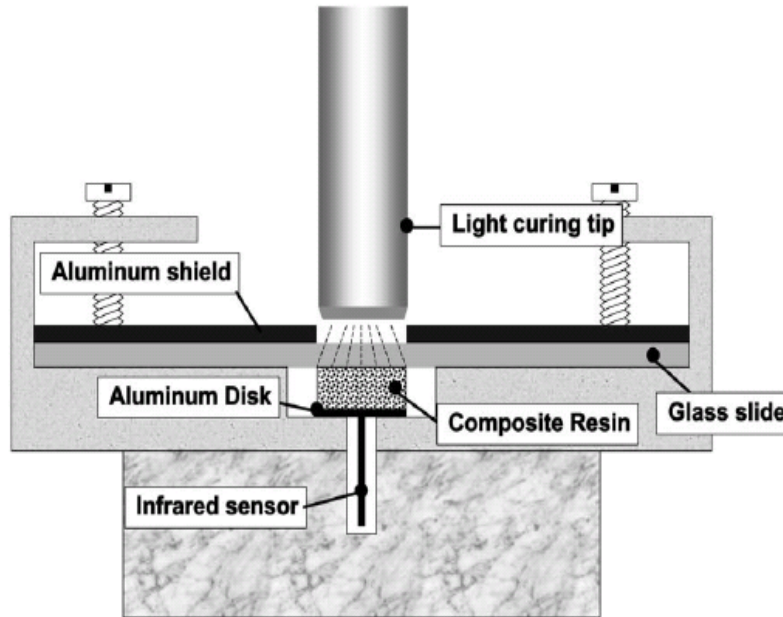
Fig. 2.6 Schematic diagram of a linometer [25]

Using the cross section analysis technique, Hudson etc. measured the shrinkage of UV-cured adhesives [27]. In the experiment, they dropped an uncured acrylic adhesive NOA 61 on a substrate which was a 500 um thick polished silicon wafer coated with a polymeric material. Then they recorded digital images of the adhesive drop before and after the curing. The curing scheme was exposure to UV-light with the intensity of 1000mW/cm^2 for 30 seconds. The result is shown in Fig. 2.7. In the image, 300 data points were collected around the periphery of a vertical section containing the axis of symmetry. They calculated the volume by rotating the image around the axis of symmetry and the volumetric shrinkage was determined to be 8.7%. This method enables the measurement of volumetric shrinkage of tiny amounts of UV-cured adhesives. However, it assumes the perfect symmetric drop shape, and the uncertainty in the volume determination could be fairly large due to the possible asymmetry of the drop shape.
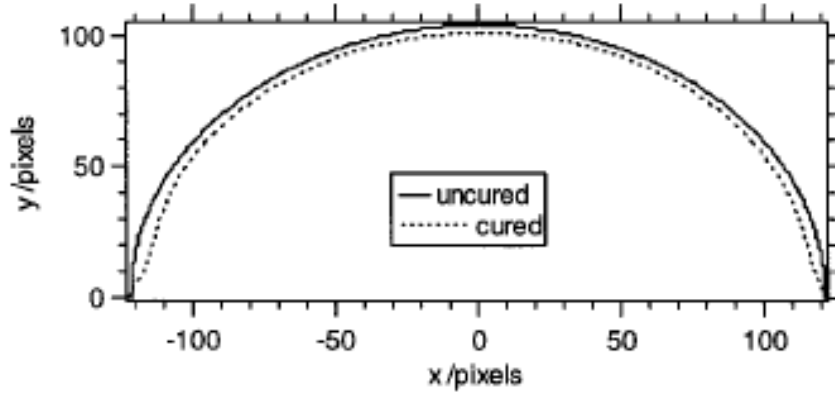
Fig. 2.7 Profile of the adhesive drop before and after cure [27]

Li etc. measured the curing shrinkage of MY750 epoxy using a buoyancy monitoring technique [14]. As shown in Fig. 2.8, the sample material was sealed in a thin-walled silicone bag and cured in a silicone fluid bath at a controlled constant temperature and weighted independently of the bath. The buoyancy of the sample was monitored as its density increased with respect to the constant density fluid during isothermal cures. By measuring the apparent weight of the sample, they calculated the buoyancy which was proportional to the sample volume and deduced the volumetric shrinkage through the equation

$$\left(\frac{\Delta V}{V}\right)_{shrinkage} = \frac{\Delta G}{\rho_{silicone} \times V_0} \tag{2-4}$$

where ΔG is the change in the apparent weight of resin weighted in the fluid bath at the curing temperature, $\rho_{silicone}$ is the density of the silicone fluid at the cuing temperature and V_0 is the volume of uncured resin. The shrinkage was found to be 6.9%. This technique is sensitive to the shrinkage since a high precision balance can weight tiny

change of apparent weight. However, it is also sensitive to air bubbles attached to the resins surface or the suspending wire which can result in errors. Residual solvent, dissolved air and volatile byproducts are all also detrimental to the measurement.
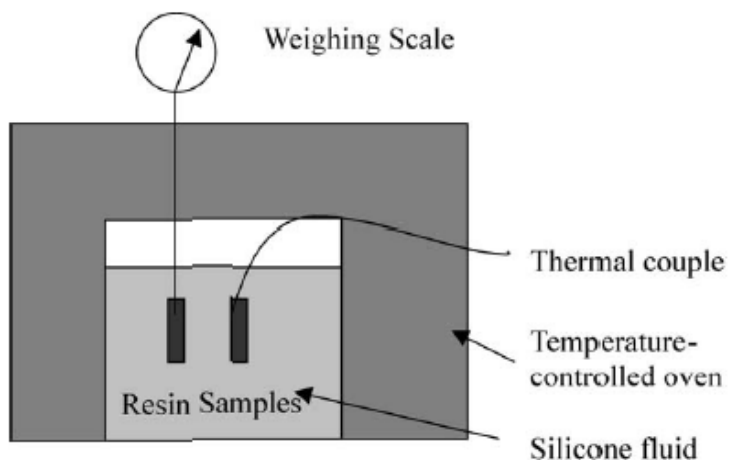
Fig. 2.8 Setup for measurement of shrinkage by monitoring buoyancy [14]

Most recently, Yu etc. studied the chemical shrinkage of two epoxy-based NCA materials XS8436 and FP4549 by the use of a Thermo-mechanical Analyzer (TMA) [28]. They sandwiched the epoxy between two silicon slides and measured dimension change of the epoxy during the curing with a TMA. The experiment setup is illustrated in Fig. 2.9. The total shrinkage was determined to be 3.71% and 5.42% respectively. The benefits of this method include easy sample preparation and instrument operation. However, it requires highly uniform thickness of the polymer layer between silicon slides, and the contact force applied by the TMA probe becomes a critical factor. A too small force will result in lost contact, while a too large force will apply undesired mechanical loading to the epoxy and thus affect the results.
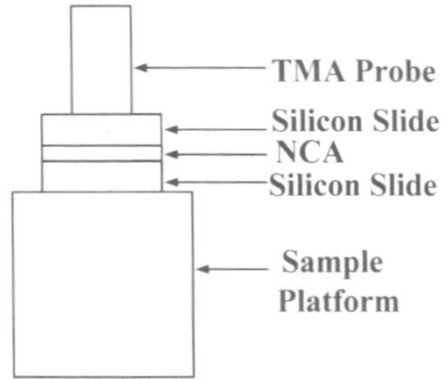
Fig. 2.9 Schematic diagram of cure shrinkage testing system by means of TMA [28]

Except for those volumetric techniques, there is a non-volumetric technique which determines the cure shrinkage based on the measurement of polymer laminates warpage. It was firstly proposed by Daniel [29] and then used by Aggelopoulos [30] and Karalekas [31]. The basic concept of this technique is coating a pre-polymer layer on an identical layer of the same material that has already been cured. Then the laminate is cured and the resulting warpage is recorded by means of shadow moiré. Figure 2.10 shows representative moiré patterns [29]. Assuming the modulus and Poisson's ratio of two layers are the same, the shrinkage in the pre-polymer layer is found to be simply related to the measured warpage through the following equations:

$$e_1^c = -\frac{8hw}{3a^2} \qquad e_2^c = -\frac{8hw}{3b^2} \qquad (2\text{-}5)$$

where e_1^c and e_2^c are shrinkages in two perpendicular directions, w is the measured warpage, h is the thickness of each layer and a, b are the length of semi-axes of the elliptical fringe.
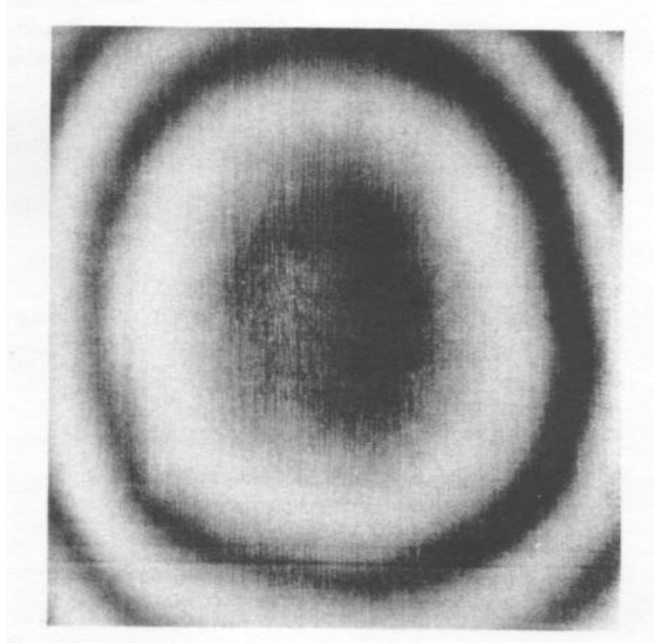
Fig. 2.10 Moiré pattern for laminate made of a pre-cured and an uncured layer [29]

In Daniel's work, the chemical shrinkage of a woven E-glass fabric impregnated with an epoxy/epoxy-novolac system was found to be 0.0154% and 0.0278% in two directions. In Karalekas's work, an isotropic shrinkage strain of 0.448% for an acrylic-based photopolymer was obtained. This technique has an obvious advantage of measuring linear shrinkage in two different directions. However, the drawback is also obvious, i.e., it is assumed that mechanical properties are the same in two layers. In fact, the properties of the uncured layer are actually changing during the curing and this assumption only holds at the end of the curing.

It should be noted that all of the methods listed above only measure the total (intrinsic) chemical shrinkage and cannot detect the gelation point. The gelation point is defined as the conversion at which an infinite molecular network is formed [32] and the polymer has apparent elastic properties [33]. As a result, when calculating the curing

induced residual stresses in the assembly, only the chemical shrinkage that occurs after the gelation point should be used instead of the total one. This effect is clearly shown in Stolov's experiment [34]. In his experiment, a UV-cured acrylic monomer was coated on a steel cantilever. After applying the radiation, warpage of the cantilever and curing extent of the polymer were monitored simultaneously. By the measured warpage, stress buildup in the polymer layer was determined through the beam theory. Results of measured accumulated stress and curing extent are plotted in one chart as shown in Fig. 2.11. No stress buildup is observed before the gelation point and it increases dramatically after gelation. We define the portion of intrinsic chemical shrinkage that contributes to the accumulation of residual stresses as the "*effective chemical shrinkage*".
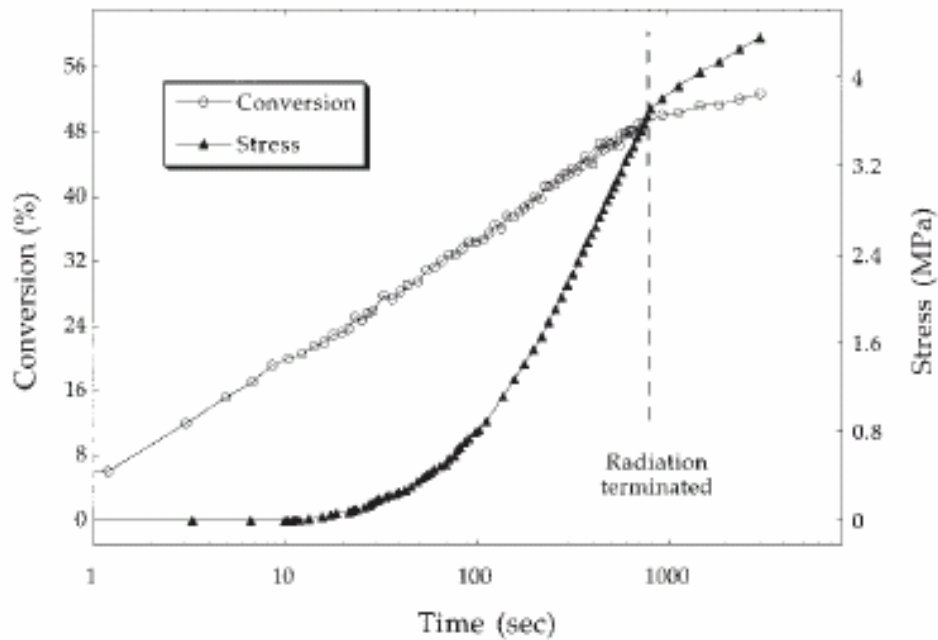
Fig. 2.11 Stress build-up vs. curing extent [34]

All the methods listed above cannot detect the gelation point. In order to obtain the effective chemical shrinkage, an auxiliary experiment is needed for the determination

21

of gelation point. A Fourier Transform Infrared Spectroscopy (FTIR) [14] or a Dynamic Mechanical Analyzer (DMA) [28] has been employed to detect the gelation point, respectively. It should be noted that more experiments mean more complexity, and moreover, the time correlation in separate experiments is extremely difficult. In this regard, a technique which can directly measure the effective chemical shrinkage evolution is highly desired.

2.3 CTE and Glass Transition Temperature

As one of the most important thermo-mechanical properties of polymeric materials, the *coefficient of thermal expansion* (CTE) relates the volume changes that occur in a polymer to the temperature variation. Normally, the polymer volume V increases with increasing temperature as a result of the increasing atomic motions resulting from the added energy. The *coefficient of volumetric thermal expansion β* is defined as the fractional rate of change of V as a function of temperature T, which can be expressed as

$$\beta(T) = \frac{1}{V(T)} \left[\frac{\partial V(T)}{\partial T} \right]_P \qquad (2\text{-}6)$$

Here partial derivative is used because V is also a function of the pressure. The *coefficient of linear thermal expansion, α* is another useful quantity which is more commonly quoted in the literature. It simply equals to one third of the coefficient of volumetric thermal expansion for an isotropic material

$$\alpha = \frac{\beta}{3} \qquad (2\text{-}7)$$

Unless specifically stated, the CTE in this study means the coefficient of linear thermal expansion, α.

Typical polymer volume variation with temperature is shown in Fig. 2.12 [35].
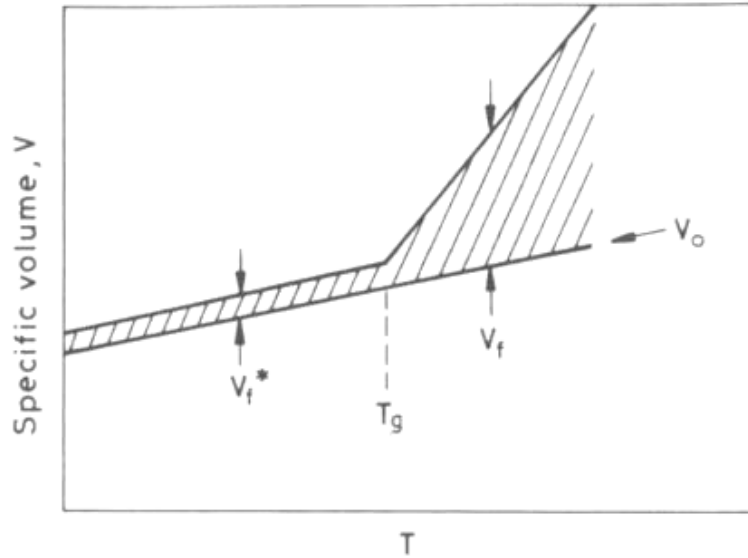
Fig. 2.12 Scheme of the variation of polymer volume with temperature [35]

As it is shown in the figure, the CTE of a polymeric material manifests a dramatic and discontinuous change when temperature is above a certain value. This particular temperature is called *glass transition temperature* (T_g) and it can be defined as the temperature at which the forces holding distinct segments together are overcome by thermally-induced motions and large scale cooperative motions of chain segments become possible [36]. The CTE of a polymer increases dramatically when temperature increases beyond T_g (in the rubbery state). The phenomenon can be explained by the free volume theory. Generally, the volume of a material, V, is the sum of the volume occupied by the molecules, V_0, and the free volume, V_f, which is the space not occupied by molecules [35]. The free volume is sensitive to changes in temperature and the

thermal expansion of polymers can be attributed to a change in free volume. When the temperature decreases from high to low, the free volume shrinks until it is too small to allow long-range cooperative motions and the temperature at this point is T_g. Below T_g only local conformational changes are permitted and consequently the free volume shows negligible temperature dependence. This phenomenon is also schematically shown in Fig. 2.12 [35]. The free volume, V_f, is represented by the shaded area and it can be seen that V_f remains constant below T_g and increases with temperature above T_g.

In electronic packaging, characterization of the CTE of a polymeric material is critical as it is required for the assessment of the reliability of a packaging product under thermal loadings. Different components in a package have different CTE values. For example, a silicon chip has a CTE of 2.5 ppm/°C; copper pad has a CTE of 17 ppm/°C; a ceramic substrate has a CTE ranging from 4 to 10 ppm/°C while an organic substrate has a CTE ranging from 18 to 24 ppm/°C; the solder material has a CTE ranging from 22 to 26 ppm/°C [13]. The CTE mismatch among different components can induce large stresses when subjected to temperature variation. In design considerations, polymers such as underfills and EMC with appropriate CTE and T_g should be used for optimum stress management. In a polymer/substrate bi-material joint, the residual stress due to a temperate change from T_0 to T can be approximately calculated as [13]

$$\sigma = \left(\alpha_1 - \alpha_i\right) E_1 \left(T_g - T\right) + \left(\alpha_2 - \alpha_i\right) E_2 \left(T_0 - T_g\right) \qquad (2\text{-}8)$$

where α_1 and α_2 are CTE of the polymer at below and above T_g and α_i is the CTE of the substrate. As shown in Eqn. (2-8), CTE plays an important role in the residual stress magnitude.

Three testing techniques are commonly used to measure the CTE of polymeric materials. They are quartz dilatometer, vitreous silica dilatometer and interferometer dilatometer [37].

Thermo-mechanical Analyzer (TMA) is the most popular tool used for the measurement of CTE [ASTM E831] and it is a quartz dilatometer. A schematic diagram of a TMA is shown in Fig. 2.13. It consists of a stage which supports the specimen and a quartz probe that moves vertically. The quartz probe is essentially a displacement sensor and a small force of 1 to 100 mN is applied to keep the probe in contact with the specimen. The temperature of the specimen is controlled by the oven. The CTE of the specimen can be calculated by

$$\alpha = \frac{1}{L_0} \frac{\Delta L}{\Delta T} \qquad (2\text{-}9)$$

where L_0 is the initial height of the specimen, ΔL is the change in height due to a temperature change ΔT.
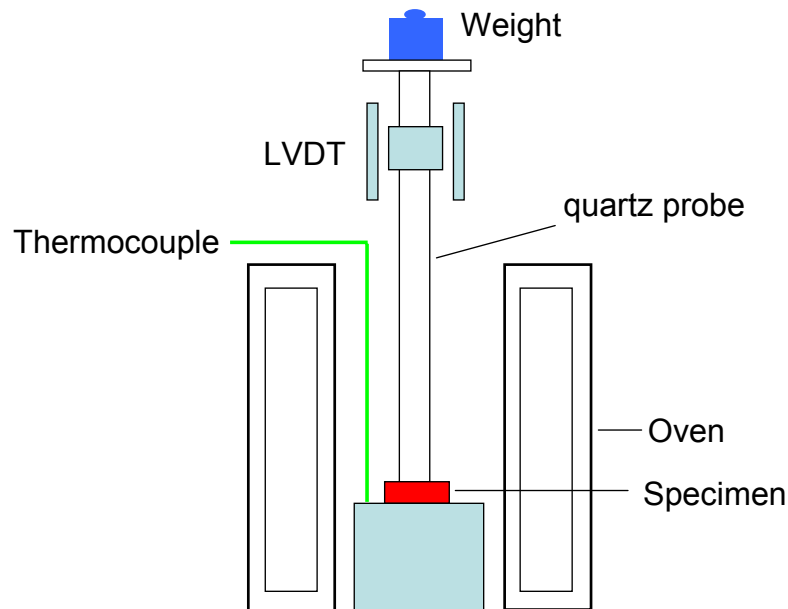
Fig. 2.13 A schematic diagram of TMA equipment

The CTE can also be measured using a silica dilatometer [ASTM E228]. As it is illustrated in Fig. 2.14, a specimen is placed inside a silica tube and a silica rod is inserted into the tube. A dial gage is attached to the rod for detection of the position. The CTE of the specimen is determined using Eqn. (2-9).
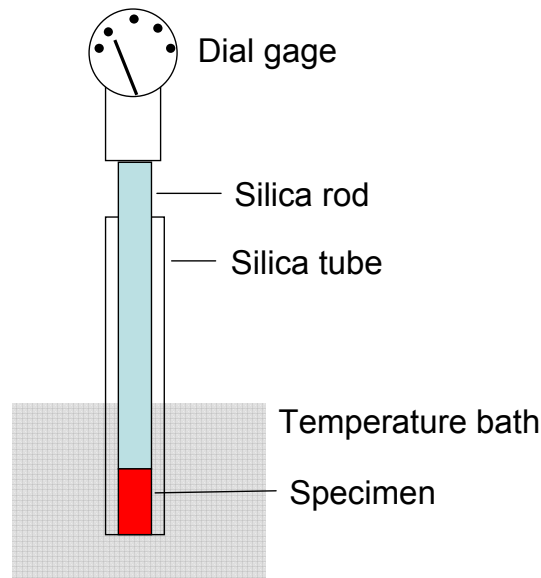
Fig. 2.14 A schematic diagram of a silica dilatometer

An interferometer dilatometer is schematically shown in Fig. 2.15 [38]. Basically, it includes the following modules: a gas chamber with a specimen support, an inductive heating device with a radio frequency (RF) power generator, a coil and so-called robber rings, a gas shower for cooling the sample, a double-beam differential laser interferometer with two light guide push rods, and a control and data acquisition unit. The laser beam is reflected at the bottom inner surface of the push rods. Elongation of the push rods will change the optical path which is detected by the interferometer. The interferometer is a miniature double-plane mirror interferometer comprising two Michelson interferometers with a common He-Ne laser source, which are provided via

two single mode fiber optic cables. Similar interferometer dilatometer setup can be found in the literature [39-41]. The optical dilatometer has a high resolution in detecting the optical path change. Unfortunately, the temperature change of the air also changes the optical path length because the refractive index the air changes with the temperature. As a result, the measurement resolution is greatly deteriorated.
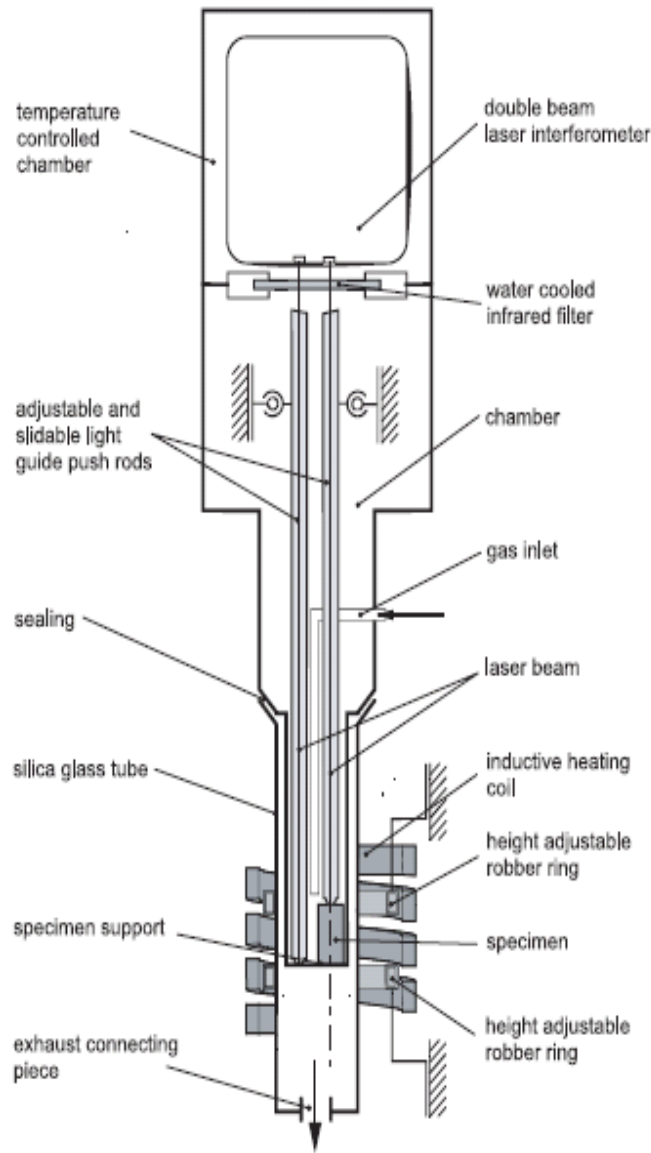
Fig. 2.15 A schematic diagram of an interferometer dilatometer [38]

Understanding T_g of a polymeric material is important especially when evaluating a new material. This fact can be more clearly explained by the following several examples.

The glass transition temperature, T_g, of the resin is an important characteristic for printed wiring boards (PWB). In general, the higher the T_g, the smaller z direction expansion when a PWB is heated. That reduces stress on plated through holes during processing and improves board reliability. Besides, the higher the T_g, the less possibility of rework which results in pads or lines detaching from the surface of the PWB and the less measling (separation of resin from glass weave due to differential expansion of the glass and the resin) is generated.

As the IC fabrication moves towards small feature and high density, interlayer dielectric (ILD) materials have been developed and successfully implemented together with copper metallurgy to increase device speed and reduce power consumption. These low-K materials tend to be porous and brittle and are protected by underfills. Tsao evaluated several underfills for the low-K flip chip package and found that only moderately low T_g underfills (T_g between 70 and 120 °C) can effectively protect both the solder joints and low-K interface [42]. In this case, T_g of the underfill becomes a very important index.

Anisotropically conductive film (ACF) is used in the flip-chip bonding. Reliability results indicate that the ACF possessing an adhesive matrix with a high T_g (282 °C) exhibits high reliability [13].

There are several methods which can be used to determine the glass transition temperature of a material. The most common technique reported in the literature is differential scanning calorimetry (DSC) which is shown schematically in Fig. 2.16 [43]. It monitors the difference between a reference and a sample during a controlled temperature change. Changes in the heating rate of the sample relative to the reference can then be converted into specific heat and enthalpy changes. T_g is determined at the inflection point of the specific heat curve. An example of using DSC to determine T_g of polymers can be found in Wong's work [44].
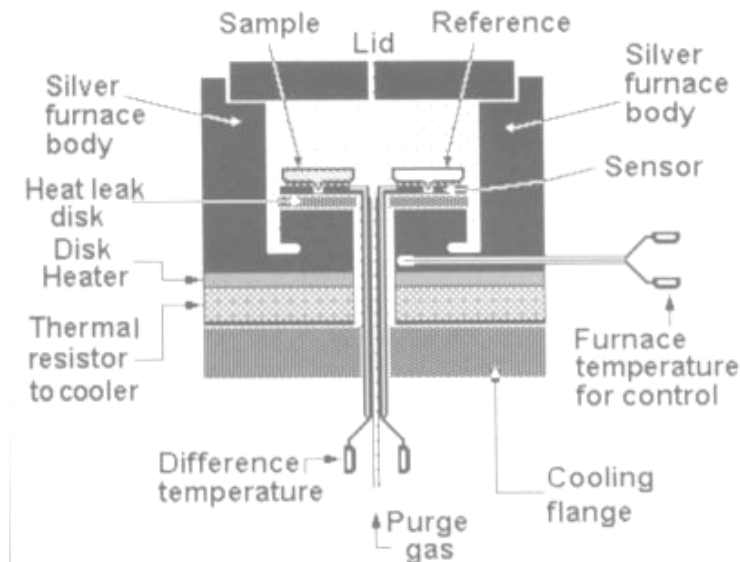
Fig. 2.16 A schematic drawing of a DSC [43]

TMA can be also employed to determine T_g. As previously discussed, the CTE of a polymeric material undergoes a dramatic and discontinuous change at T_g. Using the measured displacement-temperature curve, T_g is determined at the inflection point as

illustrated in Fig. 2.12. An example of using TMA to measure T_g of epoxy resins for PCB application can be found in Yung's work [45].

Excluding specific heat and CTE, other properties such as refractive index and dielectric constant also change considerably at T_g. Based on that, a refractometry or a dielectric relaxation spectroscopy can be used to detect T_g which essentially measures the refractive index and dielectric constant of a material, respectively [36].

2.4 Modulus Evolution

The modulus, E, is one of the most important mechanical properties of a material. It is the key indicator of the stiffness, and it quantifies the resistance of a material to mechanical deformation and the ability to store deformation energy. To measure the modulus of a polymer material, the simplest method is using a universal testing machine (UTM), which applies and monitors the loading to the standard dumbbell-shaped test specimen, together with an extensometer which determines the strain. A schematic drawing of a UTM can be found in Fig. 2.17. The specimen dimension and the testing rate are important and they can be found in ASTM D638 and ASTM D882 which are recommended for polymers [46]. An example of the measuring modulus by the use of UTM can be found in Jasso's paper [47]. In his work, the author obtained the Young's modulus of a gradient polymer which was polystyrene (PS)/ poly butyl acrylate (PBA).

Crosshead travel limit switches
Fixed crosshead load cell mounting position
Adjustable upper-limit stop
Extension measuren optical encoder (optional)
Leadscrew cover
Limit switch rod
Strain-gage extensometer connector
Leadscrew
Crosshead preload nuts
Load cell
Manual positioning resolver
Flexible coupling
Moving crosshead
Adjustable lower-limit stop
Base testing adapter
Grips
Crosshead manual positioning control
Resolver
Drive motor
Clutch driver board
Connector box
Leadscrew drive gear
Gearbox
Leveling pad
Gearbox output pinion gear and torsion testing adapter

Fig. 2.17 A schematic drawing of a UTM [48]

The polymerization process of polymers is a dynamic process and the properties of polymers evolve as the polymerization proceeds. Generally, polymers start from a liquid or gel state and gradually solidify at the curing temperature. Their modulus evolves from virtually zero at the gelation point to the final value at the end of curing. To predict the residual stresses induced by polymerization, one cannot simply use the final modulus in the calculation and the knowledge of modulus evolution is a prerequisite. The theoretical base lies in the following. It is generally hypothesized that an increment of curing induced strain, $d\varepsilon$, contributes to the stress after completion of the process

31

according to Hooke's law [49]. In the case of uni-axial condition, stress increment can be calculated as

$$d\sigma = E(t)d\varepsilon \qquad (2\text{-}10)$$

where E is the modulus at the time of the strain increment. Then the total stress σ can be obtained by integrating Eqn. (2-10) over the curing process

$$\sigma = \int E(t)d\varepsilon \qquad (2\text{-}11)$$

As it can be seen from Eqn. (2-11), evolution of the modulus is needed for the calculation of curing induced residual stress.

An UTM cannot be used to measure the modulus evolution of polymers during curing simply because the specimen cannot be clamped in the gel state. As a solution, a rheometer or a Dynamic Mechanical Analyzer (DMA) has been employed to measure the shear modulus evolution, and they are the only techniques available in the literature.

A rheometer is a mechanical spectrometer that is capable of subjecting a sample to either a dynamic (sinusoidal) or steady (linear) shear strain. A schematic drawing of a rheometer is shown in Fig. 2.18 [50]. It comprises several parts including: 1 - rotation drive, 2 – reducer, 3 – angular velocity transducer, 4 – inner (rotating) cylinder, 5 – outer (fixed) cylinder and 6 – torque transducer. A rheometer measures the resultant torque expended by the sample in response to the shear strain (shear strain is applied by the motor and torque is measured by the transducer) either in dynamic or steady mode. In the dynamic mode, the motor begins all tests at the motor zero position, and drives symmetrically about motor zero to the strain as specified. In the steady mode, the motor can begin a test from any position, rotating either clockwise or counterclockwise as specified. Adolf used a rheometer to measure the shear modulus evolution of Epon 828

epoxy [51]. Dynamic scan was applied to the specimen and the modulus was measured as a function of time at the curing temperature of 90 °C. In the experiment, a fixed frequency of 1 rad/s is used.
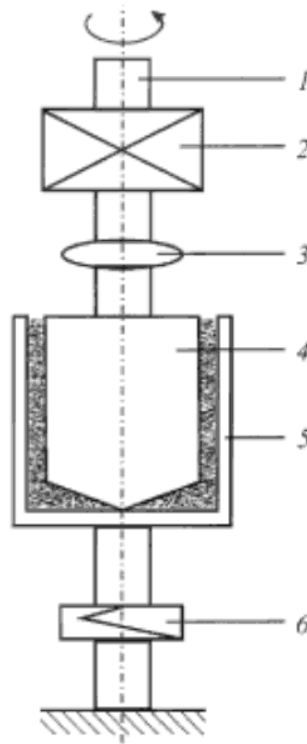
Fig. 2.18 A schematic drawing of a rheometer [50]

Dynamic Mechanical Analyzer (DMA) is more commonly used to measure the shear modulus evolution of polymers during curing. Lange studied the curing behavior of a thermosetting material using a DMA [49]. They applied the monomer between two plates of the DMA and cured it at 140 ºC. During the polymerization, the shear modulus was measured as a function of the curing time as the DMA worked in the torsion mode. The result is shown in Fig. 2.19. As shown in the figure, the modulus increases dramatically after the gelation point. Similar work can be also found in Eom's [52] and

Markovic's [53] papers, where the shear modulus evolution was measured during curing for FGDDM epoxy and phenol-formaldehyde novolac resins, respectively.
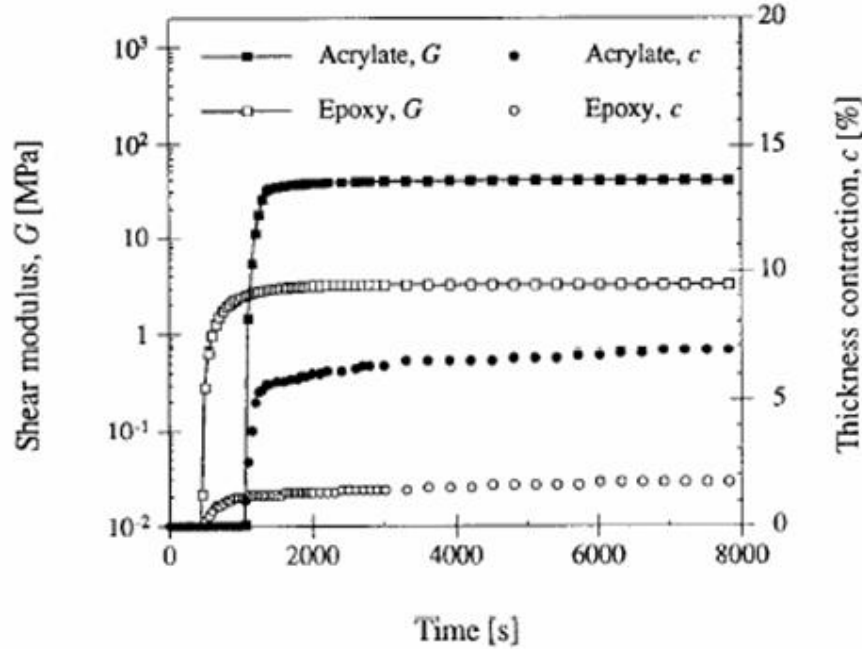
Fig. 2.19 Evolution of shear modulus as a function of curing time obtained by DMA [49]

In the above, instead of the Young's modulus, only evolution of the shear modulus is measured because of the incapability of the instruments. In addition, the techniques are difficult to implement for the evolution property measurement. A new technique needs to be developed for the measurement of Young's modulus evolution.

2.5 Visco-elastic Properties

Polymers exhibit both elastic and viscous characteristics when subjected to deformation. The elastic approximation often overestimates the stresses [54-56] and it is important to quantify visco-elastic properties of polymers for quantitative mechanical

34

analysis. There are two categories of experimental methods for measurement of the visco-elastic properties of polymers: static and dynamic [57]. Static testing is used to characterize a polymer's behavior when it is subjected to a sudden load. Both creep and stress relaxation testing belong to this category. In dynamic testing, a sinusoidal loading is applied to the specimen and the time dependence of the polymer's behavior can be characterized by varying the frequency. Generally, the static testing is a long-term method whereas the dynamic testing is for a short-term range.

A creep testing consists of measuring the time dependent strain, $\varepsilon(t)$, resulting from the application of a constant uni-axial stress, σ_0, as illustrated in Fig. 2.20a. The time dependent compliance, C(t), can be determined as

$$C(t) = \frac{\varepsilon(t)}{\sigma_0} \tag{2-12}$$

If the compliance is independent of the applied stress magnitude, then the polymer is said to be linear visco-elastic. Otherwise, the polymer is nonlinear visco-elastic. Normally, polymers exhibit linear visco-elastic behavior at low deformation levels (strain below ~ 0.5% [58]). In this study, only linear visco-elasticity is covered.

(a)   (b)
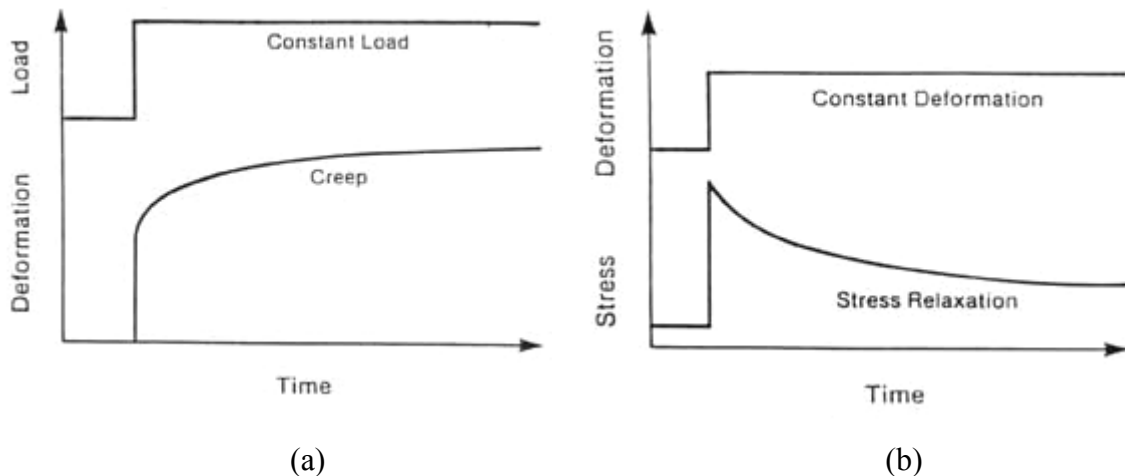
Fig. 2.20 Illustration of (a) creep testing and (b) stress relaxation testing

A creep testing station is illustrated in Fig. 2.21 [59]. It consists of clamping devices for the specimen, loading system, strain measuring system and low-friction guide to ensure axial loading. The clamping device is arranged so that the major axis of the test specimen coincides with the direction of pull force. The loading system is designed to achieve rapid but shock-free loading.
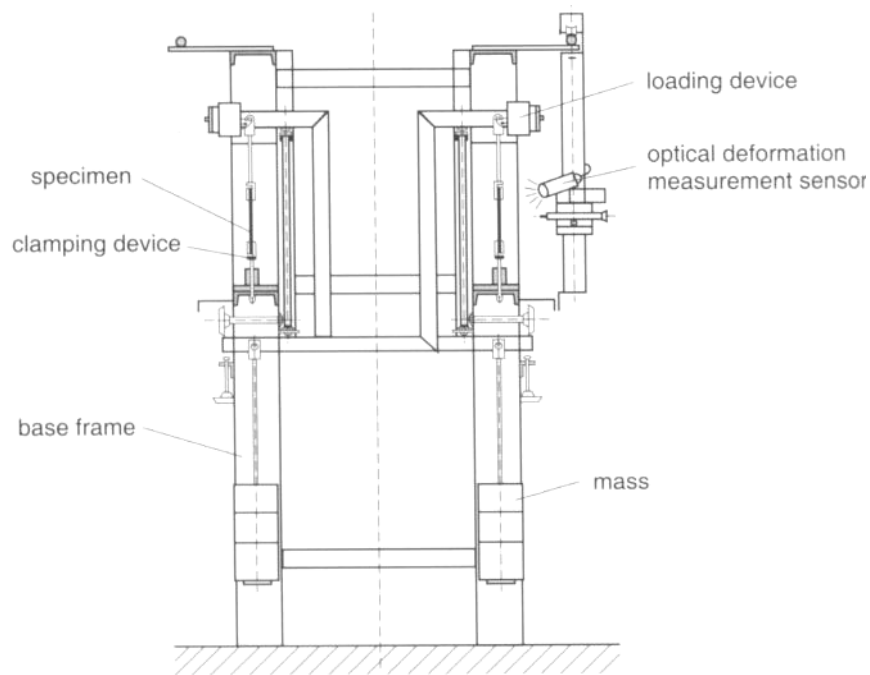
Fig. 2.21 Scheme of a creep testing apparatus [59]

The alternative step-function experiment is stress relaxation testing. The general concept of a stress relaxation experiment is illustrated in Fig. 2.20b and a schematic drawing of a stress relaxation testing station is shown in Fig. 2.22 [35]. The specimen is connected in series with a spring with sufficient rigidity. The spring undergoes negligible deformation in comparison with that of the sample. A steady strain, ε_0, is applied to the specimen instantaneously. The clamps then maintain the deformation of the sample and a

strain gauge associated with a spring element is used to record the resulting time-dependent stress, σ(t).
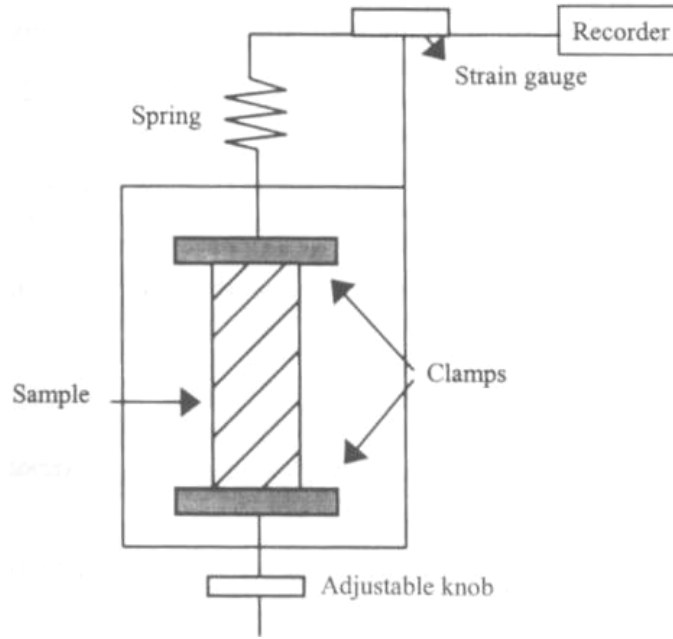
Fig. 2.22 Scheme of a stress relaxation apparatus [35]

The relaxation modulus, $E(t)$, is defined as

$$E(t) = \frac{\sigma(t)}{\varepsilon_0}$$

(2-13)

During the test, the temperature of the sample is controlled by a thermostatic device. Conducting the stress relaxation experiment at various temperatures will yield the time and temperature dependent relaxation modulus.

Both creep and relaxation are manifestations of the same molecular mechanisms and they can be related by the convolution integral [55, 60]

$$\int_0^t C(t-\tau)E(\tau)d\tau = \int_0^t E(t-\tau)C(\tau)d\tau = t$$

(2-14)

From the above equation, one can solve an integral equation to obtain a creep function from a relaxation function, or vice versa.

The temperature has a dramatic influence on the rate of visco-elastic response of polymers. With the assumption of *thermorheologically simple*, the relation between time and temperature can be described by simple models. In this case, the effect of lowering the temperature is simply to shift the creep compliance or relaxation modulus curve (plotted against log time) to the right without change in shape. It is also called the time-temperature superposition principle. A time-temperature shift factor $a_T(T)$ can be defined as the horizontal shift that must be applied to a response curve, for example, $C(t)$, measured at an arbitrary temperature T to obtain the curve at some reference temperature T_{ref}. It can be expressed mathematically as

$$\log(a_T) = \log\left(t(T)\right) - \log\left(t(T_{ref})\right) \tag{2-15}$$

Two mathematical functions are generally used to model the shift factor, a_T. The first one is called Arrhenius relationship, and it can be expressed as

$$\log\left(a_T\right) = \frac{\Delta H}{2.303R}\left(\frac{1}{T} - \frac{1}{T_{ref}}\right) \tag{2-16}$$

where ΔH is the activation energy and R is the ideal gas constant which is 8.314 $J/mol \cdot K$. The other one is called Williams–Landel–Ferry or the WLF function and it can be expressed as [61]

$$\log(a_T) = \frac{-C_1\left(T - T_{ref}\right)}{C_2 + \left(T - T_{ref}\right)} \tag{2-17}$$

where C_1 and C_2 are material constants whose values depend on the material and choice of reference temperature T_{ref}. The Arrhenius relationship is more suitable to model the

shift factors of the temperature range below the glass transition temperature whereas the WLF function is generally accepted to model the shift factors of the temperature range above T_g [62-64].

A series of creep or relaxation data taken over a range of temperatures can be converted to a single "*master curve*" via this horizontal shifting. Firstly, a particular curve is chosen as reference. Then the other curves are shifted horizontally to obtain a single curve spanning a wide range of log time as illustrated in Fig. 2.23 [65].
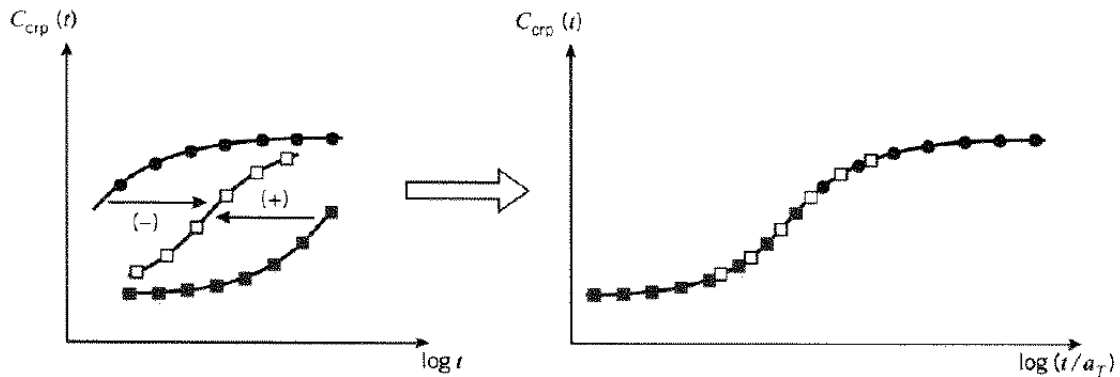
Fig. 2.23 Illustration of master curve formation [65]

Curves obtained at temperature lower than the reference temperature appear at longer times, so they will have to be shifted left; this is a positive shift as we have defined the shift factor in Eqn. (2-15). Each curve produces its own value of a_T, so that a_T becomes a tabulated function of temperature. An example of experimentally measured relaxation modulus master curve is shown in Fig. 2.24. The material is polyisobutylene and the reference temperature is 25 °C. With the concept of master curve, the visco-elastic behavior of polymers at arbitrary time or temperature is uniquely defined. It should be

noted that, although either creep compliance curve or relaxation modulus curve can be used for visco-elastic property description, master curve of relaxation modulus is more widely used in commercial finite element analysis software such as ANSYS.
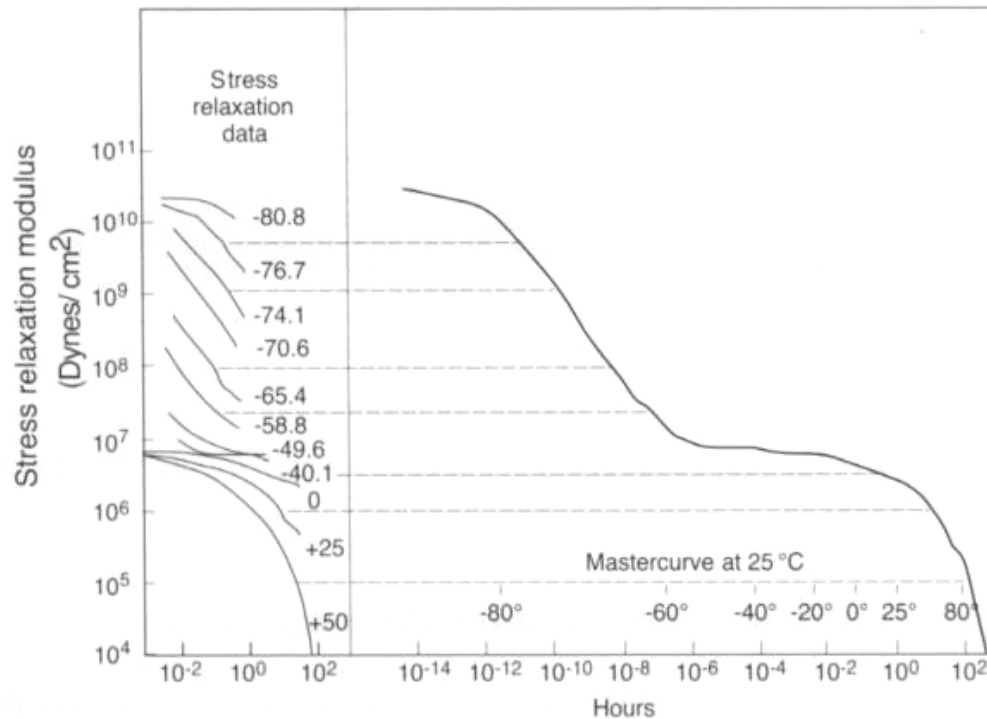
Fig. 2.24 Master curve of relaxation modulus of polyisobutylene with a reference temperature of 25 °C [2]

In practice, a Dynamic Mechanical Analyzer (DMA) is the most commonly used instrument to measure the visco-elastic properties of polymers. The design of a DMA is schematically shown in Fig. 2.25. It can apply several different loadings to the specimen including tension/compression, shear, 3-point bending, clamped bending and torsion. When working in the transient step strain mode and applying a tension loading to the specimen, a DMA is able to measure the time-dependent Young's modulus of a polymeric material.
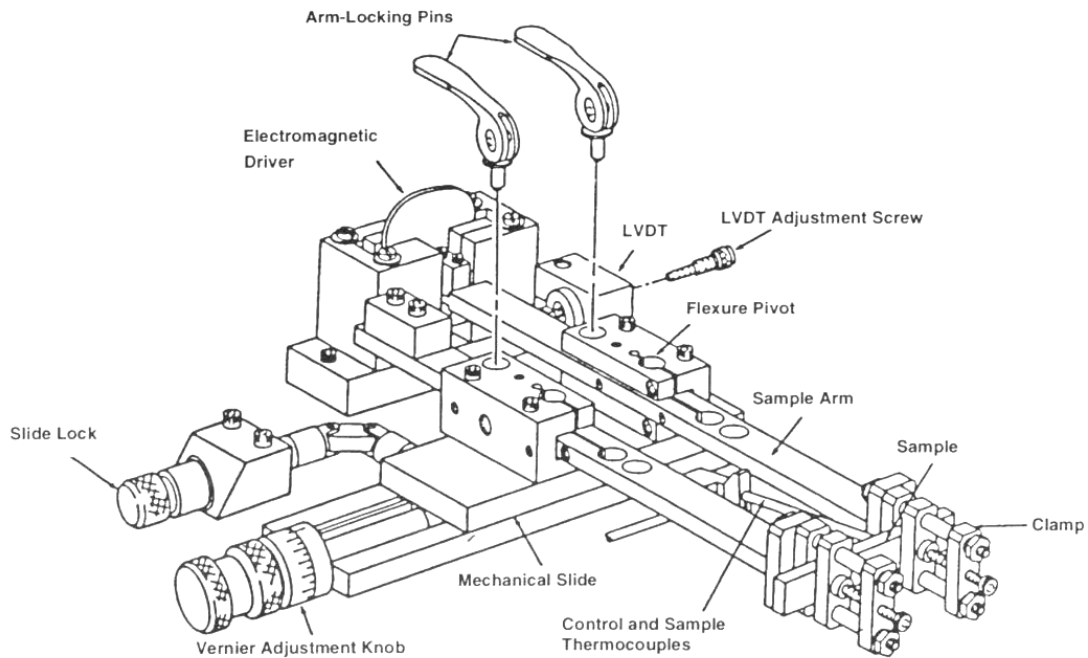
Fig. 2.25 Schematic drawing of a DMA [46]

In the static testing introduced above, special attention should be also paid to the strain measuring system [66]. Compared with metals, polymers have much smaller modulus. The weight of a clip on the extensometer would significantly distort the specimen even before the application of a loading. Thus, non-contacting extensometers such as optical extensometer are widely used. Either visible or infrared light is sent onto the gauge marks on the specimen. Photoelectric sensing devices, using a servo mechanism, follow the gauge marks as the specimen deforms and the resulting movement is monitored by using a displacement transducer, the output from which is sent to the recording device [66]. As it can be seen later, the optical strain sensor is embedded in polymers in our method and thus it has the advantage of no distortion of the specimen.

2.6 Fiber Bragg Gratings as a Sensor

This study will utilize a fiber Bragg grating (FBG) as a strain sensor and the background of FBGs is reviewed in this section. The Bragg grating is named for William Lawrence Bragg who formulated the conditions for X-ray diffraction which relate energy spectra to reflection spacing (Bragg's Law). A fiber Bragg grating is formed by a periodic perturbation of refractive index along the fiber length [67-69]. This periodic perturbation is typically created by exposing the fiber core to an intense interference pattern of UV energy. The formation of permanent grating structures in optical fibers was first demonstrated by Hill and Meltz in 1978 [69]. In their work, they launched high intensity Argon-ion laser radiation into the germanium doped fiber and observed a permanent narrowband Bragg grating filter created in the area of exposure after a period of time.

When a band of the incident light encounters a material of higher index of refraction (one of the periodic gratings), some of the incident light is reflected, some is refracted, and some is transmitted. As illustrated in Fig. 2. 26a, the Bragg grating allows a portion of the incident light to be reflected when the wavelength (known as the Bragg wavelength) satisfies

$$\lambda_B = 2n_{eff}\Lambda \tag{2-18}$$

where λ_B is the Bragg wavelength, n_{eff} is the effective refractive index and Λ is the grating pitch. The amount of the light reflected at the Bragg wavelength is dependent on the perturbation of refractive index, Δn, as well as the total grating length, as each grating serves to reflect a portion of the light signal.
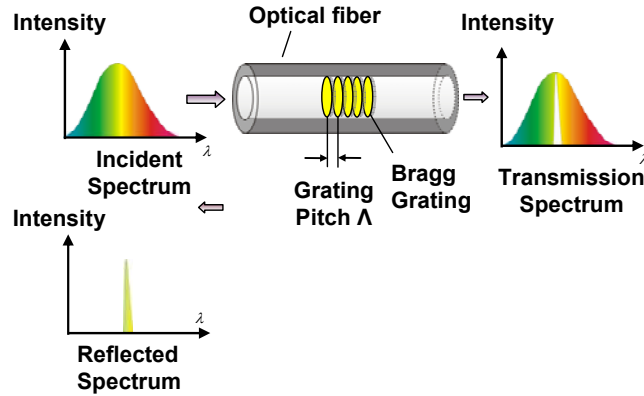
(a)
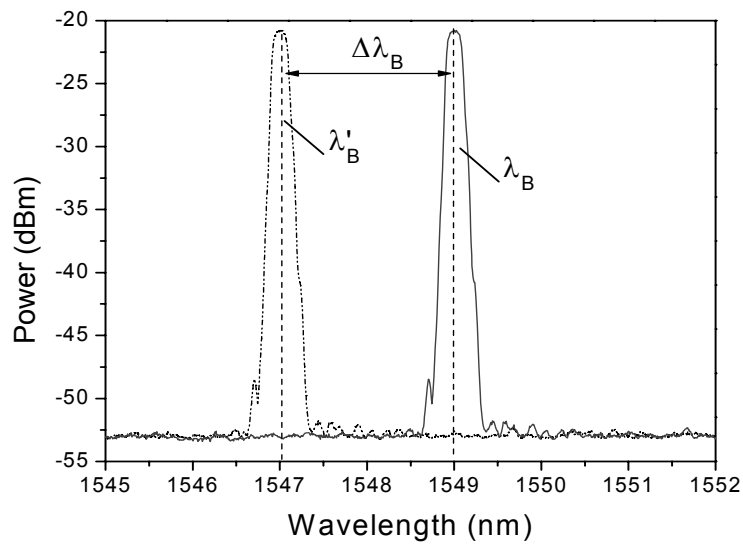
(b)

Fig. 2.26 Illustration of (a) an FBG and corresponding spectrum and (b) BW shift

External disturbances such as changes in strain or temperature will alter the effective refractive index and the grating pitch, which induces a shift in the Bragg wavelength (as illustrated in Fig. 2.26b). This is the basic principle of using FBGs as a sensor.

Differentiating Eqn. (2-18) yields [67-69],

$$\frac{\Delta\lambda_B}{\lambda_B} = \frac{\Delta\Lambda}{\Lambda} + \frac{\Delta n_{eff}}{n_{eff}} = \varepsilon_1 + \frac{\Delta n_{eff}}{n_{eff}} \tag{2-19}$$

where $\Delta\Lambda$ and Δn_{eff} are the changes in the grating pitch and the effective refractive index, respectively, and ε_1 is the axial strain along the fiber. For the case of isotropic and straight Bragg grating, we have [70]

$$\Delta n_{eff} = -\frac{n^3}{2}\left[P_{12}\varepsilon_1 + \left(P_{11} + P_{12}\right)\varepsilon_2 - \left\{\frac{2}{n^3}\frac{dn}{dT} + \left(P_{11} + 2P_{12}\right)\alpha_f\right\}\Delta T\right] \tag{2-20}$$

where ε_2 is the transverse strain, P_{ij} are strain-optic coefficients (Prockel's coefficients), $\frac{dn}{dT}$ is the thermo-optic coefficient, α_f is the CTE of the fiber core material, and ΔT is the temperature change with respect to the initial condition.

If the loading condition is uni-axial where $\varepsilon_2 = -\nu\varepsilon_1$ and assuming no temperature change, Eqns. (2-19) and (2-20) can be simplified to their more common form of

$$\Delta\lambda_B = \lambda_B\left(1 - P_k\right)\varepsilon_1 \tag{2-21}$$

where P_k is called "*effective strain-optic constant*" and it is defined as

$$P_k = -\frac{n^2}{2}\left[P_{12} - \nu\left(P_{11} + P_{12}\right)\right] \tag{2-22}$$

where ν is the Poisson's ratio of the fiber material.

Equation (2-21) clearly shows that the Bragg wavelength shift is linearly proportional to the axial strain. In practice, FBGs are widely used as strain sensors. Kang etc. monitored the strain of a filament wound composite tank during hydrostatic pressurization using 20 FBG sensors [71]. From the experimental results, it was successfully demonstrated that the FBG sensor system is useful for health monitoring of large structures that require a large number of sensor arrays. Chan etc. installed forty

44

FBG sensors on Hong Kong's landmark Tsing Ma Bridge and monitored the strain of different parts of the bridge under both railway and highway loads [72]. They compared the measurement results with those obtained by resistive strain gauges and found them in excellent agreement. Kenel etc. used FBG sensors to measure the local reinforcing strains of steel [73]. They concluded that compared with strain gauge measurements, bond properties are much less affected by FBGs.

In addition to sensing the strain, an FBG can be used as a temperature sensor. Suppose an FBG is subjected to a temperature change of ΔT and no mechanical loading, Eqn. (2-19) can be simplified as

$$\Delta \lambda_B = \lambda_B \left(\alpha_f + \frac{1}{n_{eff}} \frac{dn}{dT} \right) \Delta T \qquad (2\text{-}23)$$

As clearly shown in Eqn. (2-23), the Bragg wavelength shift is linearly proportional to the temperature perturbation and thus an FBG can be used as a temperature sensor. For silica fibers, the wavelength-temperature sensitivities are around 6.4 pm/°C, 10 pm/°C and 13 pm/°C at wavelengths 800nm, 1300nm, and 1550nm, respectively [74].

Sun etc. demonstrated a multipoint temperature warning sensor using an array of multichannel matched FBGs [75]. Multiple uniform FBGs with different nominal wavelengths were attached at different positions. When the temperature exceeded the threshold at a certain position, the pulsed light at the corresponding time slot and wavelength were reflected and detected.

In the general case when there are both mechanical and thermal loadings, two different FBGs are usually superimposed for simultaneous measurement of the strain and temperature. Xu etc. set up an array composed of two FBGs with a wavelength of 1300 and 850nm, respectively [76]. Strain and thermal induced perturbation coefficients of

45

each FBG were calibrated experimentally. Then they demonstrated that the strain and temperature can be determined by solving simultaneous equations. Similar work concerning use of FBGs for simultaneous measurement of strain and temperature can be also found in the literature [77, 78]. Recently, Sivanesan provided a guideline for the wavelength selection of dual-wavelength fiber grating sensors in those set-ups [79].

2.7 Use of Fiber Optic Sensors in Properties Determination

The fiber optic sensor is a powerful tool to perform remote, on-line, in-situ monitoring of a structure. Compared to other types of sensors, the fiber optic senor is free from electromagnetic interference and has high chemical and temperature resistance. Moreover, it can be readily embedded due to its light weight and small size, which makes it minimally intrusive in the structure.

Inspired by FBGs' excellent capability of strain and temperature measurement, researchers recently embedded FBGs in structural composites for cure monitoring and residual strain determination. In 1996, Lawrence etc. embedded Fiber Bragg Grating (FBG) sensors, Extrinsic Fabry-Perot interferometer (EFPI) and thermocouples in the carbon fiber/epoxy composites and measured the internal strain and temperature during the processing [80]. Both sensors exhibited the ability to non-destructively measure the curing strain of the composites. Moreover, they compared the results obtained by the FBG sensor with those by the EFPI, and concluded that the difference was induced by the fact that the FBG is sensitive to transverse strain while the EFPI is not.

O'Dwyery etc. used embedded dielectric micro-sensors and FBGs to monitor continuous changes in the conductivity and strain of a carbon fiber reinforced epoxy

composite [81]. The results showed that it is possible to monitor the strain levels in the optical fiber resulting from the onsets of liquification, gelation and vitrification within the surrounding resin matrix. In addition, the FBGs allowed the direct observation of the development of residual strain as a function of time.

Using FBG sensors, Murukeshan etc. studied the mechanical behavior of a multi-layer CFRP (Carbon Fiber Reinforced Plastics) and FGRP (Glass Fiber Reinforced Plastics) composite [82]. FBG sensors were embedded in different layers and the Bragg wavelength was documented when the composite was subject to 3- and 4-point bending test. It was found that the FBG is effective in identifying the defect sites in the composite and the defects significantly affect the mechanical properties of the composite.

Lin even used FBGs in the curing monitoring of a pre-stressed concrete beam [83]. In his experiment, the temperature profile and plastic shrinkage of concrete during the hardening process were measured by the embedded FBGs. Hydration temperature was determined and they concluded that FBGs showed excellent suitability in understanding the hydration process of concrete during hardening.

In order to obtain real-time information of volumetric change of polymers during the curing, Giordano etc. embedded an optical fiber in the EPON-828 epoxy to form an optical time domain reflectometry [84]. The essential principle of Giordano's technique is monitoring the intensity reflection coefficient R at the epoxy/fiber interface which is related to the refractive index by the equation

$$R = \left(\frac{n_f - n_e}{n_f + n_e} \right)^2$$

(2-24)

where n_f and n_e are the refractive index of the optical fiber and epoxy matrix, respectively. Through the Lorentz-Lorenz law, the refractive index of the epoxy is related to its density ρ as

$$\frac{n_e^2 - 1}{n_e^2 + 2} = \frac{N}{3M\varepsilon}\rho\beta \qquad (2\text{-}25)$$

where N is the Avogadro number, M is the molecular weight, ε is the permittivity and β is the polarizability. Using the measured change of R, volume change can be derived using Eqs. (2-24) and (2-25). However, in their derivation, permittivity ε and polarizability β are assumed to be constant, which is over-simplified and needs validation. In addition, the perfect epoxy/fiber interface is very critical but difficult to achieve.

Later, Giordano etc. used FBG sensors to monitor the curing of an epoxy [85]. They measured Bragg wavelength shift between the start and end of the curing and obtained a compression strain of 0.6%. The result is shown in Fig. 2.27.
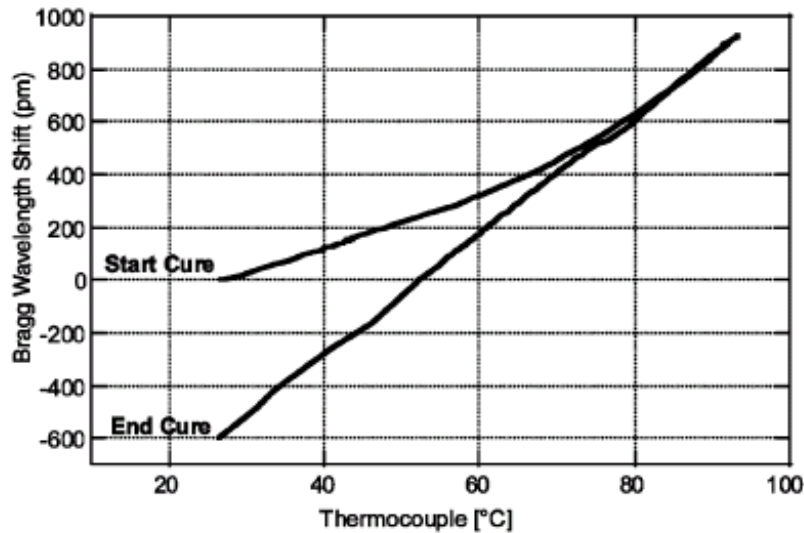
Fig. 2.27 Bragg wavelength shift during the whole curing process [85]

It should be noted that this stain includes the chemical shrinkage as well as the thermal strain, as discussed in chapter 2.2. Besides, further investigation of the dimensions of the epoxy matrix and mold is needed; otherwise, the measured cuing strain will only apply for the bulk material of the same size with the specimen in his experiment.

Using a hybrid FBG/EFPI sensor, Kang etc. simultaneously measured the strain and temperature of a graphite/epoxy composite [71]. A large curing strain in the transverse direction was obtained, whereas the strain in the reinforcing fiber direction was found to be small. The author concluded that this sensor is a suitable choice for efficient monitoring of the curing process of composites. Similar results can be found in Leng's work; the only difference is the material they characterized was Carbon Fiber Reinforced Plastics (CFRP) composites [86]. The results of measured curing strain in two perpendicular directions are shown in Fig. 2. 28.
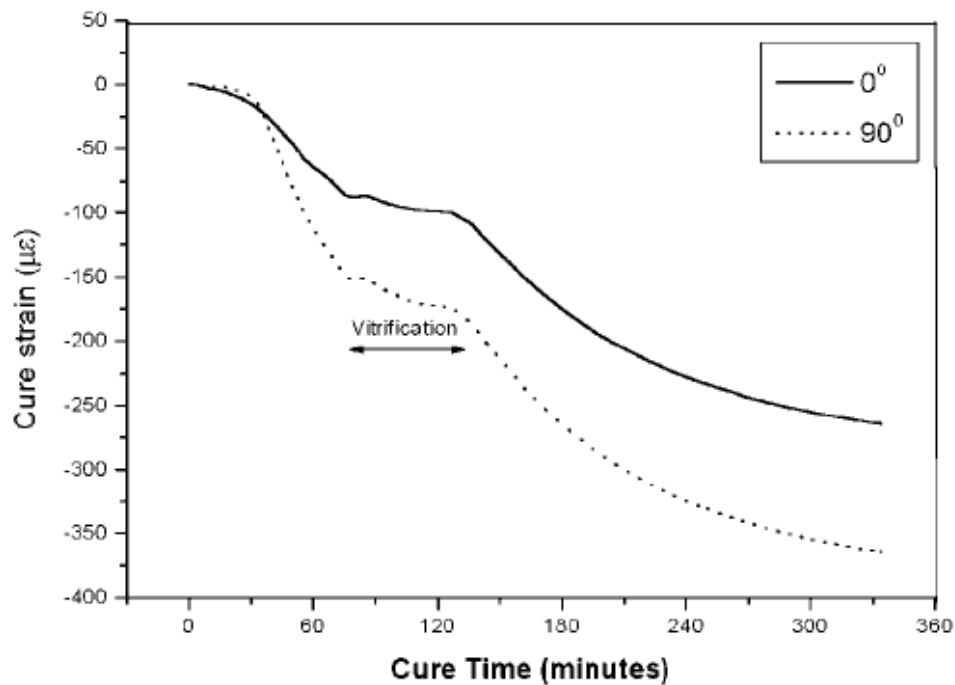
Fig. 2.28 Curing monitoring curve of a CFRP composite using EFPI [86]

All the work reviewed above focuses on the cure strain monitoring not the chemical shrinkage measurement. Bulk materials were used and the measured cure strains included both chemical shrinkage and thermal strain which was induced by the heat generation during the cure/hardening process.

Since the FBG sensor directly detects the stain, it can be used to determine the CTE of a material. To the best of my knowledge, there is only one work where FBG sensors were used to measure the CTE of cementitious composites [87]. The sensors were embedded in cement mortar and ultra-high strength reactive powder concrete prisms. The CTE of the composites was determined by the slope of measured Bragg wavelength shift during a temperature ramp. The accuracy of the measurement was shown to be an order of magnitude higher than that of conventional length measurements.

2.8 Summary

Various existing techniques that measure the chemical shrinkage evolution, modulus evolution, coefficient of thermal expansion, glass transition temperature, visco-elastic properties of polymeric materials are reviewed in this chapter. For chemical shrinkage, most of the methods focus on the measurement of total shrinkage. However, the "effective" chemical shrinkage should be used instead of the total shrinkage in the mechanical modeling simply because the shrinkage that occurs before the gelation point does not contribute to the stress build-up. No efficient method is found to be able to determine the chemical shrinkage evolution as well as the gelation point. For modulus evolution measurement, DMA is the only tool available in the literature. Although the Yong's modulus is desired, however, the shear modulus is measured due to the

50

incapability of the instrument. For CTE measurement, TMA is a standard tool which is based on the displacement measurement. It is expected that higher measurement accuracy can be achieved if a technique can measure the strain directly. DMA proves to be an effective tool in the measurement of visco-elastic properties of polymers. The disadvantage lies in the fact that it can be extremely time-consuming for specimen preparation and it can be difficult for non-experts to practice routinely. With consideration of all the above aspects, an integrated technique which can measure those critical properties is highly desired to cope with the shrinking product development cycle time.

Chapter 3 Proposed Method

3.1 Modeling of FBGs Embedded in Cylindrical Substrate

When modeling the behavior of an FBG embedded in a matrix, Eqn. (2-21) has been widely used for its simplicity [80-82, 85], which is repeated here as

$$\Delta\lambda_B = \lambda_B(1 - P_k)\varepsilon \tag{3-1}$$

where ε is the axial strain. However, when the FBG is embedded, the actual loading applied to the FBG is three dimensional. In this section, an analytical solution is sought for an FBG's response when it is embedded in a cylindrical polymer substrate.

Either mechanical or thermal loading can induce the Bragg wavelength shift of an FBG. By combining Eqns. (2-19) and (2-20), the BW shift can be written as

$$\frac{\Delta\lambda_B}{\lambda_B} = \varepsilon_1 - \frac{n^2}{2}\left[P_{12}\varepsilon_1 + (P_{11} + P_{12})\varepsilon_2 - \left\{\frac{2}{n^3}\frac{dn}{dT} + (P_{11} + 2P_{12})\alpha_f\right\}\Delta T\right] \tag{3-2}$$

where ε_1 and ε_2 are the axial and transverse strains, respectively, P_{ij} are strain-optic coefficients, $\dfrac{dn}{dT}$ is the thermo-optic coefficient, α_f is the CTE of the fiber core material, and ΔT is the temperature change with respect to the initial condition. In the case of coexistence of the thermal loading and mechanical loading, the strain components can be expressed as

$$\varepsilon_1 = \varepsilon_1^\sigma + \alpha_f\Delta T \tag{3-3}$$

and

$$\varepsilon_2 = \varepsilon_2^\sigma + \alpha_f\Delta T \tag{3-4}$$

52

where ε_1^α and ε_2^σ are the stress-induced axial strain and transverse strain of the fiber, respectively. Substituting Eqns. (3-3) and (3-4) back into Eqn. (3-2) results in

$$\Delta\lambda_B = \lambda_B\left(\alpha_f + \frac{1}{n_{eff}}\frac{dn}{dT}\right)\Delta T + \left\{\varepsilon_1^\sigma - \frac{n^2}{2}\left[P_{12}\varepsilon_1^\sigma + \left(P_{11}+P_{12}\right)\varepsilon_2^\sigma\right]\right\}\lambda_B = \Delta\lambda_B^i + \Delta\lambda_B^d$$

(3-5)

where $\Delta\lambda_B^i$ is called "*intrinsic*" BW shift which is defined as

$$\Delta\lambda_B^i = \lambda_B\left(\alpha_f + \frac{1}{n_{eff}}\frac{dn}{dT}\right)\Delta T$$

(3-6)

and $\Delta\lambda_B^d$ is called "*deformation*" induced BW shift which is defined as

$$\Delta\lambda_B^d = \left\{\varepsilon_1^\sigma - \frac{n^2}{2}\left[P_{12}\varepsilon_1^\sigma + \left(P_{11}+P_{12}\right)\varepsilon_2^\sigma\right]\right\}\lambda_B$$

(3-7)

The name "*intrinsic*" is given to $\Delta\lambda_B^i$ as this BW shift is not associated with any stress-induced deformation.

In Eqn. (3-7), ε_1^σ and ε_2^σ are mechanical strains and they can be derived using the theory of elasticity for a given mechanical load. Assume the FBG is a solid cylinder with an outer radius of a; the cylindrical polymer matrix has an inner radius of a and an outer radius of b. A schematic drawing of the FBG and matrix is shown in Fig. 3.1.
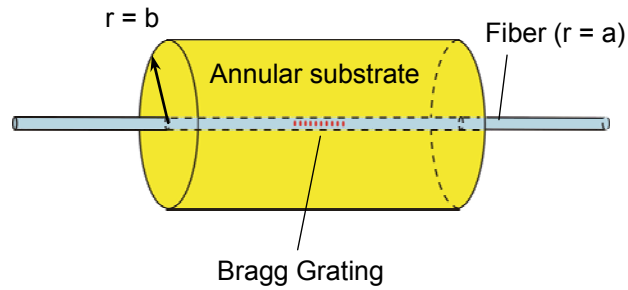
Fig. 3.1 Schematic diagram of an FBG sensor embedded in a cylindrical substrate

A loading condition of a piecewise constant temperature distribution is defined as

$$T(r) = \begin{cases} T_f \, , 0 \le r < a \\ T_s \, , a < r \le b \end{cases} \quad (3\text{-}8)$$

where T_f and T_s are the *pseudo temperature change* of the fiber and the substrate from the reference temperature, respectively. The piecewise constant temperature condition is introduced for evaluation of chemical shrinkage, which by analogy, can be simulated as thermal contraction.

In this analogy, the tendency to shrink is proportional to the temperature change. Since the strain due to chemical shrinkage is different in each material, it is necessary to allow for different "pseudo-temperature" changes in each material. With the assumption of the generalized plane strain condition where the strain in the axial direction is set to be an unknown constant, the analytical solution of the stress components can be derived. The formulations are shown in the Appendix - A, where the subscripts, *f* and *s*, are used to identify the fiber and substrate parameters, respectively.

The derived analytical solution was verified by a 2-D axi-symmetric finite element model. The radius of the fiber, *a*, was 62.5 μm and two different configurations of substrate (*b* = 1.25 mm and 12.5 mm) were used in the verification. The fiber had a CTE of 0.55 ppm/ºC, a modulus of 73 GPa and a Poisson's ratio of 0.17. The CTE, modulus and Poisson's ratio of the polymer matrix were 60 ppm/ºC, 2 GPa and 0.3, respectively. The assembly was subjected to a thermal loading of $T_f = 0$ and $T_s = -20°C$. The results obtained from the analytical model and the FEM are shown in Fig. 3.2. They agree with each other very well, which confirms the validity of the analytical solution.
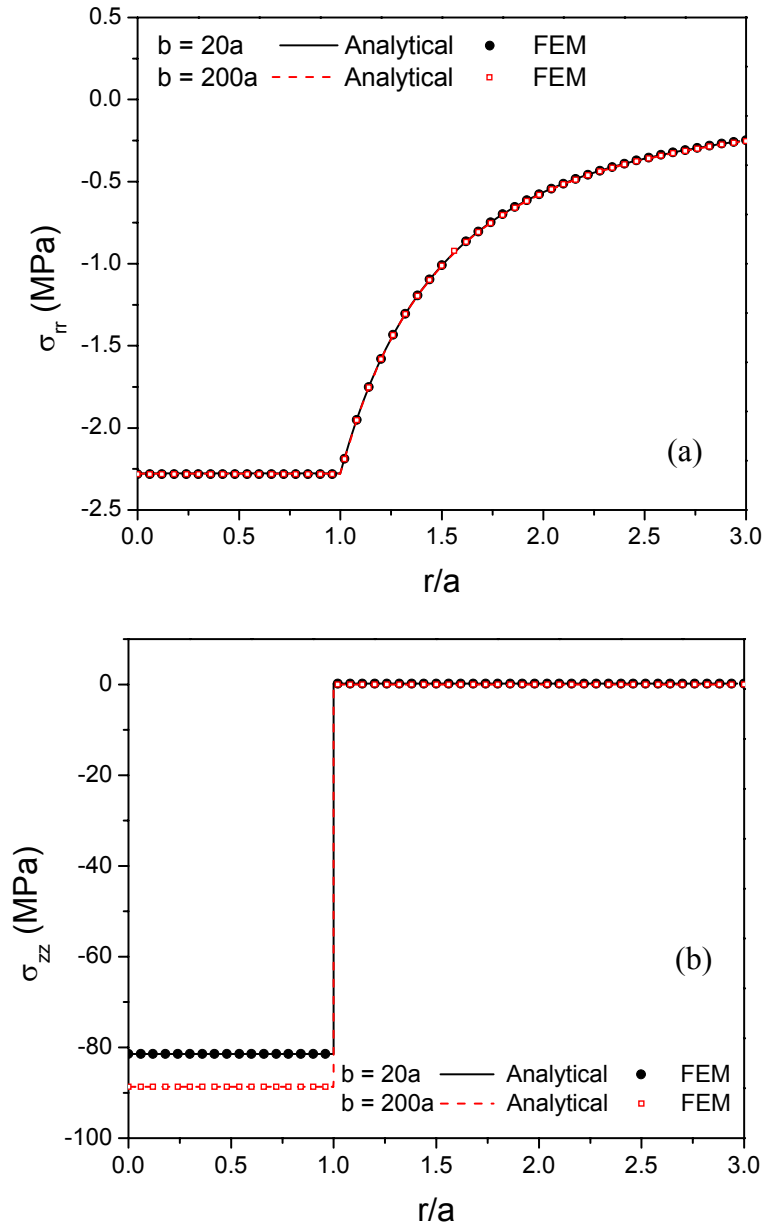
Fig. 3.2 Comparison of generalized plane strain solution with the axi-symmetric FEM model: (a) radial stress, σ_{rr} (b) axial stress, σ_{zz}

The analytical solution is formulated in terms of stress components. Considering $\sigma_{rr}^{f} = \sigma_{\theta\theta}^{f}$ (see A-1' and A-2' in the appendix), the stress-strain relationship yields

$$\varepsilon_1^{\sigma} = \frac{1}{E_f}(\sigma_{zz}^f - \upsilon_f \sigma_{rr}^f - \upsilon_f \sigma_{\theta\theta}^f) = \frac{1}{E_f}(\sigma_{zz}^f - 2\upsilon_f \sigma_{rr}^f) \qquad (3\text{-}9)$$

$$\varepsilon_2^{\sigma} = \frac{1}{E_f}(\sigma_{rr}^f - \upsilon_f \sigma_{\theta\theta}^f - \upsilon_f \sigma_{zz}^f) = \frac{1}{E_f}\left((1-\upsilon_f)\sigma_{rr}^f - \upsilon_f \sigma_{zz}^f\right) \qquad (3\text{-}10)$$

Substituting Eqns. (3-9) and (3-10) into Eqn. (3-7), the relationship between the stress components and the "*deformation*" induced BW shift can be expressed as

$$\Delta\lambda_B^d = \frac{1}{E_f}\left\{\left[1 - \frac{n^2}{2}\left(P_{12} - (P_{12} + P_{11})\upsilon_f\right)\right]\sigma_{zz}^f - \left[2\upsilon_f + \frac{n^2}{2}\left((1-\upsilon_f)P_{11} + (1-3\upsilon_f)P_{12}\right)\right]\sigma_{rr}^f\right\}\lambda_B$$

$$(3\text{-}11)$$

Through Eqn. (3-11), an analytical relationship between the "deformation induced" BW shift and the material properties of the polymer substrate under the loading condition of Eqn. (3-8) has been established.

3.2 Basic Concept of the Proposed Method

The proposed method employs the basic characteristic of the FBG. As illustrated in Fig. 3.1, a polymer of interest is cured around the FBG and the BW shift is measured and documented while (1) polymerization progresses at the curing temperature, (2) the temperature of the cured polymer changes and (3) a uni-axial tension is applied to the cured polymer. The critical material properties of the polymer are determined from the analytical relationship among the BW shift, the deformation of the FBG and the impact of the polymer properties on this deformation. Specifically, the chemical shrinkage and curing kinetics are determined from the measured $\Delta\lambda_B^d$ during the curing; CTE and T_g are calculated from the measured $\Delta\lambda_B^d$ when the cured specimen is subjected to temperature

excursions; visco-elastic properties are determined from the measured $\Delta\lambda_B^d$ when the cured specimen is subjected to an axial tension at various temperatures.

The Bragg wavelength can be measured accurately by a spectrum analyzer. Within the relatively small temperature range considered for polymers, the thermo-optic constant, $\dfrac{dn}{dT}$, and the CTE, α_f, of the fiber can be assumed to remain constant. Then the "*intrinsic*" BW shift $\Delta\lambda_B^i$, which is defined in Eqn. (3-6), is a linear function of ΔT and can be readily measured from a simple calibration experiment with a bare FBG. In an actual experiment, the BW is monitored continuously to produce $\Delta\lambda_B$ and $\Delta\lambda_B^d$ is obtained by subtracting $\Delta\lambda_B^i$ from $\Delta\lambda_B$.

3.3 Property Evolution During Curing

3.3.1 Specimen configurations

A careful investigation of the analytical solution reveals that successful implementation of the proposed method, i.e., obtaining maximum sensitivity and accuracy in the determination of the polymer substrate properties, requires a detailed understanding of the sensitivity of the "deformation" induced BW shift, $\Delta\lambda_B^d$, to (1) the outer radius of the polymer, b, and (2) Poisson's ratio of the polymer, υ_s.

The stress-induced axial strain of the fiber ε_1^σ and the corresponding $\Delta\lambda_B^d$ are shown in Fig. 3.3 for three different moduli of the polymer substrate. The radius of fiber, a, is 62.5 μm and the CTE of the polymer, α_s, is 60 ppm/ºC. In the analysis, a piece-

wise temperature change of $T_s = -10°C$ and $T_f = 0$ is used to simulate a uniform contraction of the substrate.
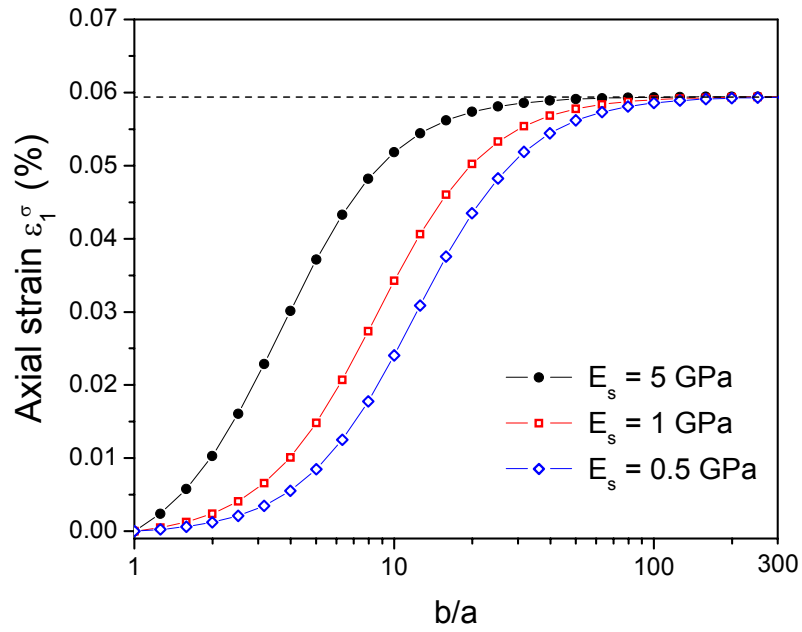
(a)
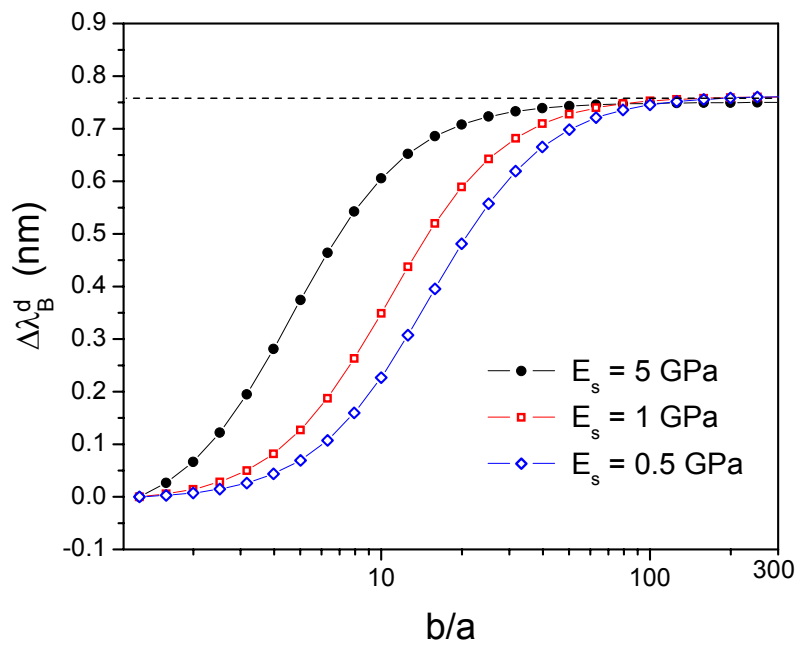
(b)

Fig. 3.3 Effect of polymer radius: (a) axial strain and (b) the corresponding BW shift

It can be seen from Fig. 3.3 that ε_1^σ converges to a limit as the ratio of b to a increases to above 200 virtually regardless of the modulus of the polymer. Physically, the results can be explained by the fact that as "b" increases, the volume stiffness, defined as the volume multiplied by the modulus, of the polymer increases while the volume stiffness of the fiber remains constant; the effective behavior of the polymer/fiber assembly will be essentially governed by the polymer as the effect of the fiber gradually decreases.

The effect of Poisson's ratio is plotted in Fig. 3.4, which clearly indicates that Poisson's ratio has virtually no impact on $\Delta\lambda_B^d$. In the analysis, the CTE and modulus of the polymer is 60 ppm/°C and 2.5 GPa, respectively. This ignorable effect of Poisson's ratio can be also understood from the fact that the deformation is produced primarily by a uni-axial loading.
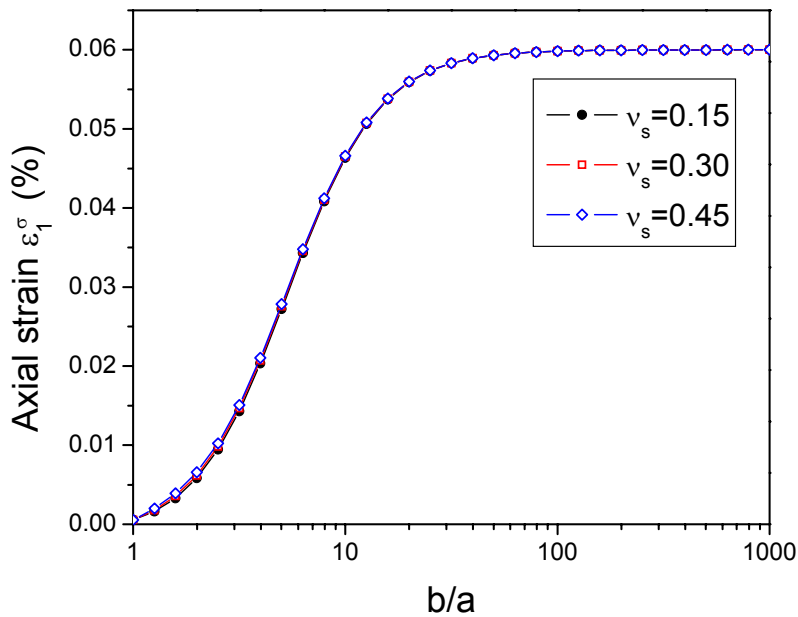
(a)
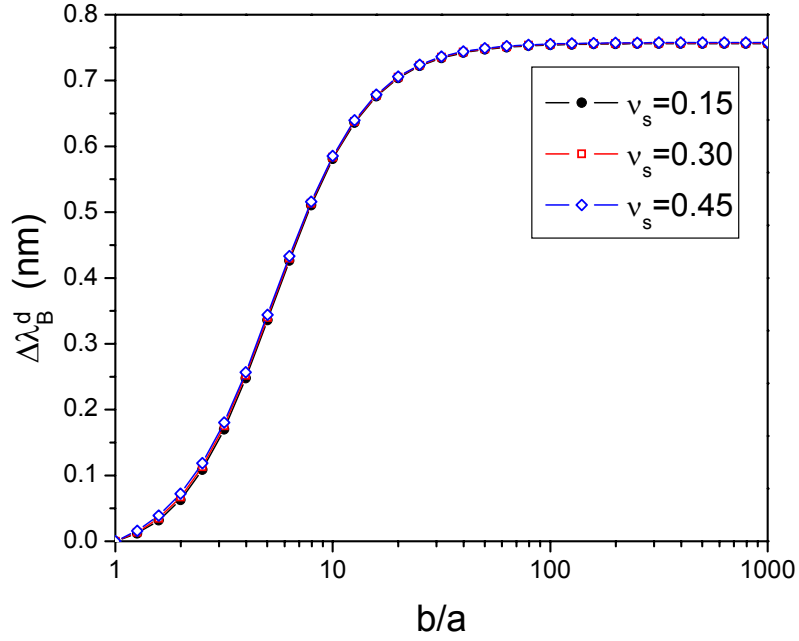
(b)

Fig. 3.4 Effect of Poisson's ratio: (a) axial strain and (b) the corresponding BW shift

The above analysis reveals several important facts. The BW shift is dependent on the polymer substrate's shrinkage strain and modulus, not on the Poisson's ratio. As a result, the total number of unknown material properties is reduced from 3 to 2. In addition, $\Delta\lambda_B^d$ is highly dependent on the polymer radius, b, with material properties fixed. In the extreme case of a large specimen configuration ($b/a > 200$), $\Delta\lambda_B^d$ is independent of the modulus and Poisson's ratio and only a function of chemical shrinkage occurred in the polymer. The curing shrinkage can be simply determined as

$$\varepsilon_{cure} = \varepsilon_f^\sigma = \frac{\Delta\lambda_B^d}{\lambda_B(1-P_k)} \quad for \ b/a > 200 \qquad (3\text{-}12)$$

Eqn. (3-12) is also the rationale used in previous studies when FBGs were embedded in a polymer matrix to measure the curing shrinkage [71, 80-82, 85].

The strain measured in Eqn. (3-12) is said to be curing shrinkage not chemical shrinkage, because a thermal strain is incorporated due to the heat generation during the curing process. Polymerization is an exothermic process and the temperature can rise considerably, especially in bulk materials. For a specimen with a cylindrical shape as illustrated in Fig. 3.5, the Fourier's heat conduction equation has the form

$$k\left(\frac{\partial^2 T}{\partial r^2} + \frac{1}{r}\frac{\partial T}{\partial r}\right) + \dot{q} = \rho c_p \frac{\partial T}{\partial t} \qquad (3\text{-}13)$$

where k is the thermal conductivity, T is the temperature, t is the time, ρ is the density, c_p is the specific heat and $\dot{q}$ is the heat generation rate.
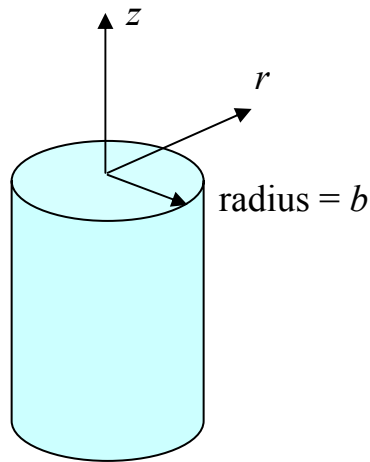
Fig. 3.5 Illustration of a cylindrical specimen subjected to convection heat transfer

The heat generation rate is directly related to the reaction speed through the equation

$$\dot{q} = \rho \Delta H \frac{dp}{dt} \qquad (3\text{-}14)$$

where p is the curing extent and ΔH is the total exotherm of the reaction. For simplicity, the polymerization can be modeled by an nth order model [52, 88-93]

$$\frac{dp}{dt} = k_c(1-p)^n \qquad (3\text{-}15)$$

where k_c is a temperature-dependent rate coefficient and it is related to the temperature through Arrhenius's equation

$$k_c = Ae^{-\frac{E_a}{RT}} \qquad (3\text{-}16)$$

where A is a material constant, E_a is the activation energy and R is the ideal gas constant, which is 8.314 $J/mol \cdot K$. Substituting Eqns. (3-14), (3-15) and (3-16) back into Eqn. (3-13) will yield the governing equation for thermal modeling of polymerization process

$$\begin{cases} \dfrac{k}{\rho}\left(\dfrac{\partial^2 T}{\partial r^2} + \dfrac{1}{r}\dfrac{\partial T}{\partial r}\right) + Ae^{-\frac{E_a}{RT}}(1-p)^n \Delta H = c_p \dfrac{\partial T}{\partial t} \\ \dfrac{dp}{dt} = Ae^{-\frac{E_a}{RT}}(1-p)^n \end{cases} \qquad (3\text{-}17)$$

The boundary conditions are

$$\begin{cases} T|_{t=0} = T_0 \\ -k\dfrac{\partial T}{\partial r}\bigg|_{r=b} = h(T - T_a) \\ p|_{t=0} = 0 \end{cases} \qquad (3\text{-}18)$$

where h is the convective heat transfer coefficient and T_a is the ambient temperature and T_0 is the initial temperature. Equation (3-17) is highly nonlinear and can be solved using a finite element method.

The temporal and spatial distribution of the temperature of a cylindrical bulk polymer during the polymerization process was solved using ANSYS. An axis-symmetric plane element 55 was used. A convection boundary condition was applied to the outer surface of the cylinder, with a convective heat transfer coefficient of $60\,W/m^2 \cdot K$. Suppose that the total number of nodes is m and the whole polymerization

process is divided into n steps with a time interval of Δt. In the ith (from 2 to n) time step, the curing extent at node j (from 1 to m) can be approximated by

$$p_{i,j} = Ae^{-\frac{E_a}{RT_{i-1,j}}}(1-p_{i-1,j})^n \Delta t + p_{i-1,j} \qquad (3\text{-}19)$$

where $T_{i-1,j}$ is the temperature at node j in the $i\text{-}1^{th}$ (from 1 to $n-1$) time step. Then the heat generation rate was updated according to Eqn. (3-14) and the corresponding temperature distribution was calculated. The newly obtained temperature and curing extent at each node were saved as an initial condition for the next time step.

The radius of the polymer was 12.5mm which corresponds to the case of $b/a = 200$. Representative polymer properties of thermal conductivity and specific heat were used; $0.25\ W/m \cdot K$ and $1500\ J/kg \cdot K$, respectively [94]. Curing kinetics parameters were $A = 29.1/s$, $E_a = 35.8\ kJ/mol$ and the curing temperature was 165 °C [52]. They are representative of various polymers and they yield a typical polymerization rate of $k_c \approx 0.002\ /s$ at the curing temperature [52, 88-93]. The total exotherm was 300 J/g which is typical for pure polymers and composites [4, 91, 92, 95-103].

The temperature profile of the case of $b/a = 200$ is shown in Fig. 3.6. The curing temperature 165 °C is chosen as the reference (T_c) and the temperature overshooting is normalized by it.
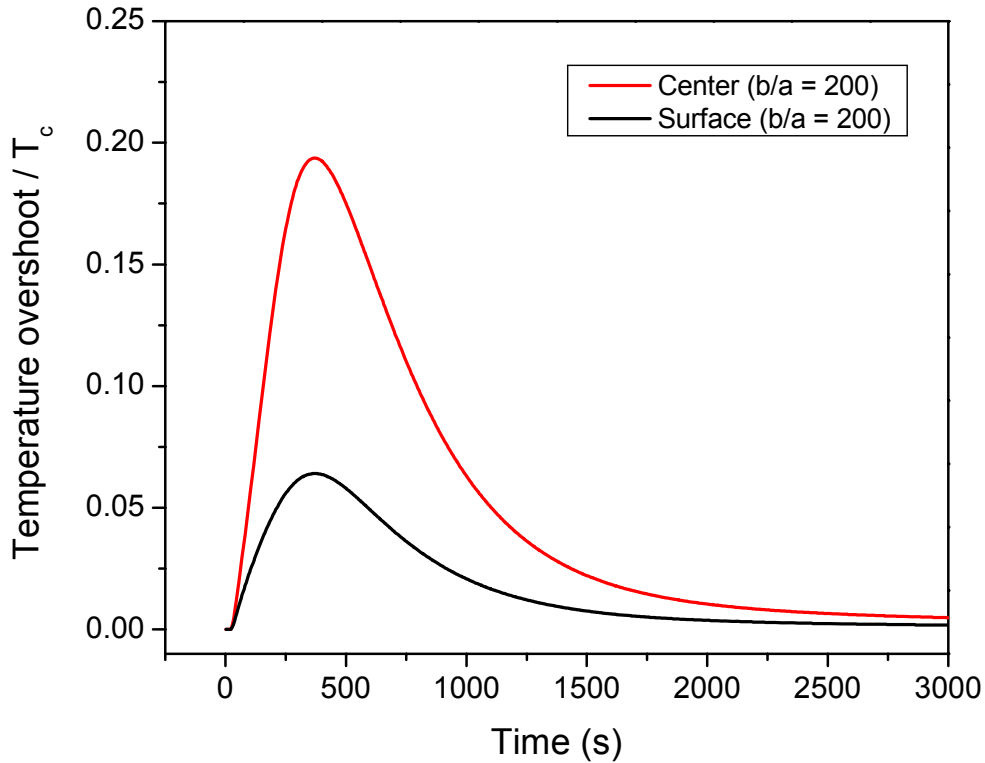
Fig. 3.6 Temperature profile of a cylindrical polymer during the curing

As seen from the figure, the center temperature overshoots by $0.2T_c$ at the maximum, which is significant. When the material is partially cured, the embedded FBG will be subjected to a large thermal strain while the temperature is dropping back to T_c. The deformation will be incorporated together with the chemical shrinkage and measured from Eqn. (3-12). Moreover, it is important to note a large temperature gradient exists in the material. This can be seen more clearly from Fig. 3.7, which shows the temperature spatial distribution at the time of $t = 370s$.
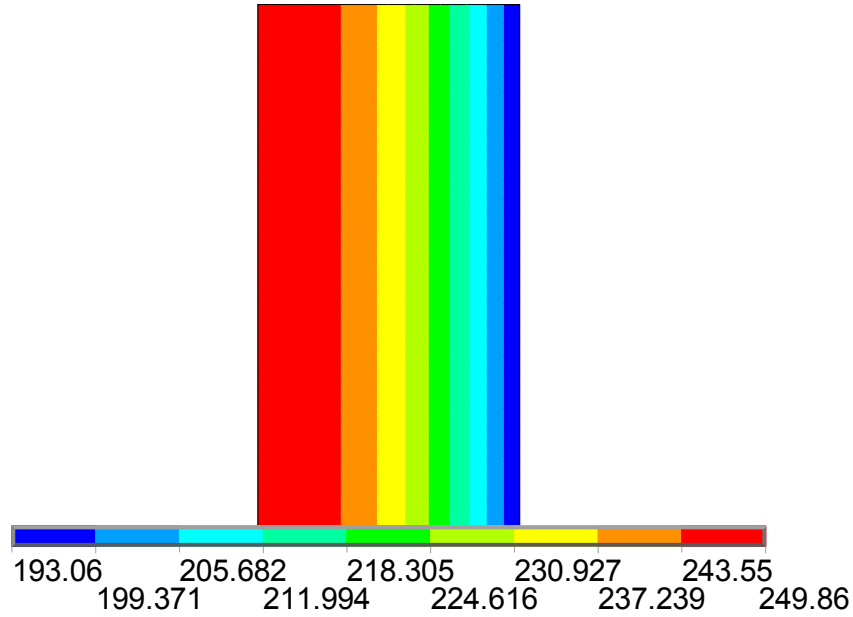
Fig. 3.7 Temperature spatial distribution at time t = 370s (Unit: °C)

This uneven temperature distribution will result in the non-uniform curing of the material. Specifically, the curing extent evolution of center material and surface material is plotted in Fig. 3.8. From the figure, it can be seen that the center material cures much faster than the surface material because the polymerization is greatly accelerated by the high temperature. As a result, the merit of sensing the center strain is seriously undermined. Since (1) the thermal strain and chemical shrinkage become non-separable and (2) non-uniform curing occurs in the material, the traditional method [71, 80-82, 85] of using bulk material is not suitable for the measurement of the chemical shrinkage.
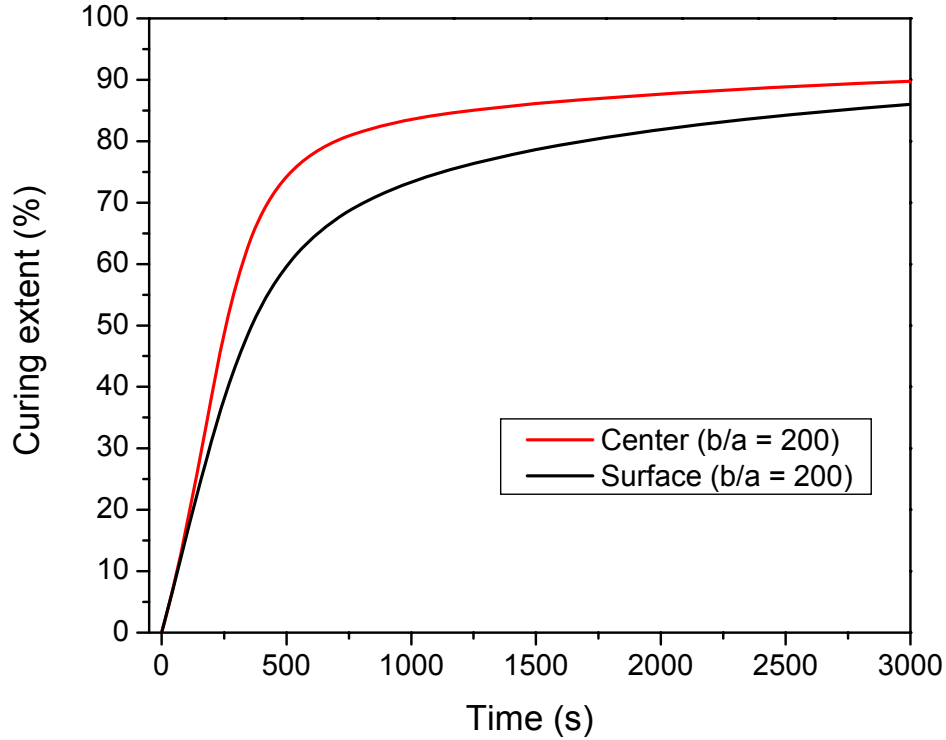
Fig. 3.8 Curing extent evolution of a cylindrical polymer during the curing

The above analysis shows the fact that FBG sensors should be embedded in polymers of small size to avoid the problems associated with the polymerization heat. In this case, the two unknowns – effective chemical shrinkage and modulus will be coupled and both of them will affect the BW shift. This can be clearly seen from Fig. 3.3(a). Through the numerical procedure described in the following section, the effective chemical shrinkage and modulus evolutions can be determined from the measured BW shift of two different specimen configurations.

3.3.2 Procedure to determine property evolutions

Assume that a shrinkage strain of $\Delta\varepsilon^{ch}$ occurs in the polymer substrate which has an instant modulus of E_s. The loading condition can be written mathematically as

$$\varepsilon(z) = \begin{cases} 0 & \text{for } 0 \leq r < a \\ \Delta\varepsilon^{ch} & \text{for } a < r \leq b \end{cases} \tag{3-20}$$

where a is the radius of the FBG and b is the radius of the polymer substrate. The thermal analogy [Eqn. (3-8)] can be written as

$$T(r) = \begin{cases} 0, 0 \leq r < a \\ \dfrac{\Delta\varepsilon^{ch}}{\alpha_s}, a < r \leq b \end{cases} \tag{3-21}$$

where α_s is the CTE of the polymer and it can be set to be an arbitrary number. After substituting (A-1') and (A-2') into Eqn. (3-11), the BW shift of the embedded FBG produced by the chemical shrinkage of $\Delta\varepsilon^{ch}$ is can be formulated. The governing equation will take a form of

$$\Delta\lambda_B^d = F\left(E_s, \beta\right) \cdot \Delta\varepsilon^{ch} \tag{3-22}$$

where $\beta = \dfrac{b}{a}$ and F is a nonlinear function of E_s and β. The specific form of the formulation is not shown here to avoid associated mathematical redundancy.

Since there are only two unknown constants (effective chemical shrinkage and modulus) in the governing equation (3-22), the BW shifts are measured for two different specimen configurations to determine the constants. The two configurations are referred to as C-1 and C-2 with $\beta = \beta_1$ and β_2, respectively. Typical results of the measured BW shifts in the two configurations are illustrated schematically in Fig. 3.9. The effective chemical shrinkage and modulus evolve with time during the curing history. They are determined incrementally by dividing the entire curing history into numerous small time segments.
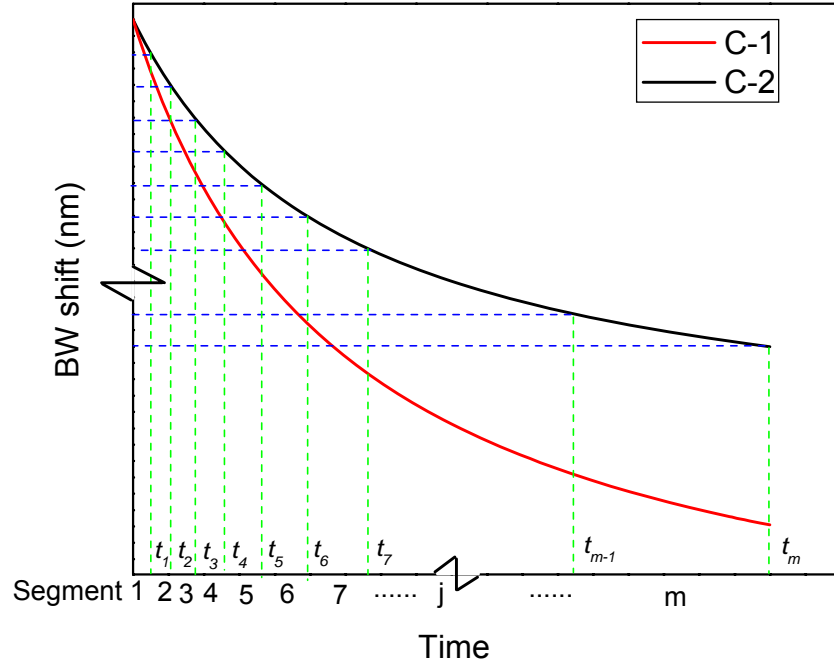
Fig. 3.9 Illustration of BW shifts and the segment division of two configurations

In the procedure, the measured BW shifts are first divided into m small constant segments as shown in Fig. 3.9. The division is made so that the BW shift of C-2 (assume $\beta_2 < \beta_1$) in each segment is even. Let the BW shift increments of C-1 and C-2 in the jth ($j = 1$ to m) segment be $\Delta\lambda_{B1,j}$ and $\Delta\lambda_{B2,j}$. The corresponding time segment begins at time t_{j-1} and ends at time t_j. From the governing equation (3-22), the following simultaneous equations can be developed

$$\begin{cases} \Delta\lambda_{B1,j} = F\left(E_{s,j},\beta_1\right)\cdot\Delta\varepsilon_j^{ch} \\ \Delta\lambda_{B2,j} = F\left(E_{s,j},\beta_2\right)\cdot\Delta\varepsilon_j^{ch} \end{cases} \tag{3-23}$$

The shrinkage increments $\Delta\varepsilon_j^{ch}$ and the instant equilibrium modulus $E_{s,j}$ in the jth time segment can be determined one after the other. Dividing the first equation by the second one in Eqn. (3-23) will eliminate $\Delta\varepsilon_j^{ch}$, and thus $E_{s,j}$ can be determined first by

68

solving the nonlinear equitation. Then by substituting $E_{s,j}$ back into either one of the equations, $\Delta\varepsilon_j^{ch}$ can be calculated. By repeating the above calculations for j iterating from 1 to m, the shrinkage increment and instant modulus in every segment can be determined. The property evolutions can then be expressed as

$$\varepsilon^{ch}(t_j) = \sum_{i=1}^{j} \Delta\varepsilon_i^{ch} \text{ and } E_s(t_j) = E_{s,j} \ (j = 1 \text{ to } m). \tag{3-24}$$

The above procedure is repeated when m increases until the convergence is achieved. It is important to note that the result of effective chemical shrinkage is in an accumulated manner while the result of the modulus is instantaneous.

3.4 Procedure to Determine CTE and T_g

When the polymer/FBG assembly is subjected to a uniform temperature change, the loading condition expressed in Eqn. (3-8) can be rewritten as

$$T(r) = \begin{cases} \Delta T, 0 \leq r < a \\ \Delta T, a < r \leq b \end{cases} \tag{3-25}$$

where ΔT is the temperature change of the fiber and polymer from the reference point. As mentioned earlier, if the polymer substrate has infinite dimension, the effective behavior of the polymer/fiber assembly will be entirely governed by the polymer. The axial strain in the limit of $b = \infty$ is proportional to the CTE mismatch between the fiber and the polymer and it can be expressed as

$$\varepsilon_1^{\sigma}\big|_{\infty} = \left(\alpha_s - \alpha_f\right) \cdot \Delta T \tag{3-26}$$

It is worth noting that the axial stress is two orders of magnitude larger than the radial stress when b is much larger than a (Fig. 3.2), which indicates that the FBG is

subjected to a nearly uni-axial loading condition. Consequently, the governing equation (3-7) can be reduced to

$$\Delta\lambda_B^d\Big|_\infty = \lambda_B(1-P_k)(\alpha_s-\alpha_f)\Delta T \qquad (3\text{-}27)$$

where P_k is the effective strain-optic constant. Then, the CTE of polymer, α_s, can be evaluated as

$$\alpha_s(T) = \frac{\Delta\lambda_B^d\Big|_\infty(T)}{\lambda_B(1-P_k)\Delta T} + \alpha_f \qquad (3\text{-}28)$$

where α_f is the CTE of the fiber. High accuracy in the CTE measurement is expected since the proposed technique obtains a CTE value directly from the measured strains. This is to be contrasted with use of the TMA method, in which the CTE is determined from measured displacements.

The advantage of using an infinite specimen lies in that the numerical calculation is fairly simple and the determination of CTE is very straightforward. In practice, however, it is impossible to fabricate a specimen with an infinite radius. In addition, as explained in the section 3.3.1, the polymer will be cured non-uniformly when b is too large, and the material property would be different at different locations. The behavior of an infinite polymer/FBG assembly can be numerically reconstructed from the behavior of the specimen with the proposed two configurations, and thus the concept of using an infinite specimen can be still employed. The numerical procedure is elaborated below.

When the polymer/FBG assembly is subjected to the loading condition which is defined in Eqn. (3-25), the governing equation will take the form of

$$\Delta\lambda_B^d = H\big(E_s,\beta\big)\cdot(\alpha_s-\alpha_f)\cdot\Delta T \qquad (3\text{-}29)$$

where $\beta = \dfrac{b}{a}$, H is a nonlinear function and E_s is an instantaneous relaxed modulus.

From Eqn. (3-29), it can be seen that the ratio of the BW shift between different specimen configurations is independent of the polymer CTE. In particular, we define the ratio between the infinite specimen and the specimen of $\beta = \beta_1$ to be κ, and the ratio between the specimen of $\beta = \beta_1$ and the specimen of $\beta = \beta_2$ to be η. Mathematically, they have the form of

$$\kappa = \frac{\Delta\lambda_B^d\big|_{\beta=\infty}}{\Delta\lambda_B^d\big|_{\beta=\beta_1}}, \qquad \eta = \frac{\Delta\lambda_B^d\big|_{\beta=\beta_1}}{\Delta\lambda_B^d\big|_{\beta=\beta_2}} \tag{3-30}$$

A nonlinear function can be defined to correlate κ and η, which is called the compensation ratio master curve $\kappa = g(\eta)$. To calculate the compensation ratio master curve, BW shifts at the three configurations ($\beta = \infty$, $\beta = \beta_1$ and $\beta = \beta_2$) are determined first from Eqn. (3-11) with a pre-set polymer CTE. Then the ratio among them is calculated for a wide range of moduli. As an example, the compensation ratio master curve for the case of $\beta_1 = 40$ and $\beta_2 = 20$ is show in Fig. 3.10.

Typical BW shifts is illustrated in Fig. 3.11, where the cured specimens of configuration C-1 and C-2 are subjected simultaneously to a temperature ramping. It should be noted that the illustrated BW shift is the deformation induced part and it can be obtained from subtracting the intrinsic part from the experimentally measured total BW shift. Then the obtained BW shifts of configuration C-1 and C-2 are divided into m small constant segments as shown in Fig. 3.11. The division is made so that the temperature increment in each segment is even. The BW shift increment is calculated and η is determined thereafter. From the compensation ratio master curve, the corresponding

value of κ is identified and the BW shift increment of the infinite configuration (C-inf) can be calculated using

$$\Delta \lambda_B^d \Big|_{\beta=\infty} = \kappa \cdot \Delta \lambda_B^d \Big|_{\beta=\beta_1} \tag{3-31}$$

By summing the BW shift increment, the BW shift versus temperature curve at configuration C-inf is obtained. The result is illustrated in Fig. 3.11. The above procedure is repeated when m increases until the convergence is achieved. Finally, through Eqn. (3-28), the temperature-dependent CTE of the polymer substrate can be determined. The glass transition temperature then is located at the inflection point of the CTE-temperature curve.
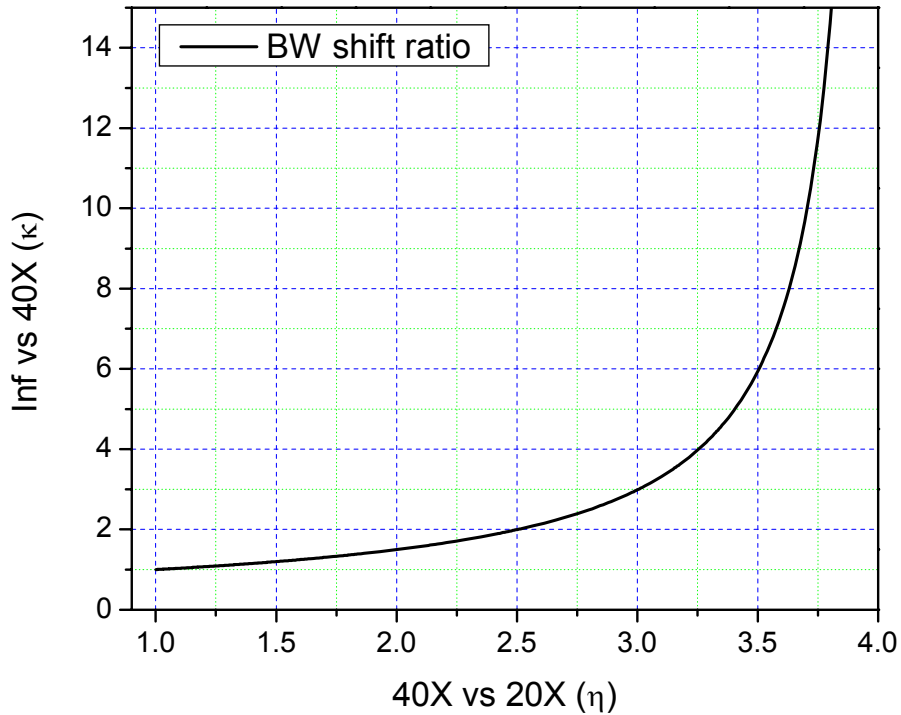
Fig. 3.10 Compensation ratio master curve for the case of $\beta_1 = 40$ and $\beta_2 = 20$
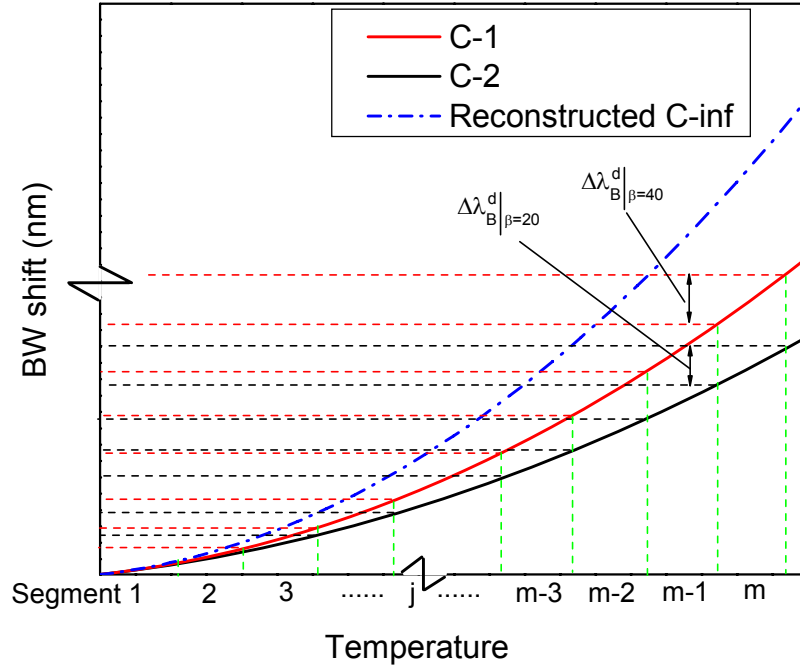
Fig. 3.11 Illustration of BW shift segment division and reconstruction of C-inf

3.5 Procedure to Determine Visco-elastic Properties

After the cured polymer/FBG specimen is subjected to a temperature ramping and the CTE and T_g are determined from the measured BW shift, an instantaneous uni-axial mechanical load is applied to the specimen and the corresponding BW shift is measured at different temperatures. The polymer/FBG specimen is illustrated in Fig. 3.12. Assume the radius of the polymer, b, is β times of the radius of the FBG, a, and the total applied force is F. The equilibrium equation has the form

$$E_f \cdot \varepsilon(t) \cdot \pi \cdot a^2 + 1/C(t) \cdot \varepsilon(t) \cdot \pi \cdot \left(\beta^2 a^2 - a^2 \right) = F \tag{3-32}$$

where $\varepsilon(t)$ is the time-dependent axial strain, E_f is the modulus of the FBG and $C(t)$ is the time-dependent compliance of the polymer.
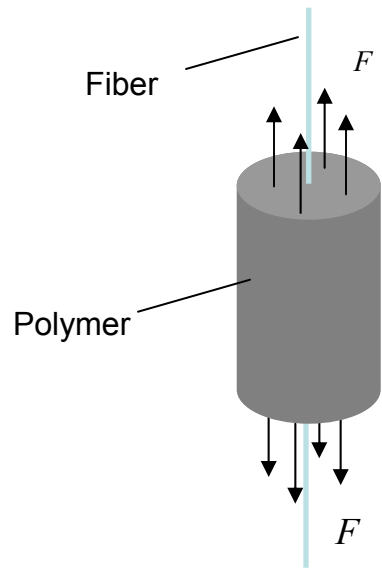
Fig. 3.12 Illustration of the polymer/FBG specimen subjected to uni-axial loading

The measured BW shift after applying the force is illustrated in Fig. 3.13.
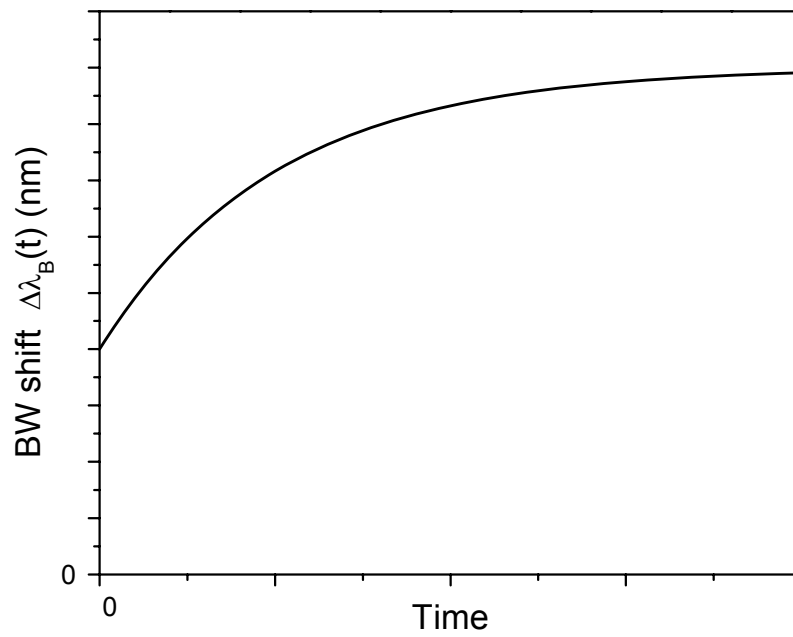
Fig. 3.13 Illustration of the measured BW shift after applying the instantaneous loading

It increases with time due to the creep of the polymer. Assuming that the BW shift is denoted as $\Delta\lambda_B(t)$, then the axial stain can be determined as

$$\varepsilon(t) = \frac{\Delta\lambda_B(t)}{\lambda_B(1-P_k)} \tag{3-33}$$

Substituting Eqn. (3-33) back into Eqn. (3-32) yields

$$C(t) = \left(\frac{\lambda_B(1-P_k)F}{\pi\left(\beta^2-1\right)a^2\Delta\lambda_B(t)} - \frac{E_f}{\beta^2-1} \right)^{-1} \tag{3-34}$$

From Eqn. (3-34), the compliance of the polymer can be determined from the measured BW shift at different temperatures.

Since the master curve of relaxation modulus is more widely used in commercial finite element analysis software such ANSYS, it is preferable to have the master curve of relaxation modulus rather than creep compliance. Through a de-convolution procedure [55], the measured creep compliance at each temperature can be transferred to the relaxation modulus at the corresponding temperature.

Recall that the creep compliance and relaxation modulus are related through the convolution integral as

$$\int_0^t C(t-\tau)E(\tau)d\tau = t \tag{3-35}$$

If the integral domain is divided into n sufficiently small intervals, $E(\tau)$ will not vary much over each interval and it can be approximated by an average value of $(E_i + E_{i-1})/2$ where E_i stands for $E(t_i)$. The same approximation is made for the compliance and Eqn. (3-35) becomes

$$\sum_{i=1}^{n} \frac{1}{4}(E_i + E_{i-1})(C_{n,i} + C_{n,i-1})(t_i - t_{i-1}) = t_n \tag{3-36}$$

where $C_{n,i}$ stands for $C(t_n - t_i)$. Separating the last term in the above equation yields

$$E_n = -E_{n-1} + \frac{4t_n - \sum_{i=1}^{n-1}(E_i + E_{i-1})(C_{n,i} + C_{n,i-1})(t_i - t_{i-1})}{(C_0 + C_{n,n-1})(t_n - t_{n-1})} \tag{3-37}$$

where C_0 is the short time limit of the creep compliance.

Equation (3-37) is a straightforward recursion relation which starts with $E_0 = 1/C_0$ and calculates each new value from previously obtained results. A creep compliance curve and corresponding transformed relaxation modulus curve in illustrated in Fig. 3.14.
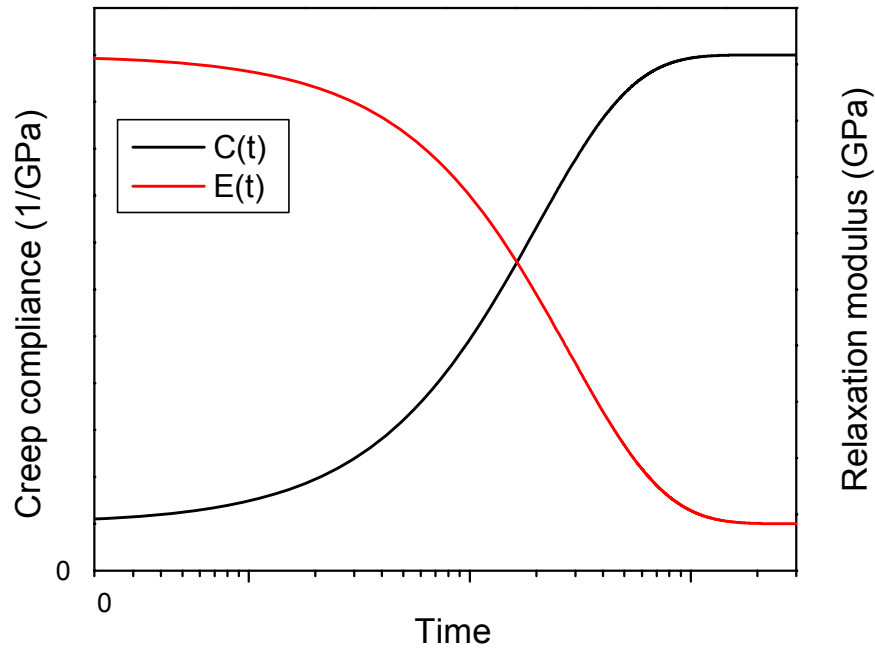
Fig. 3.14 Illustration of the creep compliance and relaxation modulus curves

The obtained relaxation modulus curves taken over a range of temperatures can be converted to a single master curve via the procedures introduced in section 2.5. The data is plotted in a double logarithmic coordinate. Data at a certain temperature is chosen as a reference and then the other curves are shifted horizontally. If the various curves can be made to overlap, the material is considered to be thermorheologically simple and the formed curve is the master curve.

For modeling purpose, the obtained master curve of relaxation modulus can be then fitted by the Prony series. The theoretical base of the Prony series lies in the generalized Maxwell model (or Wiechert model) which is shown in Fig. 3.15 [65]. As illustrated in the figure, the polymer is modeled by a parallel connection of an isolated spring (E_∞) and many spring-dashpot (Maxwell) elements. Each spring-dashpot has different relaxation time which is defined as

$$\tau_i = \frac{\eta_i}{E_i} \tag{3-38}$$

where η_i is the viscosity of the ith element and E_i is the modulus of the ith element. Many spring-dashpot elements are used because a real polymer does not relax with a single relaxation time. It has been found that simpler and shorter segments relax much more quickly than the longer ones, leading to a distribution of relaxation times. The Wiechert model illustrated in Fig. 3.15 can have as many spring-dashpot elements as are needed to approximate the distribution satisfactorily.
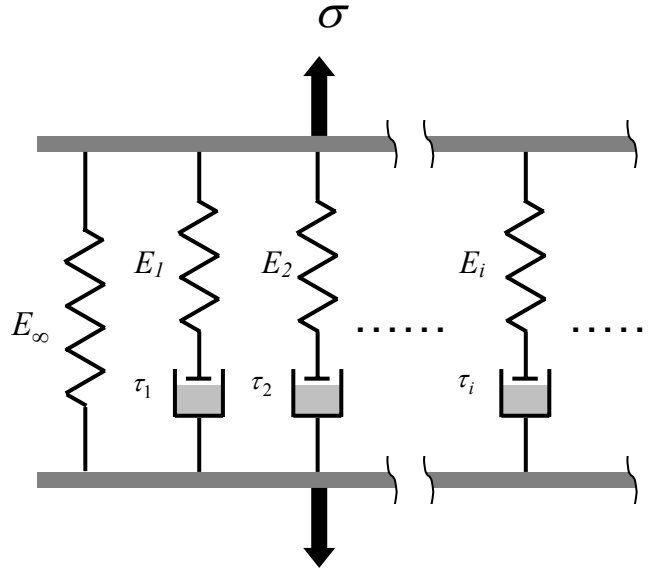
Fig. 3.15 Illustration of the generalized Maxwell model

The behavior of the ith element can be described by the differential equation

$$\dot{\varepsilon}_i = \frac{\dot{\sigma}_i}{E_i} + \frac{\sigma_i}{\eta_i} \tag{3-39}$$

With a constant strain of ε_0 imposed, the solution of Eqn. (3-39) will be

$$\sigma_i(t) = E_i \varepsilon_0 \exp\left(-\frac{t}{\tau_i}\right) \tag{3-40}$$

Adding the stress in every element together will yield the total stress

$$\sigma(t) = E_\infty \varepsilon_0 + \sum_{i=1}^{n} E_i \varepsilon_0 \exp\left(-\frac{t}{\tau_i}\right) \tag{3-41}$$

where n is the number of spring-dashpot elements. Then the relaxation modulus $E(t)$ can be determined to be

$$E(t) = \frac{\sigma(t)}{\varepsilon_0} = E_\infty + \sum_{i=1}^{n} E_i \exp\left(-\frac{t}{\tau_i}\right) \tag{3-42}$$

78

Equation (3-42) is the called Prony series representation of relaxation modulus. A pair of E_i and τ_i are referred to be a Prony pair. With Eqn. (3-42), the obtained master curve of relaxation modulus can be fitted using nonlinear regression scheme. Then the results can be imported directly into FEM codes for the modeling of polymers' visco-elastic behavior.

Chapter 4 Measurement of Properties Evolutions

4.1 Experimental Setup

4.1.1 Specimen configurations

As elaborated in section 3.3, small specimen configurations are desired to minimize the effect of the heat generation. However, the small configurations produce proportionally small deformations of the polymer/FBG assembly and thus reduce the signal of the FBG. A numerical analysis is conducted to select an optimum pair of configurations for implementation of the proposed method.

C-2 configuration

Assuming the effective chemical shrinkage increment is linearly proportional to the curing extent increment [4, 17], an inverse numerical procedure to calculate the property evolutions described in section 3.3.2 can be used to simulate the curing induced BW shift in different specimen configurations. The calculation is based on Eqn. (3-11), repeated here,

$$\Delta\lambda_B^d = \frac{1}{E_f}\left\{\left[1-\frac{n^2}{2}\left(P_{12}-(P_{12}+P_{11})\upsilon_f\right)\right]\sigma_{zz}^f - \left[2\upsilon_f+\frac{n^2}{2}\left((1-\upsilon_f)P_{11}+(1-3\upsilon_f)P_{12}\right)\right]\sigma_{rr}^f\right\}\lambda_B$$

(3-11)

As shown in the above equation, both modulus and effective chemical shrinkage are required in the calculation. The total chemical shrinkage was firstly obtained from the values reported in the literature which range from 0.2% to 4%; 0.9% was selected as the most representative value [14, 16, 18, 20, 22, 23, 25, 27, 28, 30, 104, 105]. Then considering the typical gelation point is 0.5 for polymers [106-110], an effective chemical

shrinkage of 0.45% was used in the simulation. Since we are only interested in the final BW shift, for numerical simplicity, the effective chemical shrinkage is assumed to increase from zero to 0.45% linearly. To model the modulus, the well know percolation theory [111, 112] was employed which can be written as

$$
E(t) = \begin{cases} 0 & \text{if } t < t_{gel} \\ E_\infty^0 \left(\dfrac{p^2 - p_{gel}^2}{1 - p_{gel}^2} \right)^{8/3} & \text{if } t \geq t_{gel} \end{cases}
\tag{4-1}
$$

where E_∞^0 is the equilibrium modulus when the polymer is fully cured and p is the curing extent. Polymers develop a small modulus at the end of the curing especially when they are cured at elevated temperature. Depending on the material, E_∞^0 can vary from tens of MPa to several GPa. A value of 100 MPa was chosen for the calculation, which was a low end of the reported moduli [49, 112-118].

The simulated BW shift for the different cases of b/a are plotted in Fig.4.1. It will be shown later that the BW measurement resolution of the employed experimental system is 5 pm in practice. Considering a minimum of 10 segments (10 data points) to describe the nonlinear nature of two property evolutions faithfully, the required minimum BW shift should be at least 500 pm for the 90% engineering accuracy; i.e.,

$$
10 \text{ segments} \times \frac{5 \text{ pm}}{10\%} = 500 \text{ pm}
$$

From Fig. 4.1, the smaller specimen configuration (C-2) is chosen to be $\beta_2 = 20$ (denoted as 20X) in the implementation.
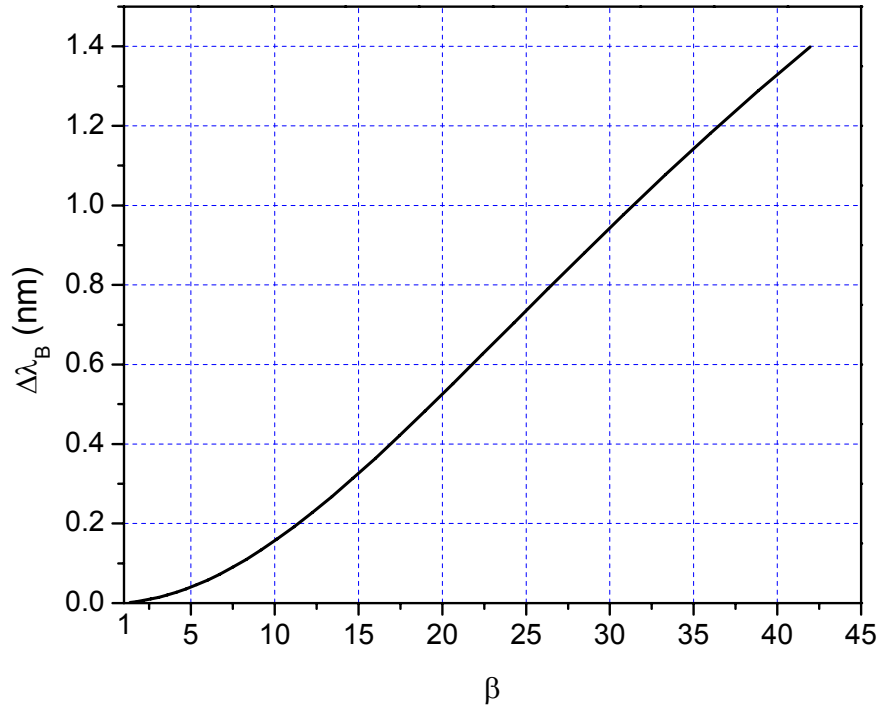
Fig. 4.1 Simulation results of BW shift in different configurations

C-1 configuration

For the given C-2 configuration, Eqn. (3-23) clearly indicates that it is desired to make the ratio of the BW shifts between two configurations large for the high sensitivity. Figure 4.2 shows numerical solutions obtained for the ratio of the BW shift between various C-1 configurations and C-2 configuration ($\beta_2 = 20$) as a function of modulus. A wide range of modulus (from 100 MPa to 1 GPa), E_s, is considered in the analysis.
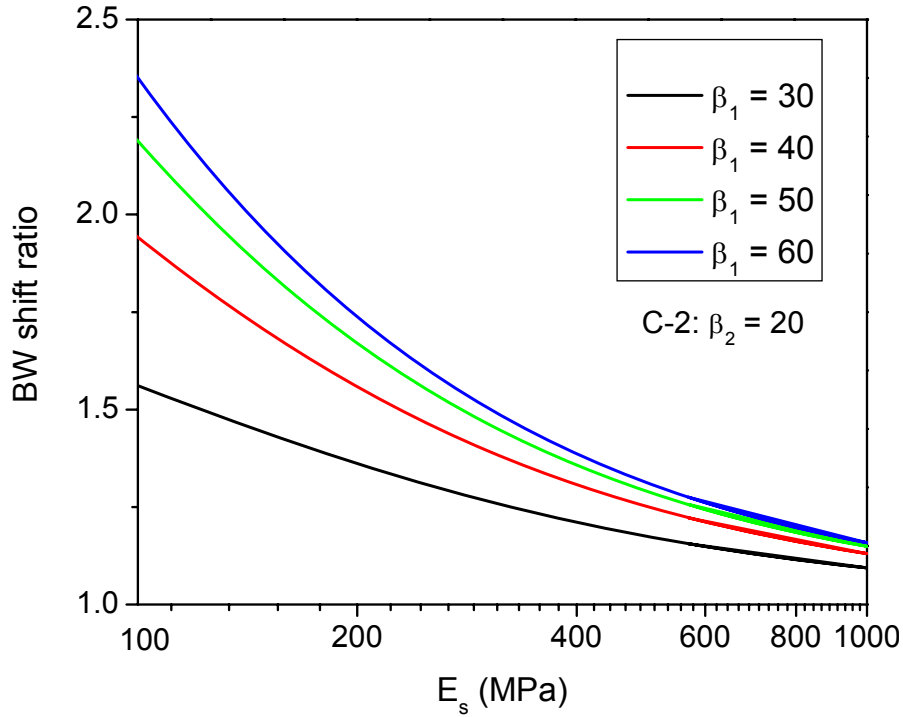
Fig. 4.2 BW shift ratio versus modulus of various C-1 configurations

Figure 4.2 clearly shows that the ratio is sensitive to the modulus of interest and the larger C-1 configuration yields better sensitivity. There is large improvement from β_1 = 30 to β_1 = 40, but the improvement gets smaller when C-1 dimension continues to increase. The accuracy of the measurement can be enhanced in larger C-1 configuration. However, as explained before, there will be more accumulated heat generation in the larger configuration, which does not produce the uniform curing temperature distribution. The BW sensitivity and the curing-induced heat generation become two trade-off factors.

The numerical procedure introduced in section 3.3.1 was repeated for three different cases of β_1 = 30, β_1 = 40, β_1 = 50 and β_1 = 60 to illustrate the trade-off. Identical material parameters were used; $k = 0.25 \ W/m \cdot K$, $C_p = 1500 \ J/kg \cdot K$, $A = 29.1$/s, $E_a =$

35.8 kJ/mol and $\Delta H = 300$ J/g. The normalized center temperature profile is shown in Fig. 4.3, plotted together with $\beta_1 = 200$ result (see Fig. 3.6) for a reference.
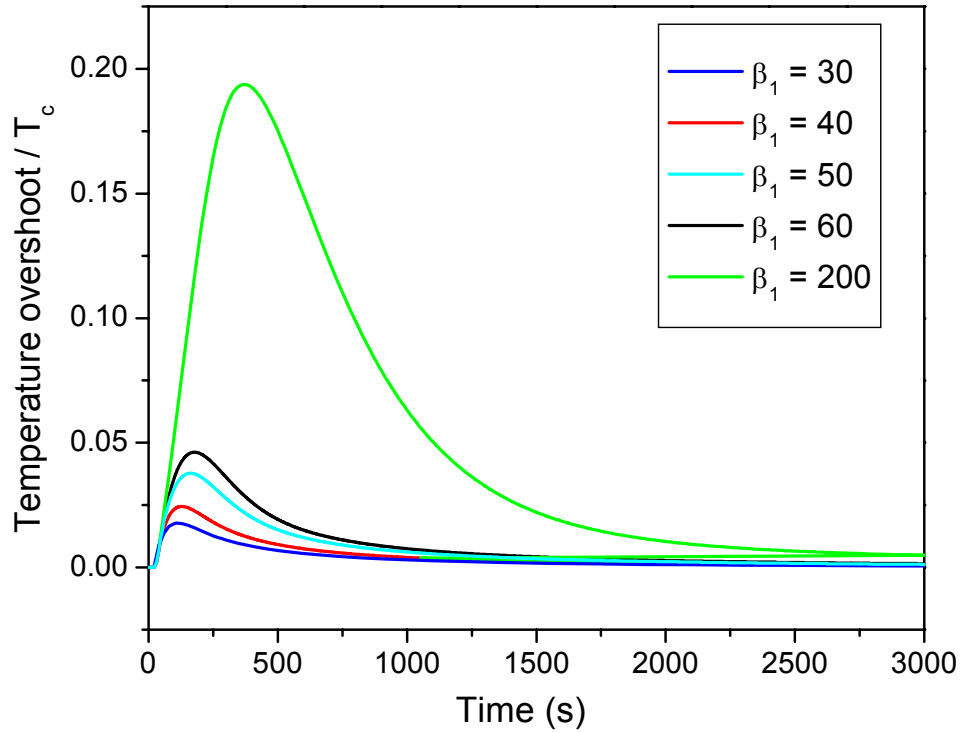
Fig. 4.3 Center temperature profile for three different cases of $\beta_1 = 30$, 40 50, 60 and 200

More importantly, the curing extent evolution of the material of $\beta_1 = 30$, 40, 50 and 60 is plotted in Fig. 4.4, in addition to that of $\beta_2 = 20$ for a comparison. The calculation of the curing extent evolution for different β_1 follows the numerical procedure introduced previously in section 3.3.1, or say though Eqns. (3-17) to (3-19).

From Fig. 4.3 and Fig. 4.4, it can be seen that the maximum temperature overshooting in configuration $\beta_1 = 30$ and 40 are close and they are half of that in configuration $\beta_1 = 50$ or 60. The curing speed in the configuration of $\beta_1 = 30$ and 40 are consistent with that in configuration C-2 ($\beta_2 = 20$), whereas the material of $\beta_1 = 50$ and 60 are cured faster. Considering the assumption of consistent curing in two configurations

used to derive the governing equations and better sensitivity of $\beta_1 = 40$ than that of $\beta_1 = 30$, the C-1 specimen configurations are chosen to be $\beta_1 = 40$ (denoted as 40X) in the implementation.
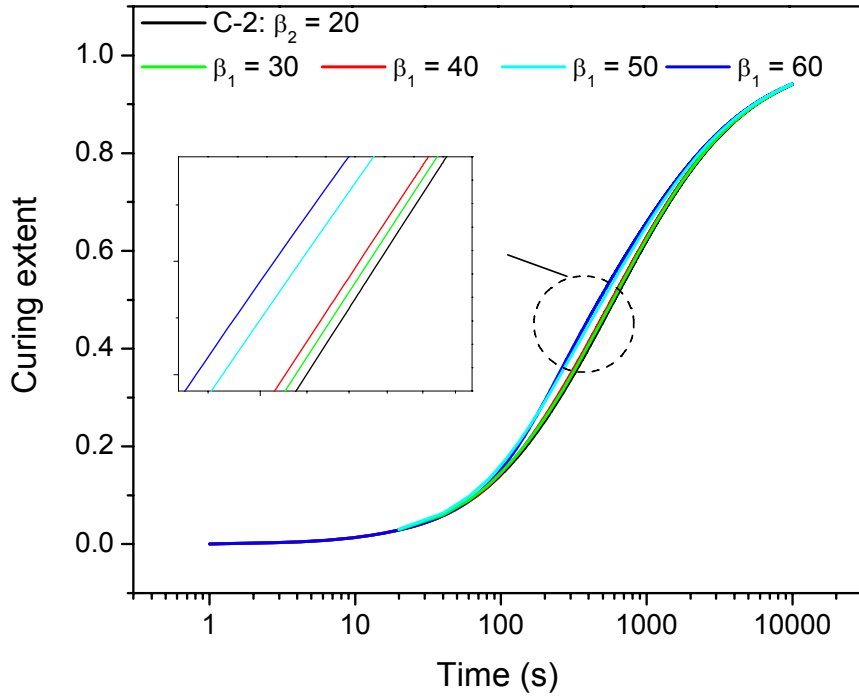
Fig. 4.4 Curing extent evolution of different specimen configurations

Length of configurations

The length of the specimen is also critical because the generalized plane strain condition is assumed in the derivation of governing equations. If the specimen is not long enough, the strain field where the Bragg gratings are located (in the middle of the specimen) will be affected due to the free-edge effect. To investigate the effect of the specimen length, the strain field of specimens with various lengths was simulated using the finite element method. In the calculation, a chemical shrinkage of 1% is used. The total length of the specimen is 30 mm with a configuration of $\beta_1 = 40$. Large specimen

configurations were studied because the free-edge effect is more pressing in configuration C-1 than C-2. The modulus of the polymer evolves from zero to the final value during the curing and 1 MPa was used to study the free-edge effect in the beginning stage of the curing. The figure 4.5a shows the contour plot of the strain field when the polymer has a modulus of 1 MPa. From the figure, it can be clearly been that the strain field of the specimen is affected a certain distance from the edge. In Fig. 4.5b, the distribution of axial strain from the middle of the specimen is plotted in which the polymer has a modulus of 1 MPa or 1 GPa.

(a)
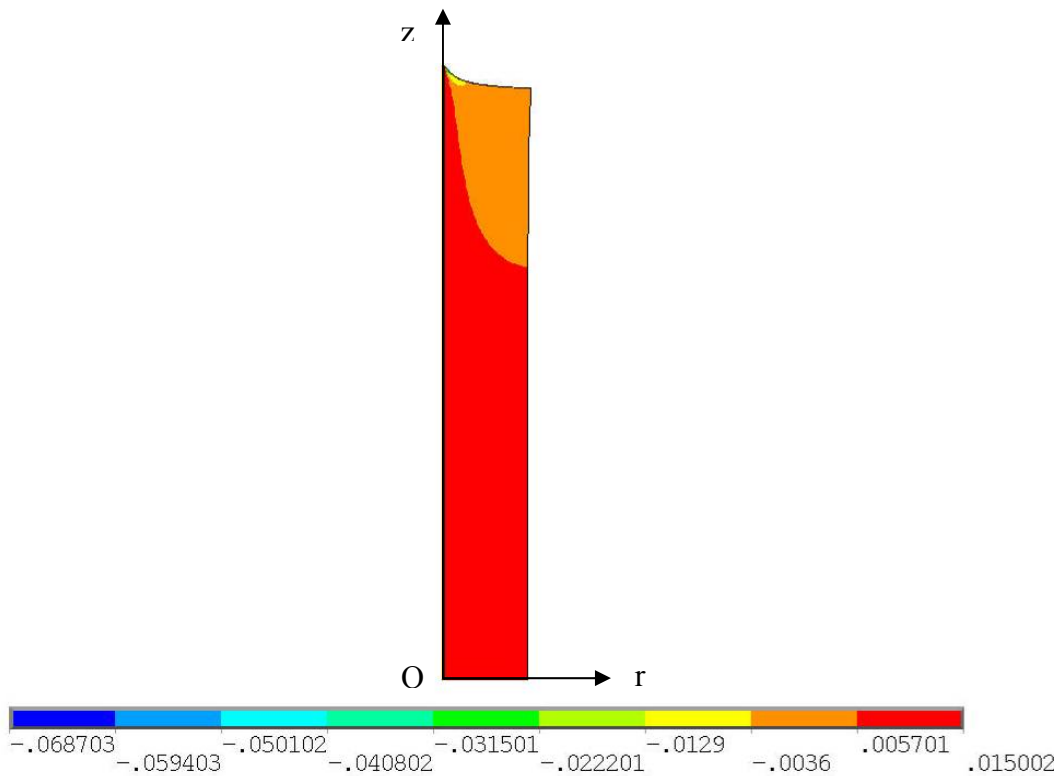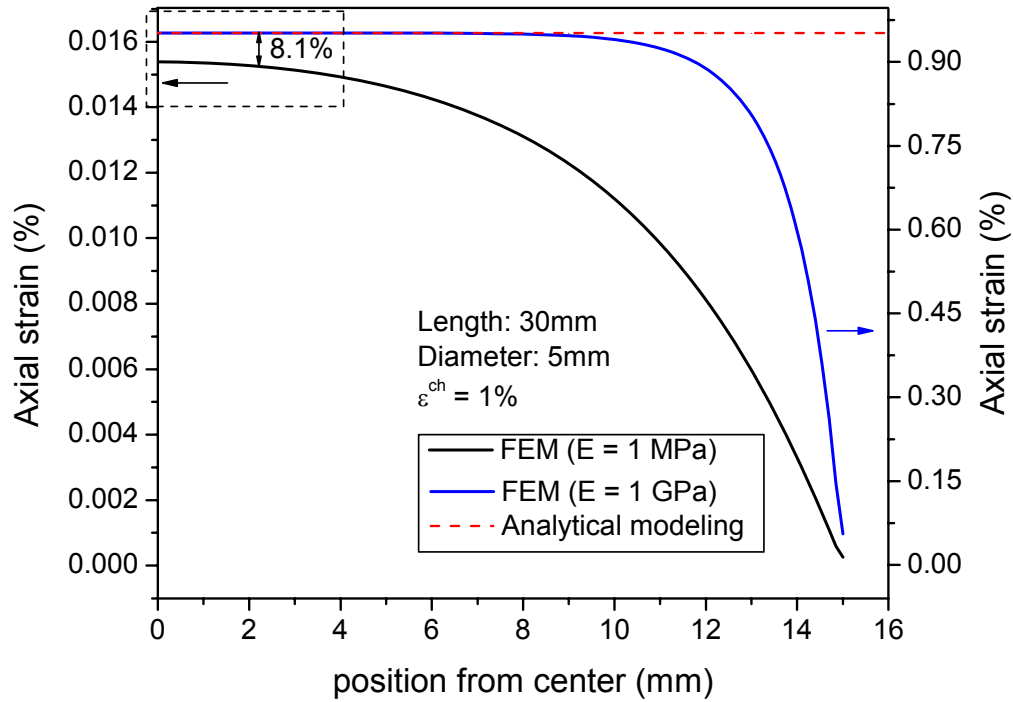
Fig. 4.5 (a) Contour plot of the axial stain field (polymer modulus: 1 MPa);

(b) Distribution of the axial strain along the specimen length

Two observations can be made from Fig. 4.5. Firstly, when the polymer has a large modulus like 1 GPa, the axial strain is consistent with the theoretical prediction at the middle. When the polymer has a tiny modulus like 1 MPa, the axial strain is off from the theoretical prediction even at the middle point. Secondly, the strain decays faster when the polymer has smaller modulus. Both facts indicate that the specimen is more susceptible to the free-edge effect when the polymer has smaller modulus.

It is important to assure that the strain field around the Bragg gratings is not affected by the free edge. The axial strain of the fiber at the edge of the Bragg gratings was simulated using FEM when the specimen has finite lengths. The polymer was

assumed to have a modulus of 1 MPa in the calculation. Then the simulation results were

compared with the theoretical prediction which is based on the generalized plane strain

assumption. The deviations between the simulation results and theoretical results were

calculated and plotted in Fig. 4.6 as a function of the specimen length. In the figure, the

specimen length is normalized by the total length of Bragg gratings.
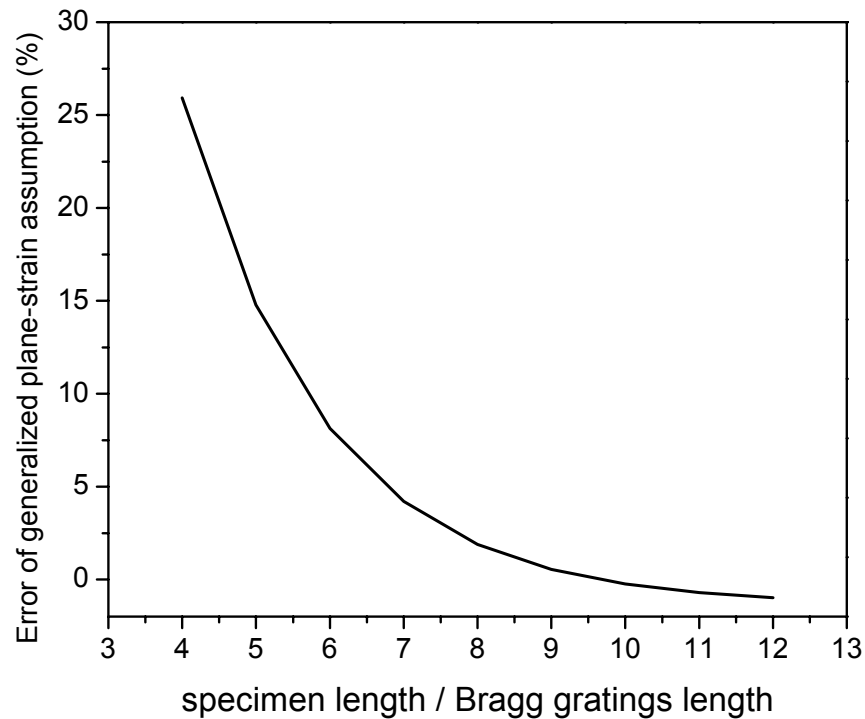
Fig. 4.6 Deviation from actual axial strain when introducing generalized plane-strain
assumption

It is seen from the figure that when the length of the specimen is short, the error caused

by the generalized plane strain assumption can be as large as 25%. When the specimen

length is more than ten times larger than the gratings length, the error can be reduced to

less than 1%. In the implementation of this technique, the mold will be designed in such

a way that the specimen is 10 times longer than the gratings.

4.1.2 Mold design and sample preparation

This study employs the cylindrical polymer/FBG assembly. A mold was designed to fabricate specimens with the desired shape. As shown in Fig. 4.7, the mold consists of a base, two caps and a silicone rubber tube.
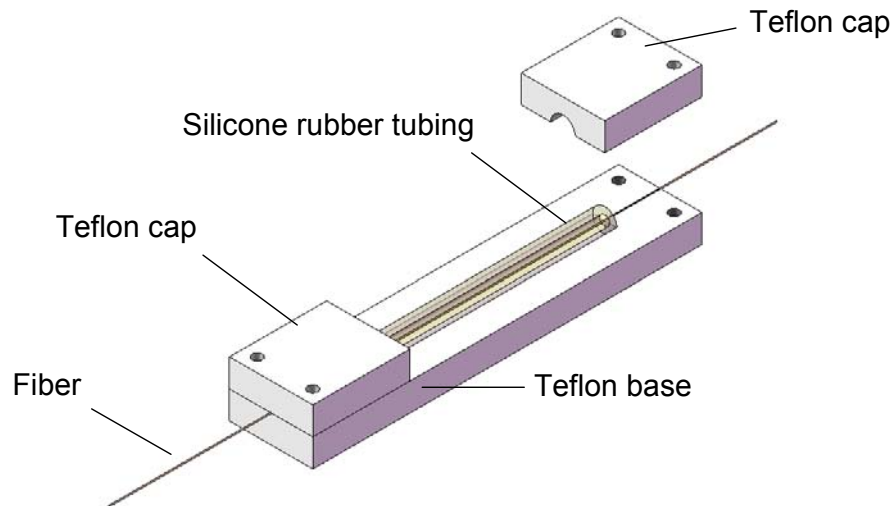
Fig. 4.7 Schematic drawing of the mold design for fabrication of the specimen

The base and two caps were made of Teflon. Teflon can resist high temperature while not adhering to polymers. Very fine grooves were fabricated along the centerline in the base mold to hold an FBG. The material is cured in a silicone rubber tube, forming the cylindrical shape. The modulus of silicone rubber is so low (1-2 MPa) that the constraint applied to the tested material is negligible. Another advantage of using silicone rubber is that it does not adhere to polymers. After the curing, the polymer specimen can be easily separated from the tube and readily used for further testing.

The diameter of the FBG used in the experiment is 125 μm. Considering the practicality and commercial availability of silicone rubber tubes, in this study, the inner

diameter of the tube is 3/16'' in specimen configuration C-1 and 3/32'' in configuration C-2; which leads to $\beta_1 = 38$ and $\beta_2 = 19$. The total length of Bragg gratings and the length of the polymer specimen are 5 mm and 50 mm, respectively.

A fine-wire thermal couple is also embedded to monitor the temperature; it is embedded next to the fiber but away from the Bragg gratings so that the inclusion effect was minimized. The following procedure was used to fabricate a specimen:

1. Place an FBG through a silicone rubber tube;

2. Secure the FBG along the groove of the Teflon base;

3. Assemble the bottom Teflon cap;

4. Inject a polymer of interest into the tube;

5. Embed a fine-wire thermal couple;

6. Assemble the top Teflon cap;

7. Cure the polymer.

The final shape of a specimen is illustrated in Fig. 4.8.
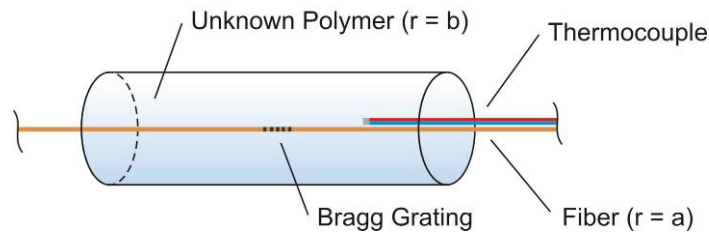
Fig. 4.8 Schematic illustration of a specimen

4.1.3 FBG data acquisition system

An FBG data acquisition system is illustrated in Fig. 4.9. The system consists of an FBG interrogation system (FBG-IS), an environmental chamber and a PC. The Bragg wavelength is measured by a commercial FBG interrogation system (sm125-500, Micron Optics), which has a resolution of 1 pm and repeatability of 0.2 pm. A computer-controlled environmental chamber (EC11A, Sun Electronics Systems) controls the temperature. Experimental results are saved in a personal computer as the experiment progresses.
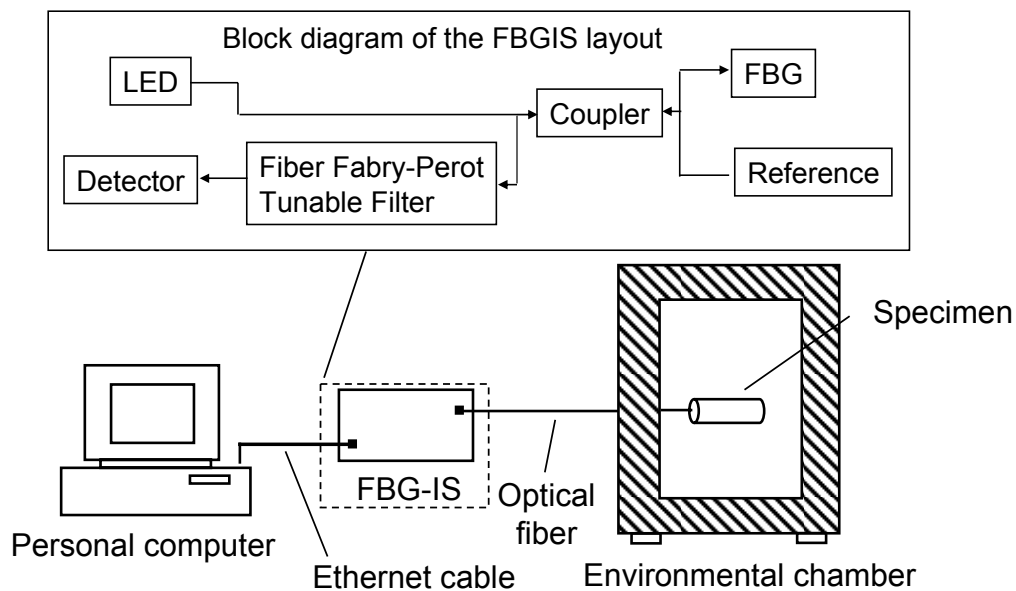
Fig. 4.9 Schematic illustration of the experimental setup

The insert of Fig. 4.9 shows a block diagram of the FBG-IS layout. An LED illuminates the FBG, which reflects the light at the Bragg wavelength. The fiber Fabry-Perot tunable filter (FFP-TF) scans the reflected light from the FBG as well as the

picoWave reference alternatively. The detected signals are then converted to wavelengths. The picoWave is the multi-wavelength reference of the FBG interrogation system that consists of a Fiber Fabry-Perot Interferometer, a wavelength marker of a fiber Bragg Grating, and a built-in thermo electric controller for thermal stability. It enables real-time wavelength calibration to picometer accuracy.

4.2 Experimental Results and Data Analysis

4.2.1 Calibration of FBGs

Before being embedded into the polymer substrate, the FBG was calibrated to determine the "*intrinsic*" BW shift, $\Delta\lambda_B^i$. Specifically, the bare FBG was placed in the environmental chamber and the BW shift was documented as a function of temperature. A representative experimental result is shown in Fig. 4.10.
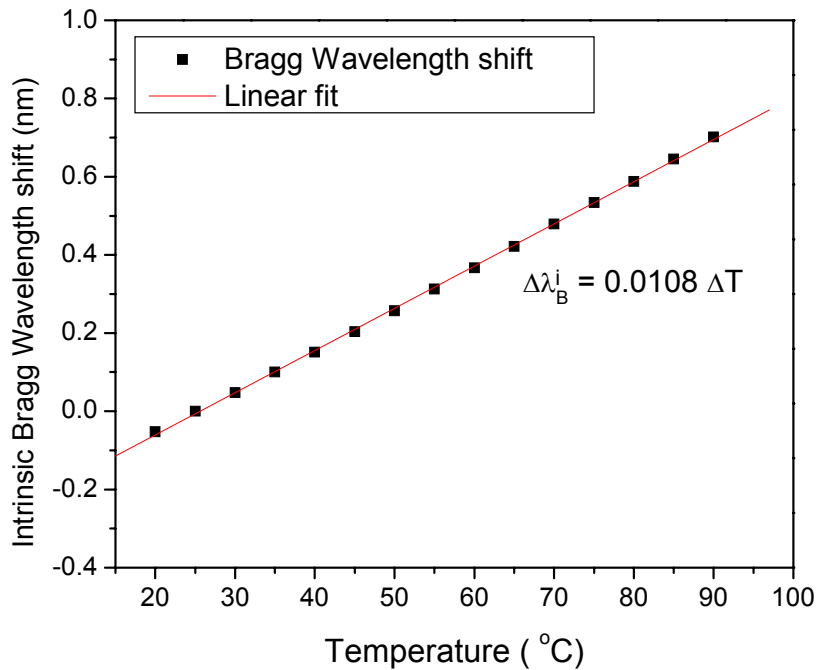
Fig. 4.10 Bragg wavelength shift of a bare fiber as a function of temperature

For the test fiber, the slope of the intrinsic BW shift with temperature change is determined to be 0.0108 nm/°C. The result agrees well with the theoretical value of $0.0104 \, nm/°C$ [119]. Furthermore, for the given refractive index of $n_{eff} = 1.457$ [74] and fiber CTE of $\alpha_f = 0.55 \, ppm/°C$ [120-122], the thermo-optical constant was determined to be $\dfrac{dn}{dT} = 9.4 \times 10^{-6}/°C$ using Eqn. (3-6). The thermo-optical constant also agrees well with earlier results [121, 123].

Strain-optic coefficients, P_{ij}, are also important intrinsic parameters of FBGs. There are two different sets of data for glass FBGs available in the literatures: $P_{11} = 0.113$, $P_{12} = 0.252$ [78, 120, 124, 125] and $P_{11} = 0.121$, $P_{12} = 0.270$ [70, 126, 127]. It is well known that the Poisson's ratio of the fiber, υ_f, is 0.17 [70, 120].

Using Eqn. (2-22), the effective strain-optic constant, P_k, is calculated to be 0.198 and 0.216 from the first and second set of P_{ij}, respectively. In the calibration experiment of P_k, a dead weight was applied to an FBG. The dead weight induced the strain in the fiber and resulted in a shift in the Bragg wavelength. By measuring the BW before and after applying the dead weight, P_k can be calculated using Eqn. (2-21). The experimental results are shown in Table 4-1

Table 4-1 Calibration results of P_k

Dead weight	FBG diameter	Initial BW	Final BW	BW shift
107.62 g	160 μm	1550.279 nm	1551.667 nm	1.373 nm

When 73.1 GPa [128] and 3 GPa [129] were used for Young's modulus of the fiber and polyimide, P_k was determined to be 0.219. It should be noted that the calibration results

agree well with the second prediction result listed above and $P_{11} = 0.121, P_{12} = 0.270$ is to be used in this study.

4.2.2 Evolutions of effective chemical shrinkage and modulus

The proposed method was implemented with three different polymeric materials. They include a high filler ratio underfill material (UF-1, 65% filler ratio), a medium filler ratio underfill material (UF-2, 40% filler ratio) and a pure epoxy resin (Epoxy-1, Epichlorohydrin phenol formaldehyde). The effective chemical shrinkage and modulus evolutions were measured and the results are summarized in the following sections.

4.2.2.1 Results of material UF-1

The FBGs were calibrated before they were mounted on the mold. The bare FBGs were placed in the environmental chamber and the BW shift was documented as a function of temperature. Experimental results of two fibers used in C-1 and C-2 are shown in Fig. 4.11. The intrinsic BW shift has a linear relationship with ΔT

$$\Delta \lambda_B^i \big|_{C-1} = 0.0118 \cdot (T - 175) \tag{4-2}$$

$$\Delta \lambda_B^i \big|_{C-2} = 0.0115 \cdot (T - 175) \tag{4-3}$$

where the reference temperature is 175°C.

After the FBG was aligned in the mold, the material UF-1 was injected into the silicone rubber tube. The specimen was then heated to 175°C at a ramp rate of 20°C /min and dwelled for 3.5 hours. The evolution of BW throughout the entire process was

94

recorded in both C-1 and C-2. The results of measured BW evolution and temperature profile are shown in Fig. 4.12.
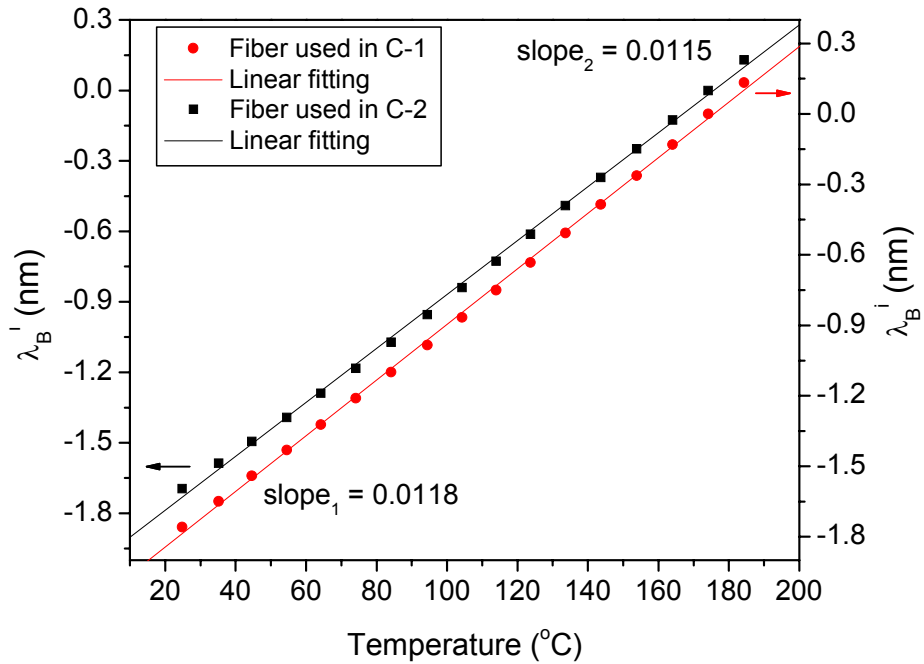
Fig. 4.11 Calibration results of FBGs used for the material UF-1
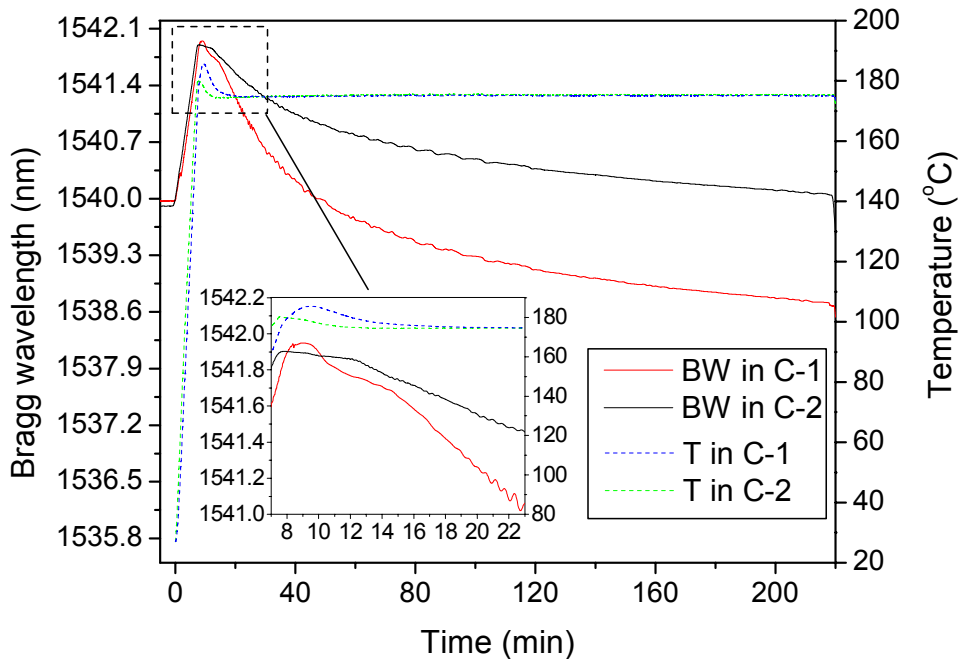
Fig. 4.12 Measured BW and temperature profile of the sample UF-1

95

Although optimized, a small temperature overshoot was observed in the experiment due to the exothermic polymerization process. This temperature overshoot can be seen more clearly in the insert of Fig. 4.12. A peak of the BW can be identified and its position is consistent with the peak temperature. Using Eqns. (3-5), (4-2) and (4-3), the BW compensated with the intrinsic part was calculated and the results are shown in Fig. 4.13. From the figure, a plateau area followed by an inflection point can be clearly seen in the BW curve of both configurations. In the plateau area, the polymer does not possess any mechanical strength and therefore cannot induce any deformation of the embedded FBG. After the polymer develops some modulus, the embedded FBG is deformed and the BW starts to decrease, which causes the inflection point.
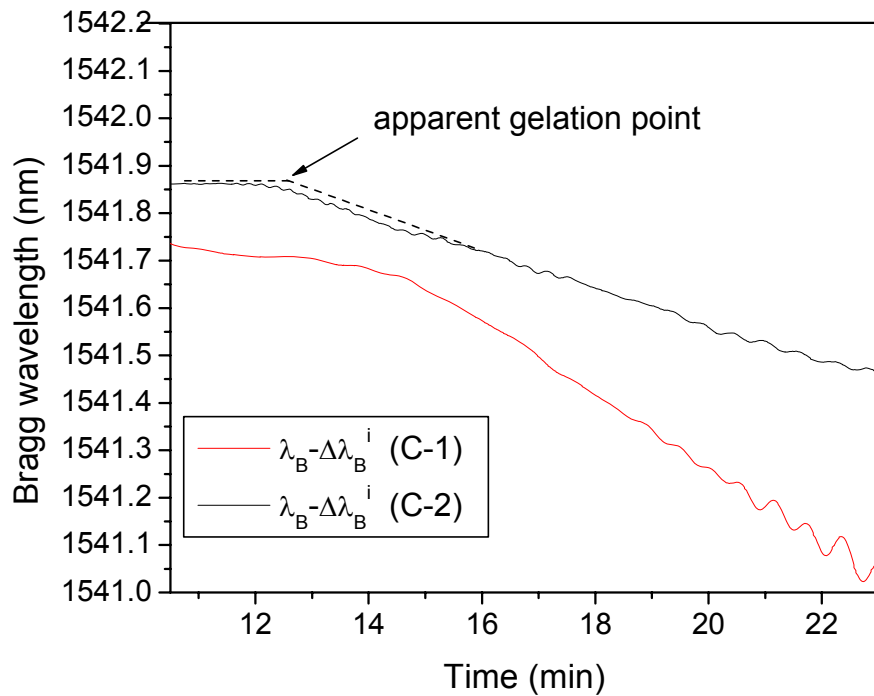
Fig. 4.13 The BW compensated with the intrinsic part of the sample UF-1

As the starting point of the inverse calculation of property evolutions, the *apparent gelation point* was determined as the crossing points of two linear lines that represent the plateau area and initial part of the decreasing area in C-2 curve. Configuration C-2 is chosen as the reference because the inverse calculation of Eqn. (3-23) requires nonzero BW shifts in both configurations. Since the specimen of configuration C-1 has a larger dimension of the polymer substrate and therefore larger volume stiffness, the configuration C-1 will pick up the polymer deformation earlier than the configuration C-2. In Fig. 4.12, the specimen temperature of C-2 is found to reach the curing temperature at the time of 7.0 min; in Fig. 4.12, the apparent gelation point is identified to occur at the time of 12.5 min. An apparent gelation time of 5.5 min is therefore determined for the test material.

The BW shifts after the apparent gelation point in both configurations are plotted in Fig. 4.14. An offset is made on the time axis so that the time at the apparent gelation point is zero (will be referred to as "effective time"). When the curing is completed, the magnitude of $\Delta\lambda_B^d$ in C-1 is approximately two times larger than that in C-2, as expected from the larger volume stiffness in C-1.

Following the numerical procedures described in section 3.3.2, the evolutions of effective chemical shrinkage and modulus were calculated from the data in Fig. 4.14. The results are shown in Fig. 4.15a and Fig. 4.15b, respectively. The effective chemical shrinkage accumulates much faster at the early stage of the polymerization, and gradually converges as the polymerization proceeds. The result indicates an expected gradual decrease in the polymerization speed.

Fig. 4.14 BW shift of the sample UF-1 after the apparent gelation point
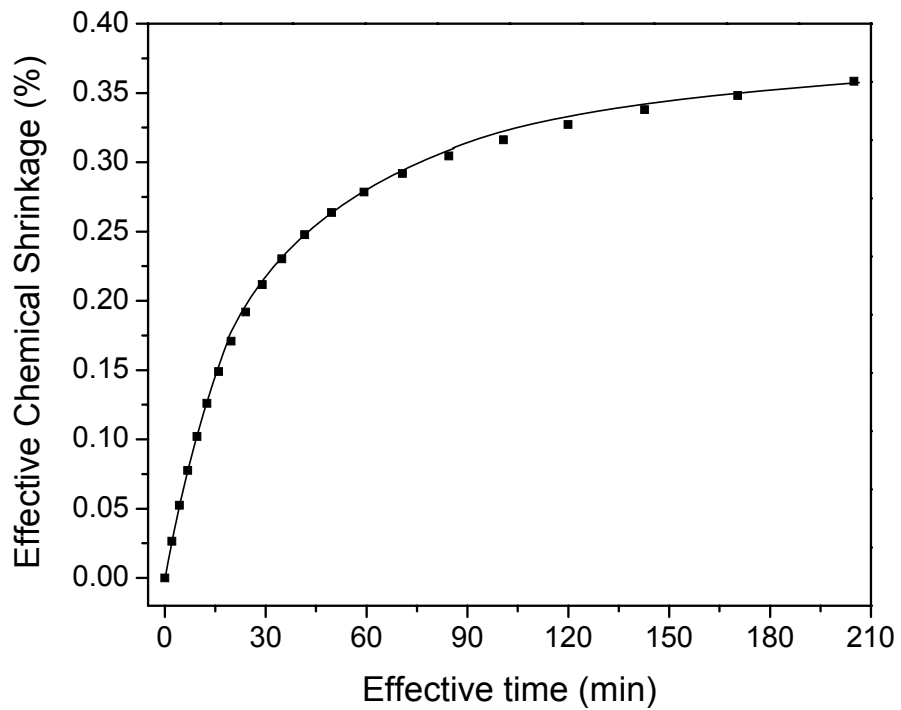
(a)
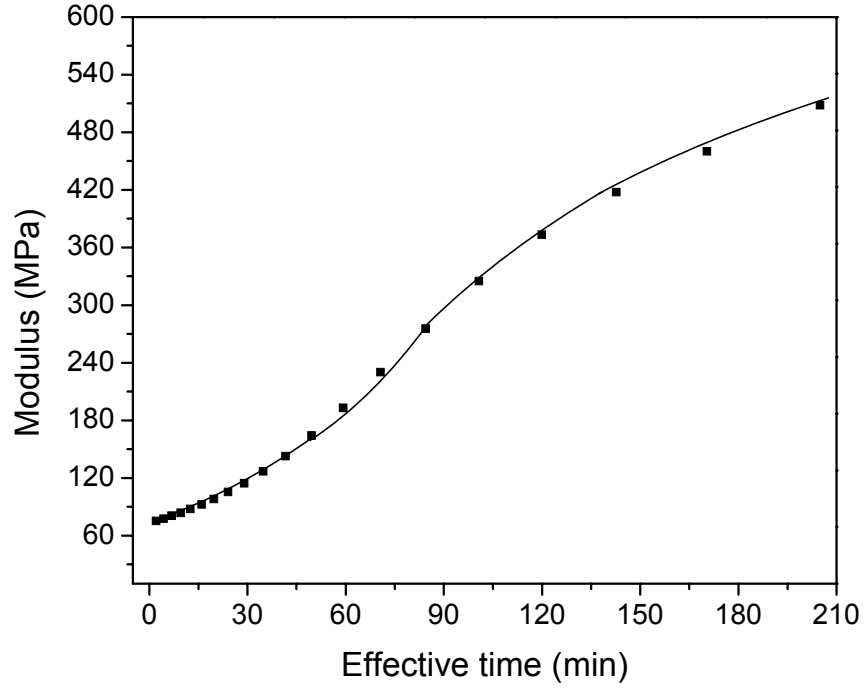
(b)

Fig. 4.15 Evolution properties of UF-1; (a) effective chemical shrinkage and (b) modulus

4.2.2.2 Results of material UF-2

The above experimental procedures were repeated for the material UF-2. The intrinsic BW shifts of two FBGs were calibrated and the results are:

$$\Delta \lambda_B^i \big|_{C-1} = 0.0118 \cdot (T - 175) \tag{4-4}$$

$$\Delta \lambda_B^i \big|_{C-2} = 0.0118 \cdot (T - 175) \tag{4-5}$$

where the reference temperature is 175°C.

After the FBG was aligned in the mold, the material UF-2 was injected into the silicone rubber tube. The specimen was then heated to 175°C at a ramp rate of 7.5°C/min and dwelled for 2.5 hours. The results of measured BW evolution and temperature profile are shown in Fig. 4.16. The same procedure used for UF-1 was followed and the

99

results are shown in (1) Fig. 4.17 for the BW compensated with the intrinsic part, (2) Fig. 4.18 for the BW shifts after the apparent gelation point and (3) Fig. 4.19 for the evolutions of effective chemical shrinkage and modulus.
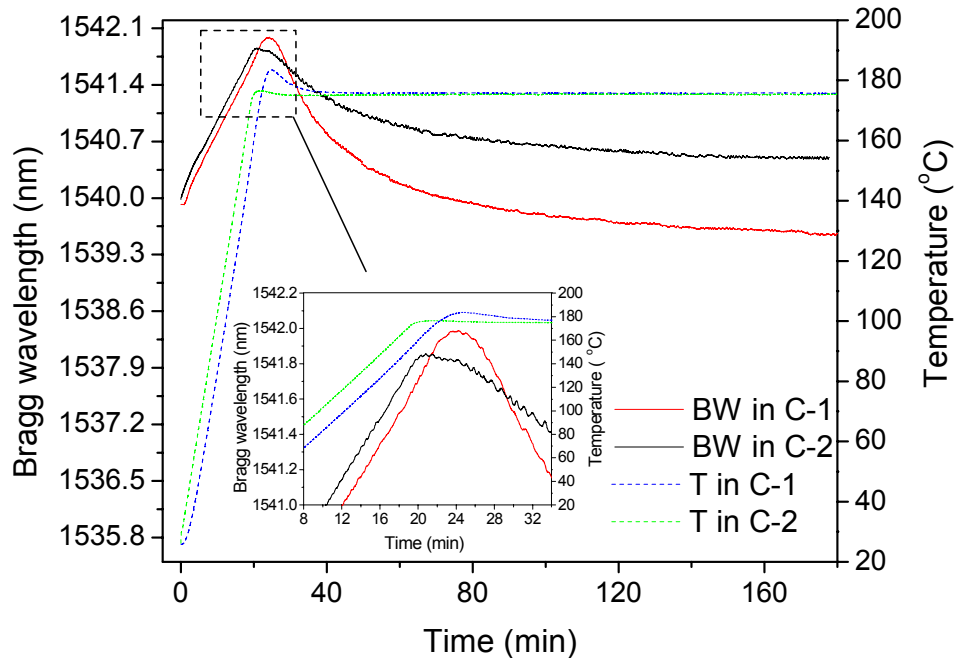
Fig. 4.16 Measured BW and temperature profile of the sample UF-2

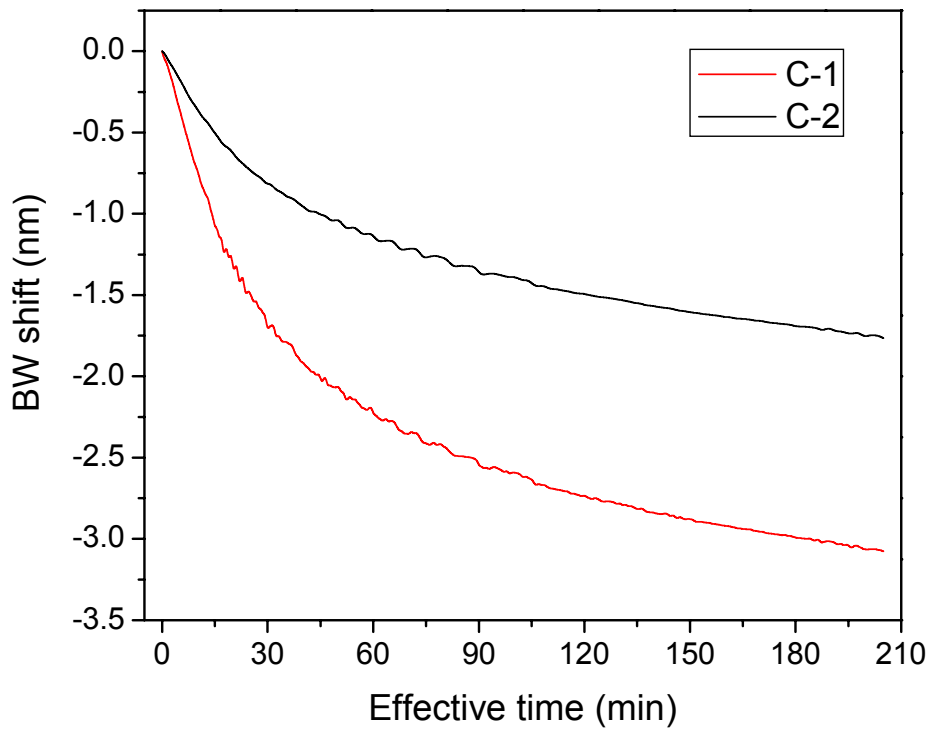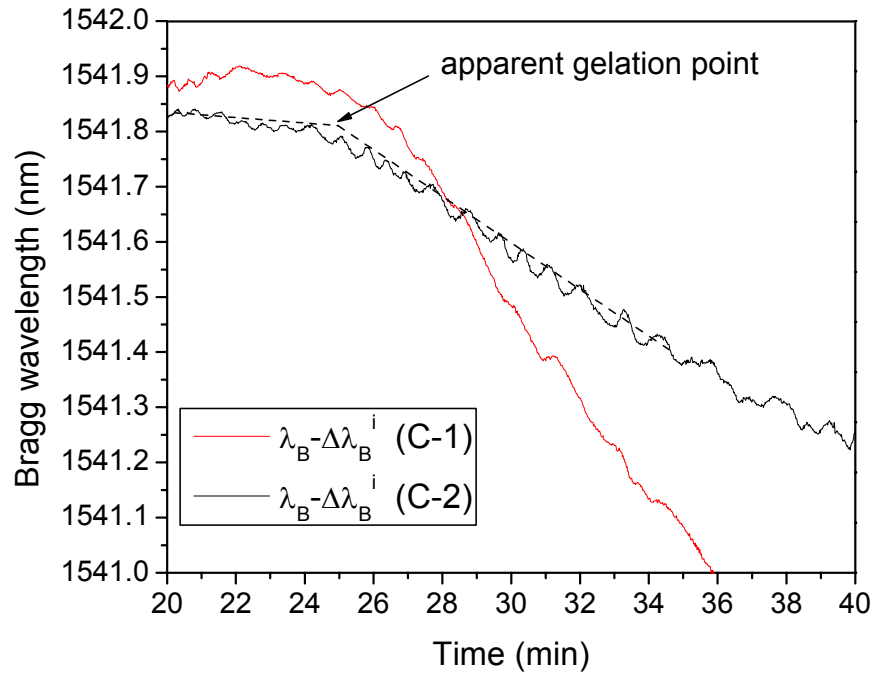Fig. 4.17 The BW compensated with the intrinsic part of the sample UF-2

Fig. 4.18 BW shift of the sample UF-2 after the apparent gelation point

(a)

(b)

Fig. 4.19 Evolution properties of UF-2; (a) effective chemical shrinkage and (b) modulus

A plateau area is also seen in the BW curve of both configurations (Fig. 4.17). The apparent gelation point located at the time of 24.9 min in C-2 curve while the temperature reaches the target at 19.8 min. An apparent gelation time of 5.1 min is determined for the material UF-2. Compared with UF-1, the material UF-2 has smaller effective chemical shrinkage and modulus.

4.2.2.3 Results of Epoxy-1

The calibration results of the intrinsic BW shifts of the FBGs in the Epoxy-1 test are found to be

$$\Delta\lambda_B^i\Big|_{C-1} = 0.0118 \cdot (T - 165) \tag{4-6}$$

102

$$\Delta\lambda_B^i\big|_{C-2} = 0.0119 \cdot (T - 165) \qquad\qquad (4\text{-}7)$$

with a reference temperature of 165°C. .

The polymer/FBG specimen was then heated to 165°C at a ramp rate of 60°C/min and dwelled for 5 hours. The results of the measured BW evolution and temperature profile are shown in Fig. 4.20. From the figure, it can be seen that there is virtually no temperature overshooting in both configurations and that the temperature stabilizes at the target temperature after only a few minutes. This indicates that the material cures slowly and that the heat generation rate is small.
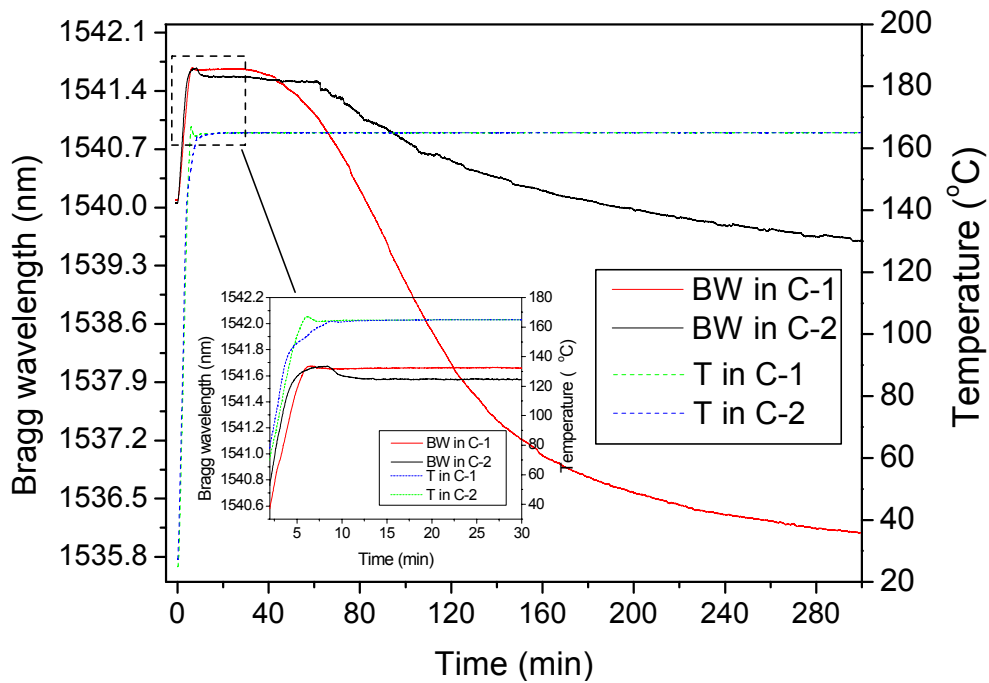
Fig. 4.20 Measured BW and temperature profile of the sample Epoxy-1

The BW compensated with the intrinsic part was calculated and the results are shown in Fig. 4.21. A long plateau area is identified in the C-2 BW curve. An apparent gelation time of 41 min is determined for the material.
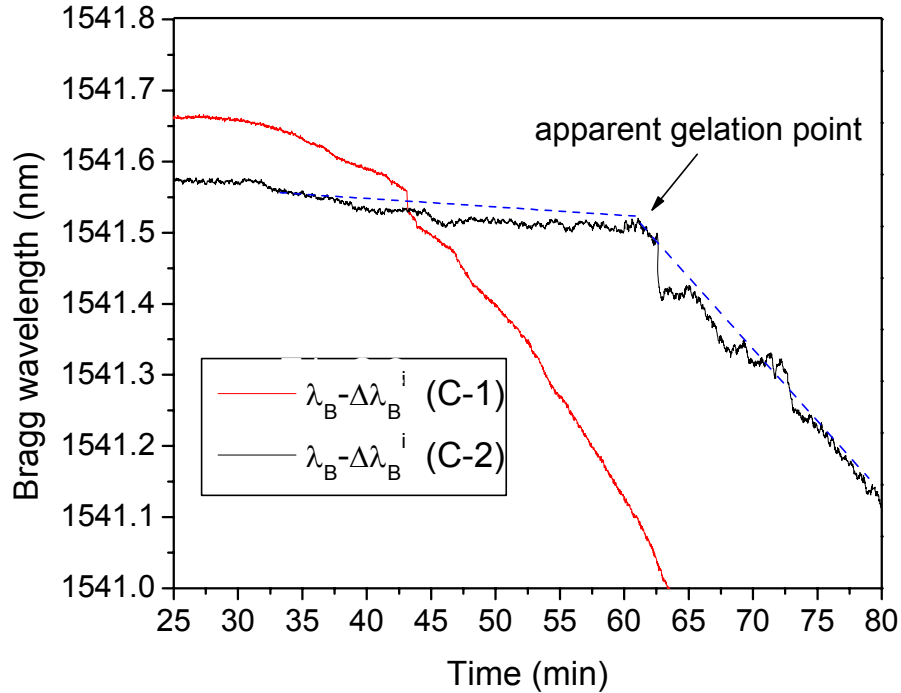
Fig. 4.21 The BW compensated with the intrinsic part of the sample Epoxy-1

The BW shifts after the apparent gelation point in both configurations are plotted in Fig. 4.22 and the results of the calculated effective chemical shrinkage evolution and modulus evolution are shown in Fig. 4.23a and Fig. 4.23b, respectively. Compared with the underfill material UF-1 and UF-2, this pure epoxy resin shows much larger chemical shrinkage.
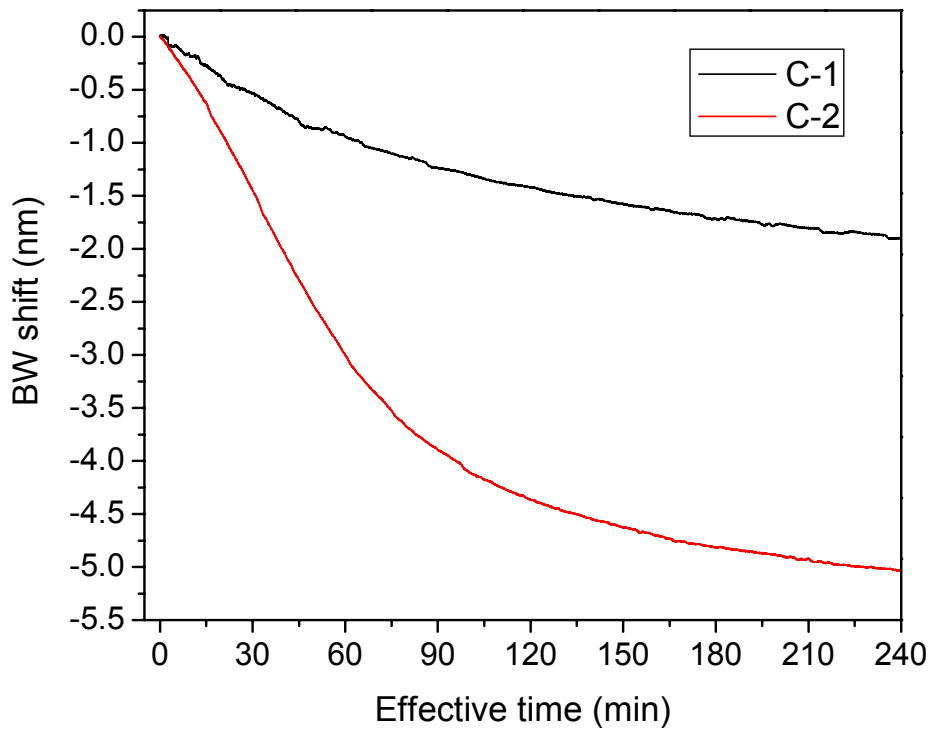
Fig. 4.22 BW shift of the sample Epoxy-1 after the apparent gelation point

(a)

105
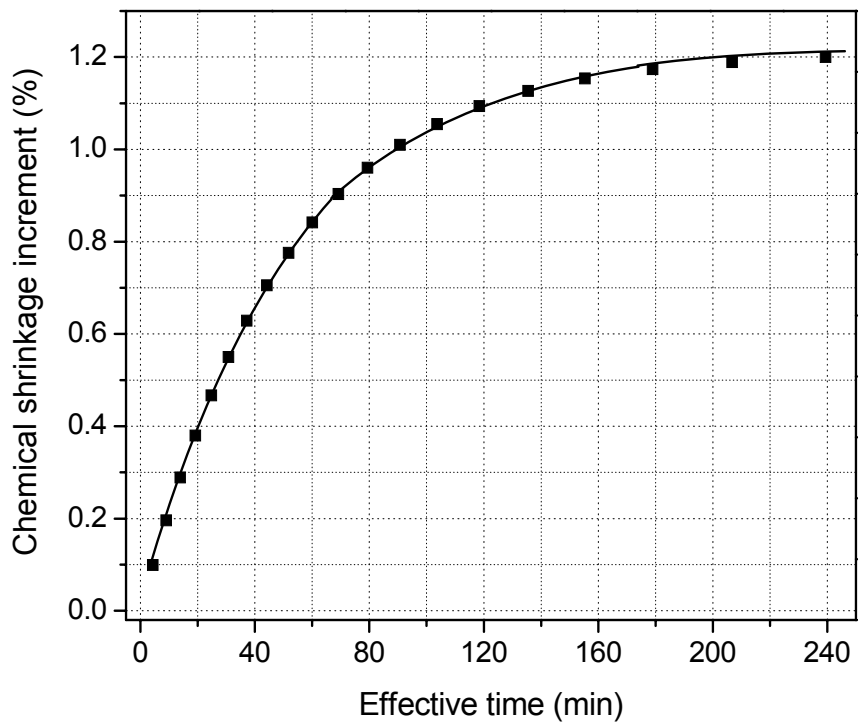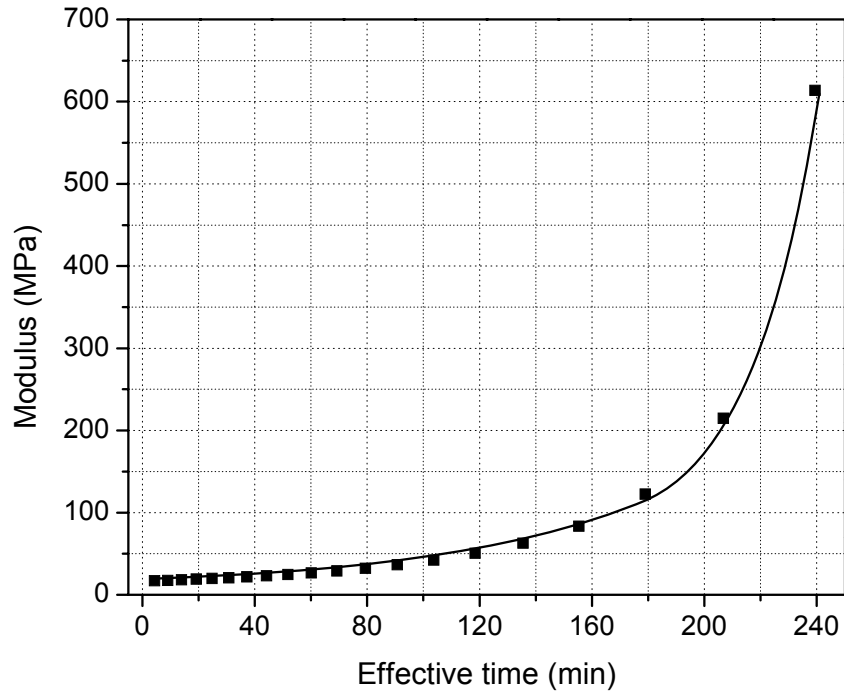
(b)

Fig. 4.23 Evolution properties of Epoxy-1;

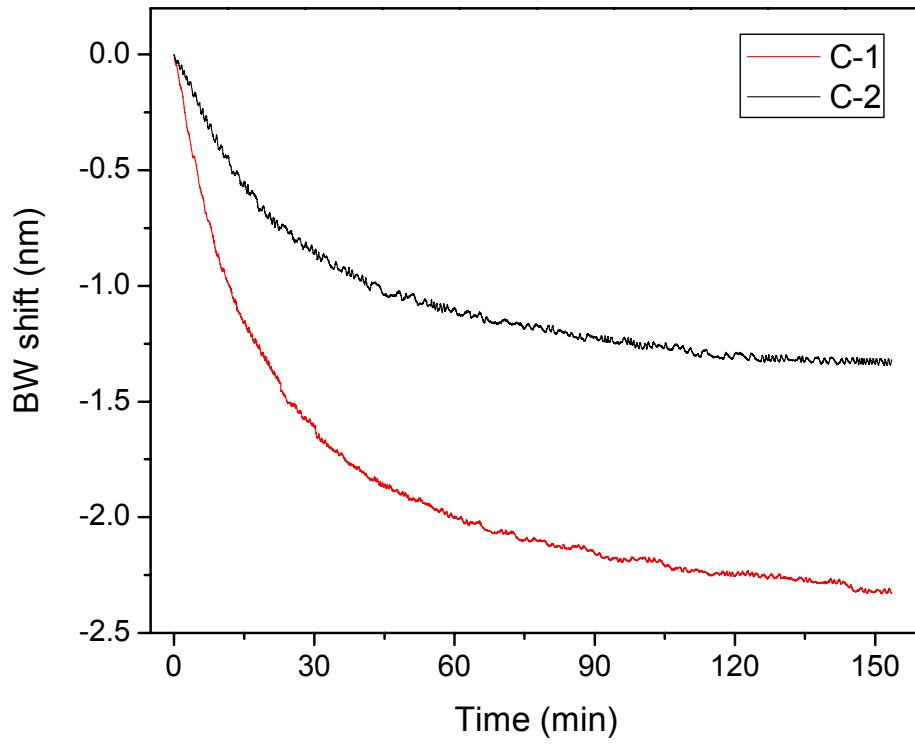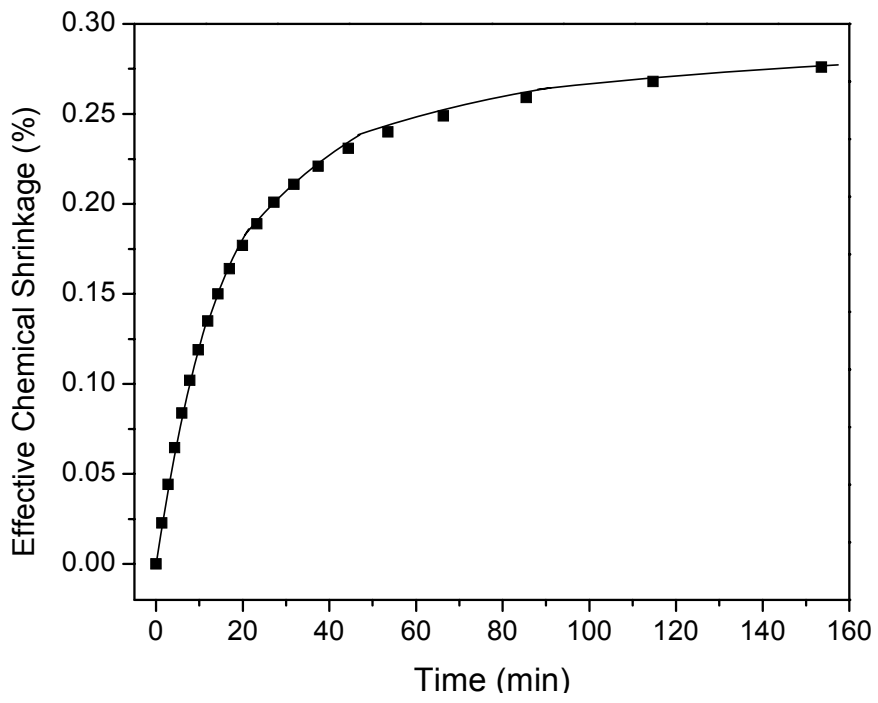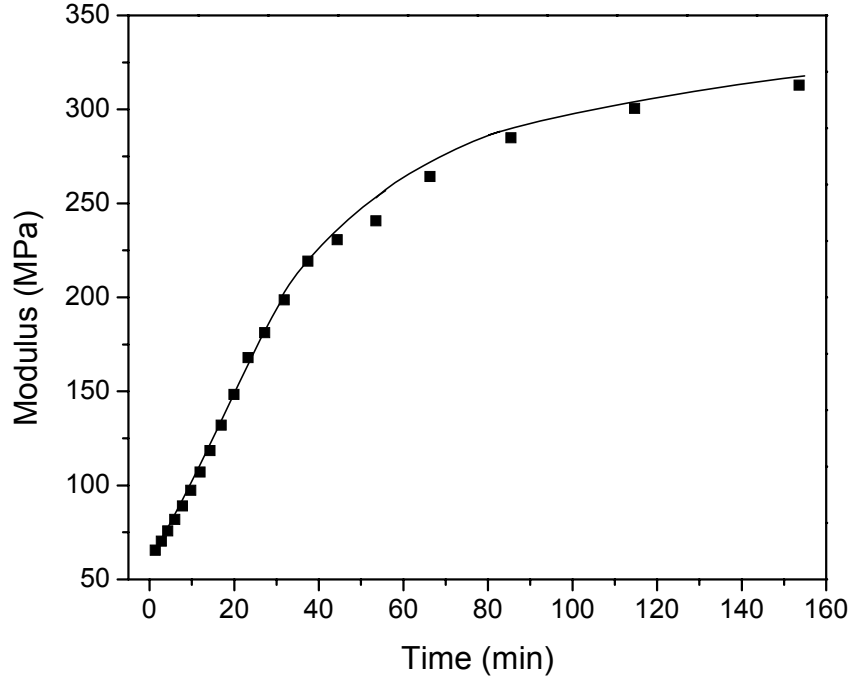(a) effective chemical shrinkage and (b) modulus

4.3 Validation

Two tests are conducted to verify the validity of the proposed method: a self-consistency test to confirm the accuracy of the raw data obtained from the two configurations, and a deformation measurement test to verify the validity of the evolution properties inversely calculated from the raw data.

4.3.1 Self-consistency test

A different configuration is tested for the self-consistency of the measurements using UF-1 and 2. The diameter of the polymer substrate is 1/8'' which corresponds to a

configuration of $\beta = 25$ (denoted as C-3). The BW shift of the specimen during the curing process is measured experimentally.

The experimental results of temperature profile and BW evolution of UF-1 are shown in Fig. 4.24. The corresponding $\Delta\lambda_B^d$ after the gelation point is plotted in Fig.4.25.
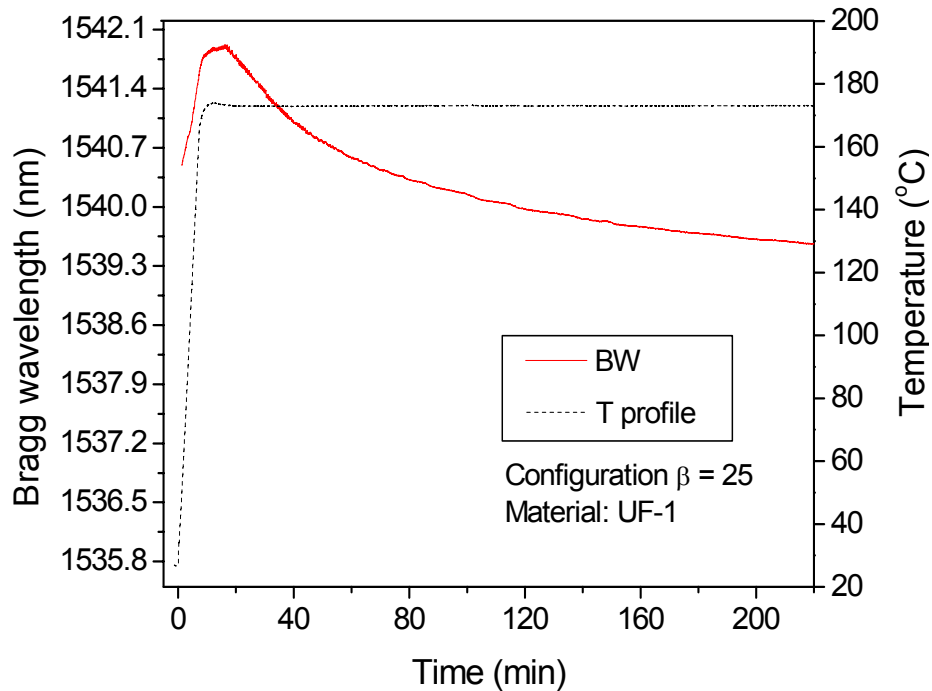
Fig. 4.24 BW and temperature profile of UF-1 with the configuration C-3

To predict the BW shift of the specimen with a configuration of C-3, an inverse of the procedure described in section 3.3.2 is used. In the procedure, the entire curing process is divided into the same small segments as those in section 3.3.2. In each segment, the chemical shrinkage increment and the instant equilibrium modulus are obtained from the property evolutions shown in Fig. 4.15. Using the governing equation (3-22), the BW shift increment can be calculated. Summation of the BW shift increment in each segment

yields the final BW shift evolution. The predicted results of UF-1 are also shown in Fig.4.25. The two results agree well with each other.
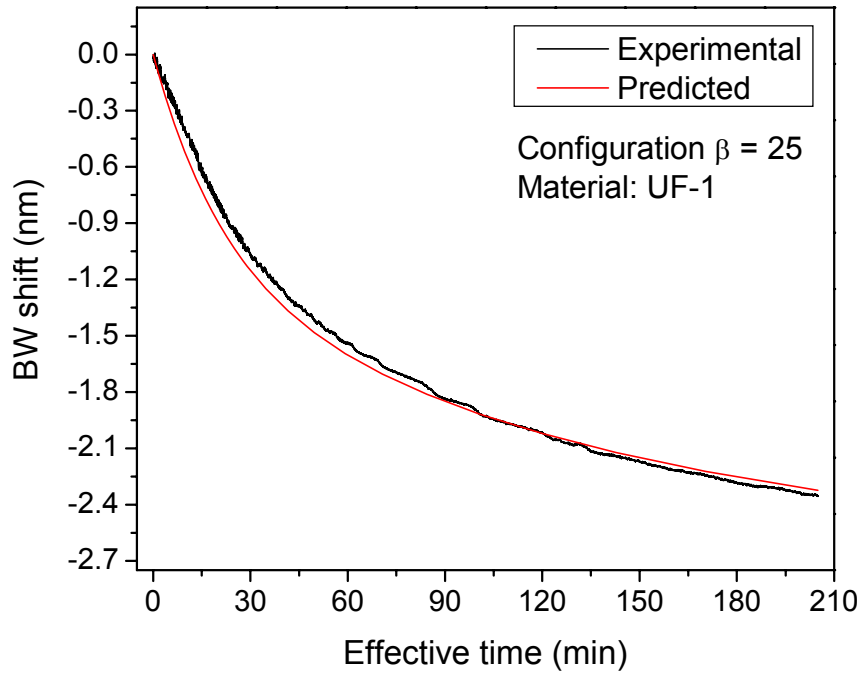
Fig. 4.25 Predicted and experimentally measured BW shift of UF-1

The same procedure was implemented for UF-2. The temperature profile and BW evolution of UF-2 are shown in Fig. 4.26. The corresponding $\Delta\lambda_B^d$ after the gelation point is plotted in Fig. 4.27, together with the predicted results using the data in Fig. 4.19. The two results are nearly identical.

The above results provide solid evidence that the experimental methodology is self-consistent and robust.
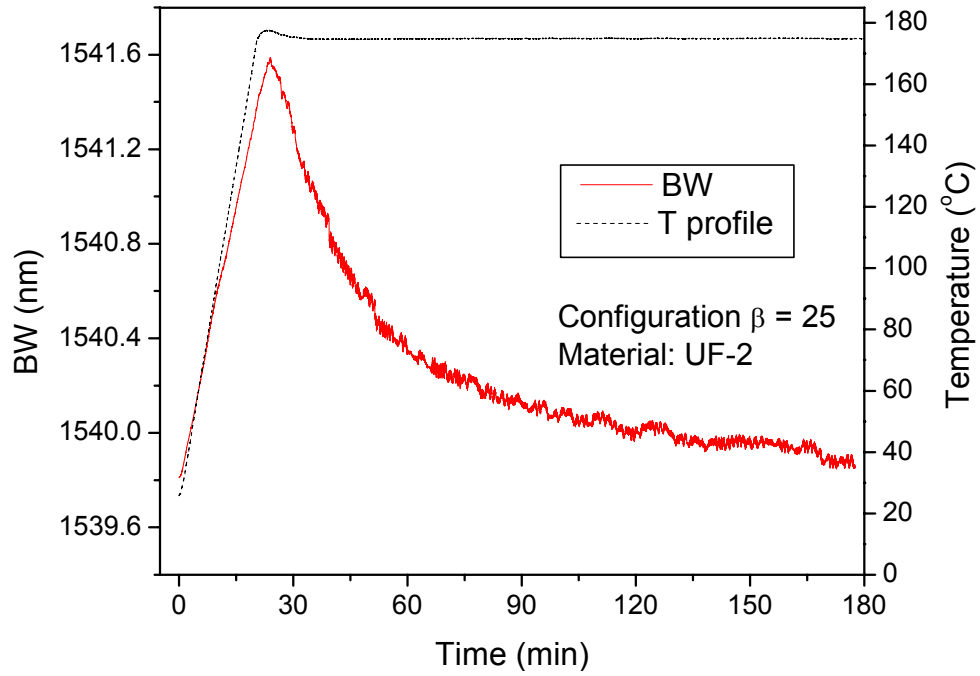
Fig. 4.26 BW and temperature profile of UF-2 with the configuration C-3
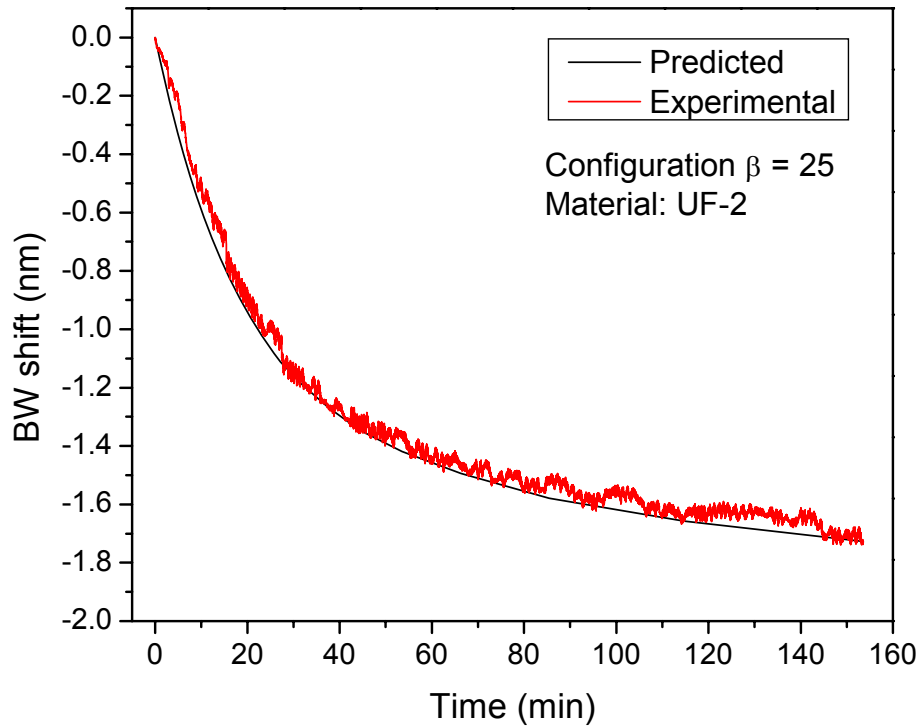
Fig. 4.27 Predicted and experimentally measured BW shift of UF-2

4.3.2 Warpage measurement by T/G Interferometry

The above verification procedure confirms the self-consistency of the experimental methodology. However, it does not necessarily guarantee that the measured evolution properties accurately represent the intrinsic properties of the polymer. The polymerization induced warpage of a bi-material strip was studied to further validate the accuracy of measured properties.

To fabricate a bi-material strip, high temperature tape was first wrapped around the edge of a rectangular glass strip to form a 'dam' as illustrated in Fig. 4.28. After that, the test polymer was poured into the 'dam' to form a bi-material strip. The curing-induced warpage of the bottom surface was measured by Twyman/Green (T/G) interferometry during the entire curing process.
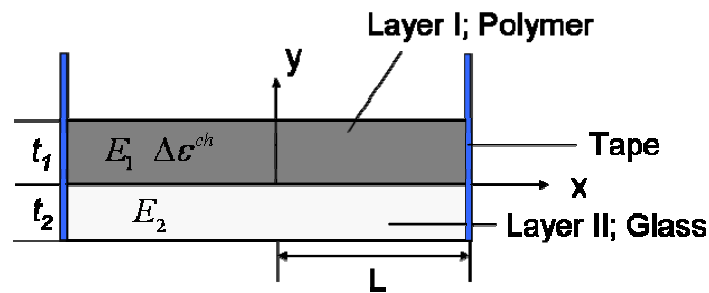
Fig. 4.28 Schematic drawing of bi-material joint

Twyman-Green (T/G) interferometry is a classical form of interferometry which involves the interference of coherent light. A coherent light source, usually a laser, is collimated and then passed through a beam splitter where it is split into *active* and *reference* paths as shown in Fig. 4.29. The reference and active paths are reflected by the reference flat and the specimen, respectively. The reflected beams combine to interfere

and create a fringe pattern seen by the observer, which represents the contour map of out-of-plane displacement (or warpage).
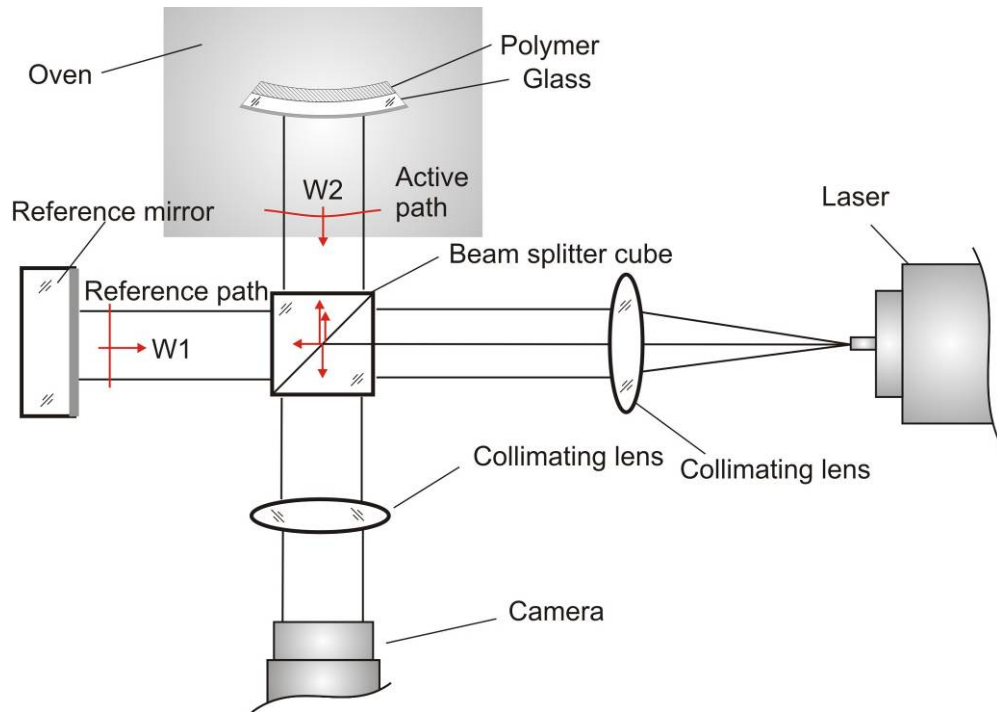
Fig. 4.29 Schematic drawing of the T/G setup

It is to be noted that the specimen was installed in an environmental chamber for real-time observations during curing at the high curing temperature. The specimen holder inside the environmental chamber was designed specifically to accommodate the uncured bi-material strip, which requires viewing from the bottom side. Figure 4.30 depicts the design that allows the required viewing direction. The specimen stage was designed to hold the uncured bi-material strip horizontally on top of a glass plate. Directly attached to the stage is a 45° mirror. This mirror reflects light both to and from the glass surface. A thin layer of aluminum was vacuum-deposited on the bottom surface

111

of the glass strip. To eliminate the undesired fringes formed by the interference of the
light reflected by the glass plate top surface and specimen surface, two approaches can be
used. In the first one, an index matching fluid can be used to fill the gap between the
bottom of the glass strip and the glass plate to avoid any undesired multiple reflections.
Alternatively, a cushion can be used to tilt the specimen angle so that the light reflected
by the glass plate top surface will not be collected by the camera.
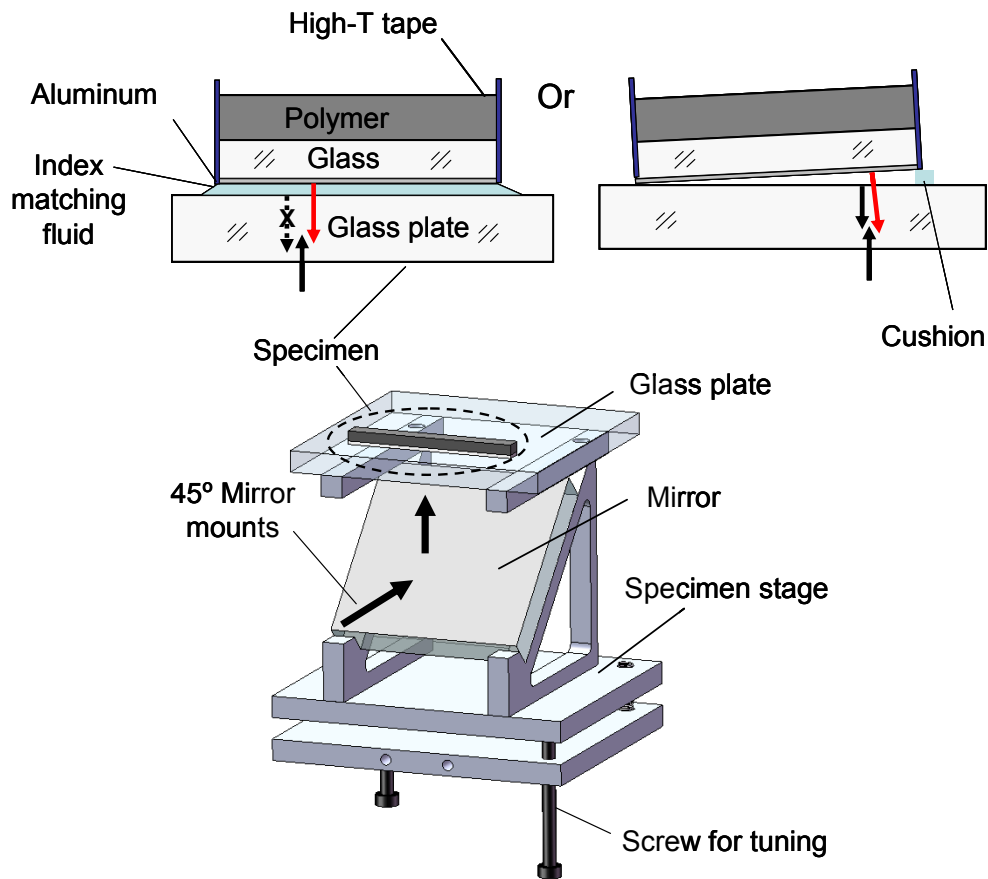
Fig. 4.30 Design of the specimen stage

With this configuration, the warpage of the bi-material, w, can be determined by
[130]

$$w = \frac{N}{2n} \lambda \qquad (4\text{-}8)$$

where $n = 1.5$ when the index matching fluid is used and $n = 1$ when the cushion method is used, N is the order of fringes, and λ is the wavelength of the laser.

The curing-induced warpage is also calculated numerically using the evolution properties. When a chemical shrinkage of $\Delta \varepsilon^{ch}$ occurs in the polymer layer that has a thickness of t_1 and an instant modulus of E_1, the curing induced warpage of the glass substrate can be calculated by (see Fig. 4.28)

$$\Delta w = \frac{3(t_1 + t_2)E_1 E_2 t_1 t_2 L^2}{E_1^2 t_1^4 + 6E_1 E_2 t_1^2 t_2^2 + E_2^2 t_2^4 + 4E_1 E_2 t_1^3 t_2 + 4E_1 E_2 t_1 t_2^3} \Delta \varepsilon^{ch} \qquad (4\text{-}9)$$

where t_2 and E_2 are the modulus and the thickness of the glass strip, respectively, and L is the half length of the strip . The derivation of Eqn. (4-9) can be found in Appendix B. Since both effective chemical shrinkage and modulus evolve nonlinearly with time, a numerical procedure similar to the one shown in section 4.3.1 is used to calculate the curing induced warpage evolution. The warpage change during each small time segment can be calculated first and the evolution of curing induced warpage can be then determined by accumulating the warpage increments.

A bi-material specimen consisting of the glass strip and UF-1 was tested at 175°C. The thickness of the glass strip and the polymer layer were 3.1 mm and 3.6 mm, respectively. An index matching fluid was used in the experiment. Figure 4.31 shows the representative fringe patterns of the half specimen, obtained at various times during the curing process.

time = 30 minutes

time = 90 minutes

time = 140 minutes
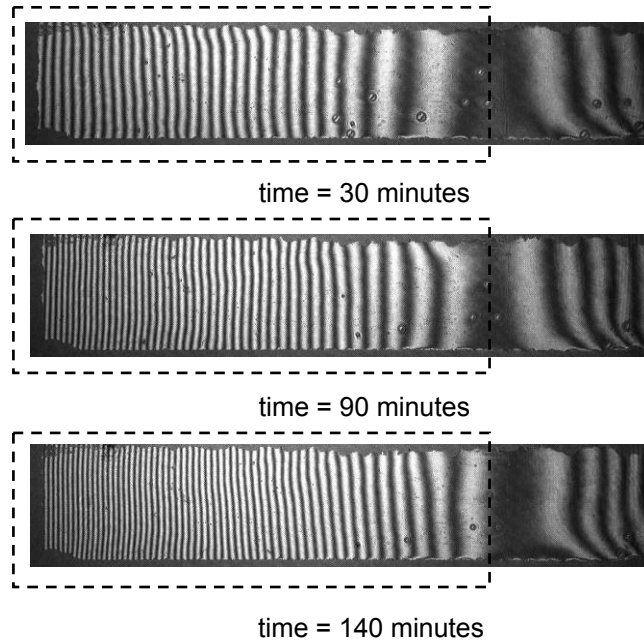
Fig. 4.31 Representative fringe patterns of the half specimen (UF-1) at different time

during the curing

An Argon laser with $\lambda = 514$ nm was employed in the experiment, which produced a contour interval of 171.3 nm per fringe. The warpage as a function of the effective time is shown in Fig. 4.32. The numerically predicted warpage evolution is also plotted in Fig.4.32 for a comparison. The two results agree very well, which confirms the validity of the property measurement.
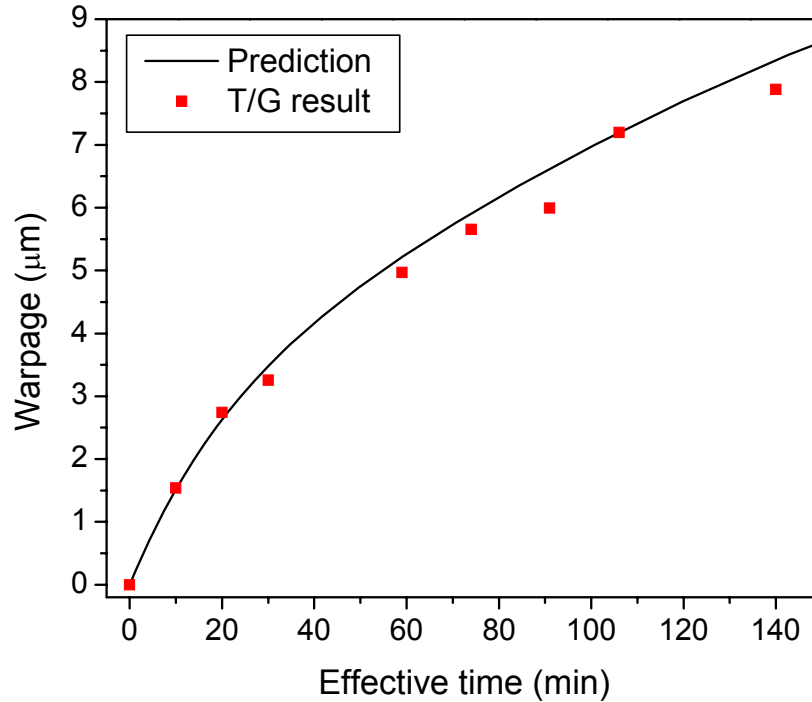
Fig. 4.32 Comparison between the experimentally measured warpage and predicted result of the material UF-1

Another bi-material specimen consisting of the glass strip and Epoxy-1 was repeated at 165 °C. The polymer layer was 2.5 mm in thickness and the glass strip was 1.9 mm. No index matching fluid was used in the experiment. The laser source had a wavelength of 488 nm and thus the contour interval was 244 nm per fringe. The fringe patterns of the whole specimen were captured at various times during the curing process and the results are shown in Fig. 4.33. The warpage is plotted as a function of the effective time in Fig. 4.34, together with the numerically predicted warpage evolution. The two results agree reasonably well, which confirms the validity of the property measurement.
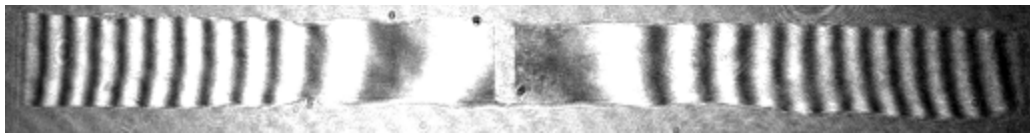
time = 0 (reach the target temperature)
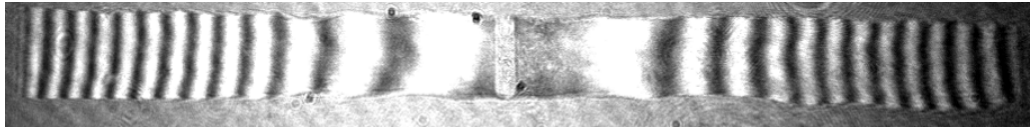
time = 48 minutes
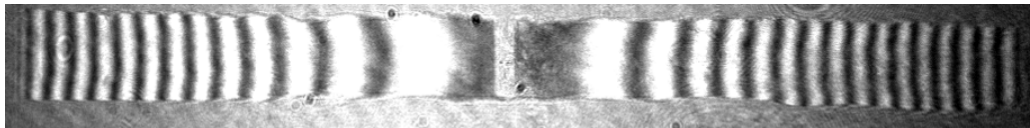
time = 88 minutes

time =128 minutes
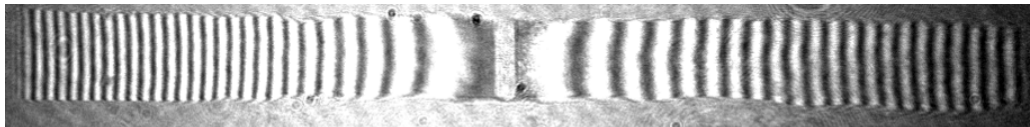
time =173 minutes

time =214 minutes
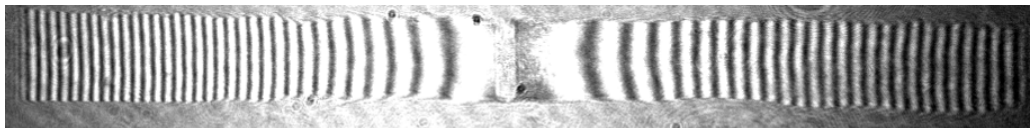
time =254 minutes

Fig. 4.33 Representative fringe patterns of the whole specimen (Epoxy-1) at different times during the curing process
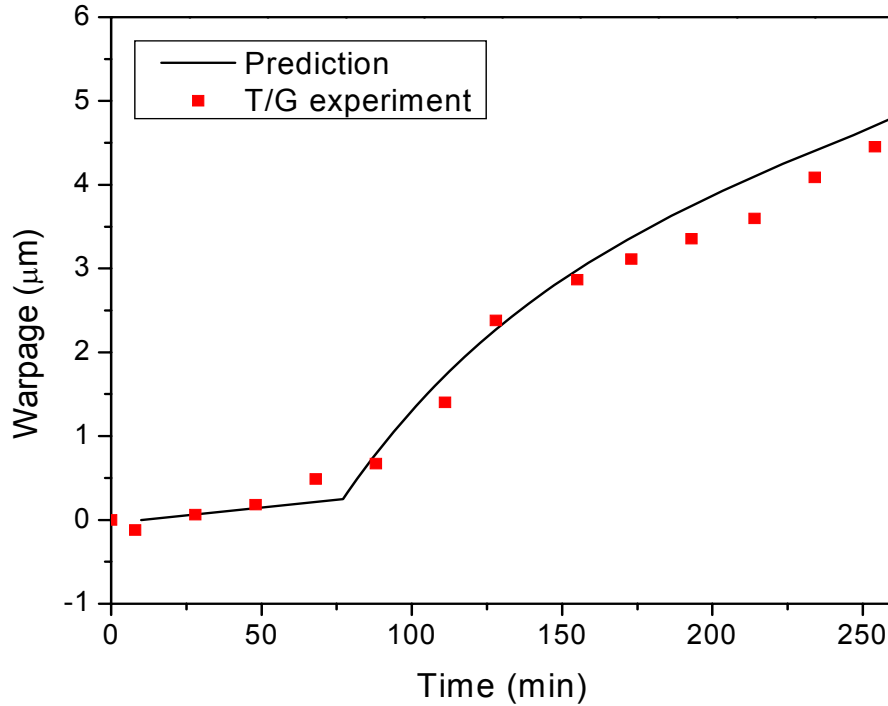
Fig. 4.34 Comparison between the experimentally measured warpage and predicted result of the material Epoxy-1

4.4 Extension: Total Chemical Shrinkage

In the above experimental procedure, the chemical shrinkage that occurs only after the gelation point is measured. For the mechanical stress analysis, the effective chemical shrinkage and associated with modulus evolution are sufficient. However, for curing optimization, other chemical properties are also desired. With the aid of theoretical modeling and/or an auxiliary experiment by a well-known method, DSC, the total chemical shrinkage can be determined from the measured effective chemical shrinkage evolution.

4.4.1 Closed form solution

If the curing kinetics of the polymer follows an nth order scheme, the follwing closed form solution can be obtained. The nth order model is expressed as

$$\frac{dp}{dt} = k_c (1-p)^n \tag{4-10}$$

Equation (4-10) can be solved with the initial condition of $p(0) = 0$ and the solution has the form of [95]

$$p = 1 - \left[1 - (1-n) \cdot k_c \cdot t \right]^{\frac{1}{1-n}} \tag{4-11}$$

The curing extent at the apparent gelation point, p_{gel}, can be determined as

$$p_{gel} = 1 - \left[1 - (1-n) \cdot k_c \cdot t_{gel} \right]^{\frac{1}{1-n}} \tag{4-12}$$

where t_{gel} is the apparent gelatin point. The curing extent that accumulates after the apparent gelation point is

$$\tilde{p}(\tilde{t}) = \left[1 - (1-n) \cdot k_c \cdot t_{gel} \right]^{\frac{1}{1-n}} - \left[1 - (1-n) \cdot k_c \cdot \left(t_{gel} + \tilde{t} \right) \right]^{\frac{1}{1-n}} \tag{4-13}$$

where $\tilde{t}$ is the effective time as defined in section 4.2.2.

It has been known that the chemical shrinkage is linearly proportional to the curing extent [4, 17, 112]. Mathematically, the effective chemical shrinkage can be written as

$$\varepsilon^{ch}(\tilde{t}) = \left\{ \left[1 - (1-n) \cdot k_c \cdot t_{gel} \right]^{\frac{1}{1-n}} - \left[1 - (1-n) \cdot k_c \cdot \left(t_{gel} + \tilde{t} \right) \right]^{\frac{1}{1-n}} \right\} \cdot \varepsilon^{ch}_{total} \tag{4-14}$$

where ε^{ch}_{total} is the total chemical shrinkage at the fully cured state. Using the nonlinear regression scheme, the measured evolution of effective chemical shrinkage can be fitted

by Eqn. (4-14). The total chemical shrinkage, ε_{total}^{ch}, and two kinetics parameters, k_c and n, can be then obtained.

Example: UF-2 and Epoxy-1

The evolution history of the effective chemical shrinkage of UF-2 (Fig. 4.19a) was fitted by Eqn. (4-14) and the result is shown in Fig. 4.35. The three unknowns are determined from the regression analysis: $\varepsilon_{total}^{ch} = 0.42\%$, $k_c = 0.082\,/\min$ and $n = 1.61$.
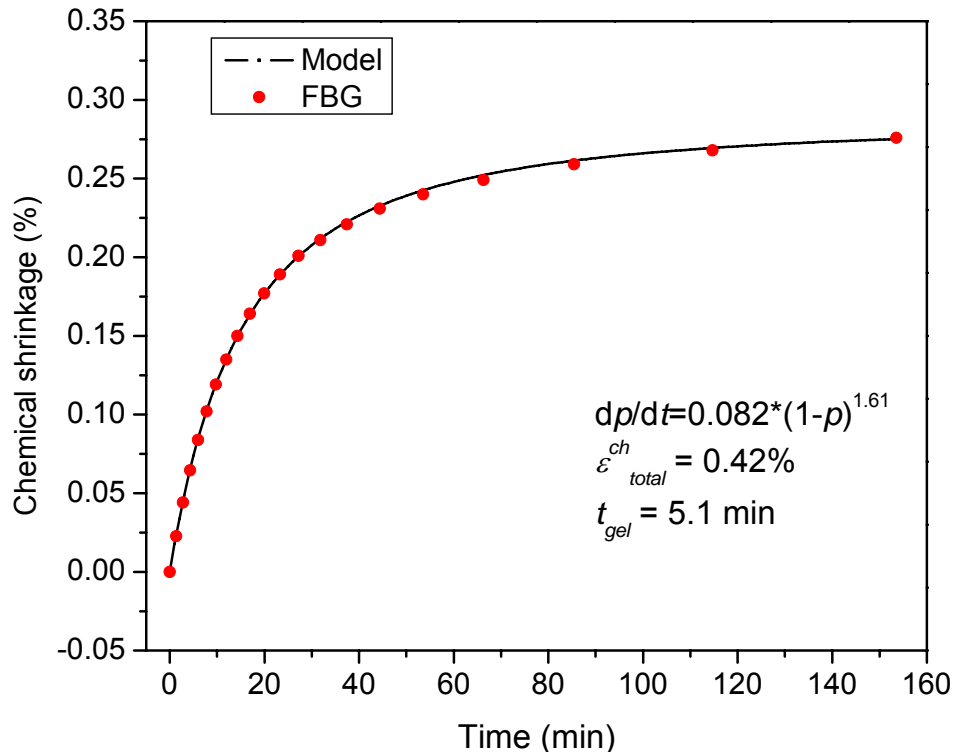
Fig. 4.35 Determination of total chemical shrinkage and curing kinetics of UF-2

Similarly, the evolution history of the effective chemical shrinkage of Epoxy-1 (Fig. 4.24a) was also fitted by Eqn. (4-14). The result is shown in Fig. 4.36. The regression analysis yields: $\varepsilon_{total}^{ch} = 2.7\%$, $k_c = 0.019\,/\min$ and $n = 0.98$.
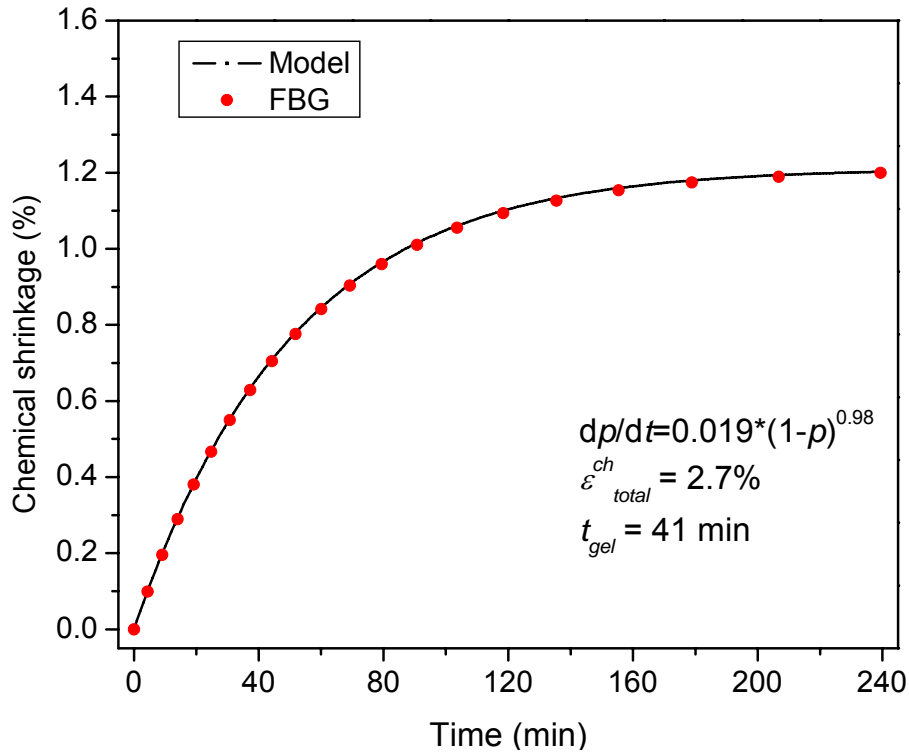
Fig. 4.36 Determination of total chemical shrinkage and curing kinetics of Epoxy-1

DSC validation for curing kinetics

The curing kinetics of UF-2 and Epoxy-1 were measured using a differential scanning calorimeter (DSC Pyris-1). The heat flow was documented in the isothermal mode. The temperature profile and recorded heat flow curve of material UF-2 are shown in Fig. 4.37a. The specimen was quickly ramped to 175 °C at a rate of 60 °C/min and dwelled for 2.5 hours. The total heat was then obtained by integrating the area under the heat flow curve and it was 21.8 J. The weight of the specimen was 0.0733 g and the total exotherm, ΔH was thus determined to be 330 J/g.

At arbitrary time t, the partial reaction heat was calculated by the partial integral of the area. The corresponding partial exotherm can be defined as $\Delta H(t)$. Then, the curing extent, $p(t)$, at time t can be simply determined as

120

$$p(t) = \frac{\Delta H(t)}{\Delta H} \qquad (4\text{-}15)$$

The evolution of curing extent was determined based on Eqn. (4-15) and the result is shown in Fig. 4.37b. The same n^{th}-order model was used to fit the measured curing extent, and the result is also shown in Fig. 4.37b. The curing kinetics are determined to be: $k_c = 0.080 \, / \min$ and $n = 1.57$. These values are nearly identical to those obtained from the FBG test data ($k_c = 0.082 \, / \min$ and $n = 1.61$).

The DSC results of Epoxy-1 are shown in Fig. 4.38a. The specimen was quickly ramped to 165 °C at a rate of 60 °C/min and dwelled for 4 hours. The total heat was calculated to be 26.0 J by the area integral. With the weight of the specimen known to be 0.0652 g, ΔH is determined to be 400 J/g. The determined curing extent evolution is shown in Fig. 4.38b. After fitting with an nth order model, the curing kinetics are determined to be: $k_c = 0.018 \, / \min$ and $n = 0.97$. The result agrees very well with the result obtained from the FBG test data which is $k_c = 0.019 \, / \min$ and $n = 0.98$.

(a)

$$dp/dt = 0.080*(1-p)^{1.57}$$
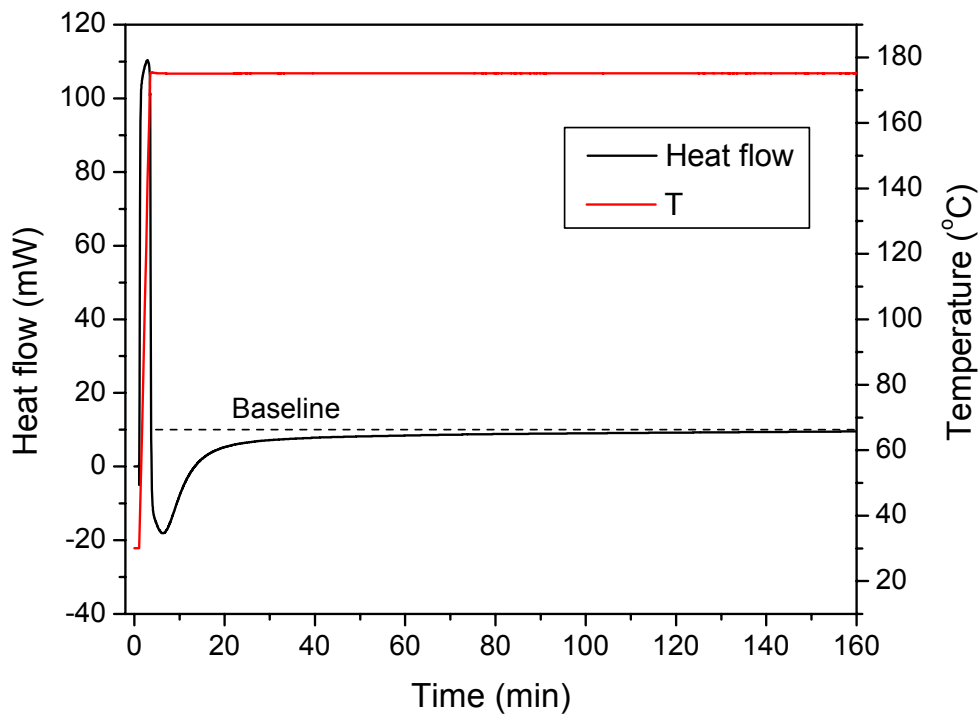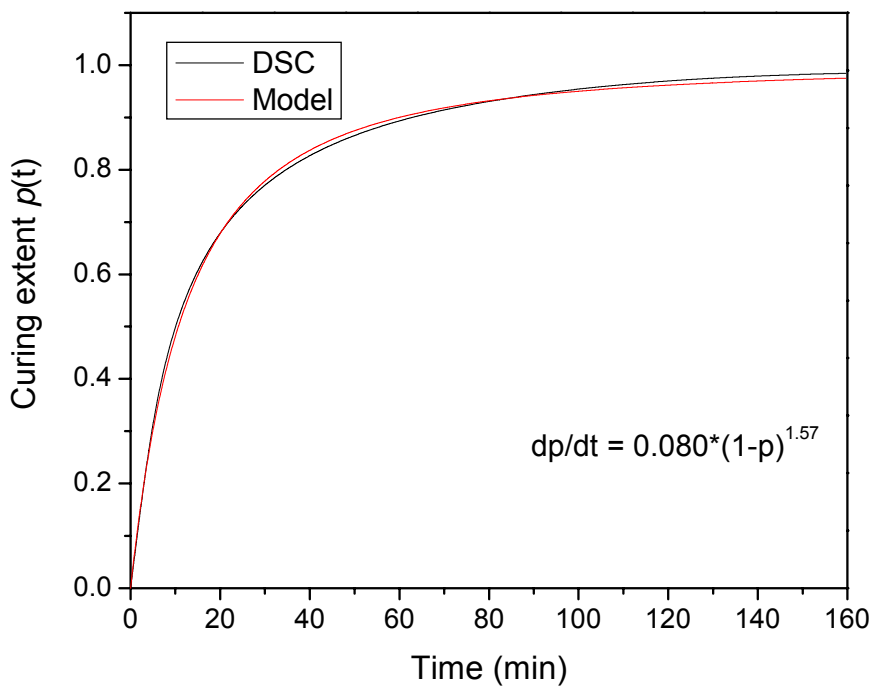
(b)

Fig. 4.37 (a) DSC results of the material UF-2; (b) Evolution of curing extent and determination of curing kinetics of UF-2

(a)

$$dp/dt = 0.018*(1-p)^{0.97}$$
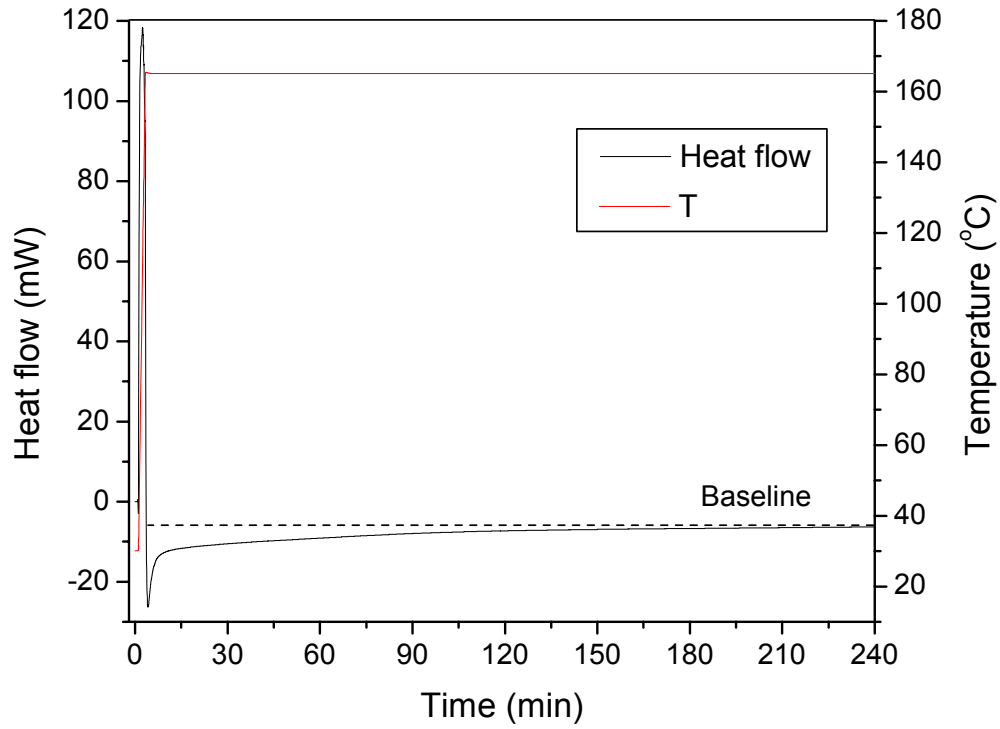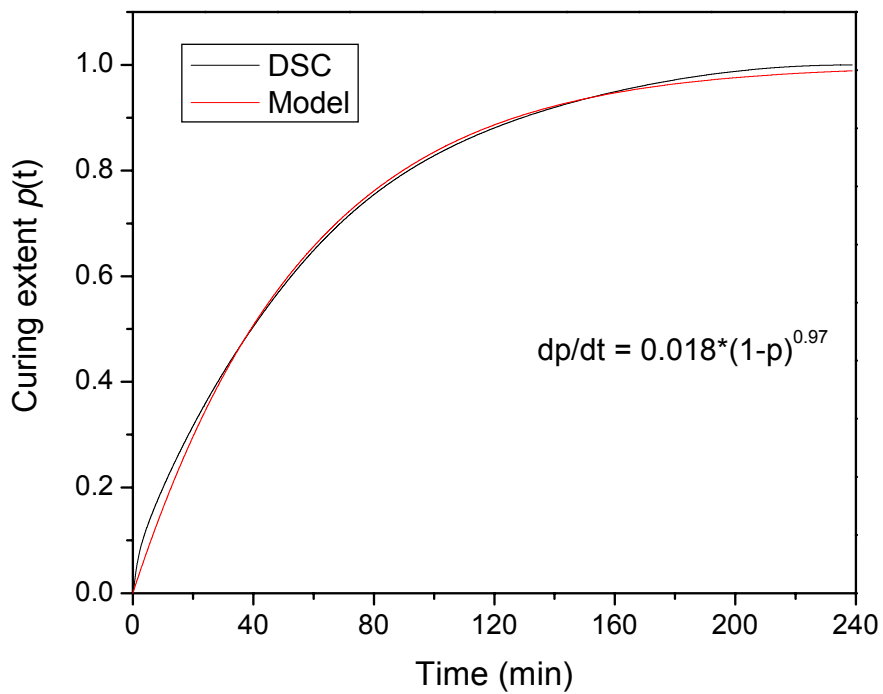
(b)

Fig. 4.38 (a) DSC results of the material Epoxy-1; (b) Evolution of curing extent and determination of curing kinetics of Epoxy-1

4.4.2 Combined approach with DSC

When the curing kinetics of the polymer does not follow the nth order model, the total chemical shrinkage can be estimated by combining the measured effective chemical shrinkage data and DSC data. The DSC results of UF-1 are shown in Fig. 4.39, and it is found that the curing extent cannot be fitted well by the nth order model.

From Fig. 4.39, the curing extent at the apparent gelation time, 5.5min, can be read directly and it is determined to be 0.37. Then the total chemical shrinkage is estimated to be 0.36% / (1-0.37) = 0.57%.
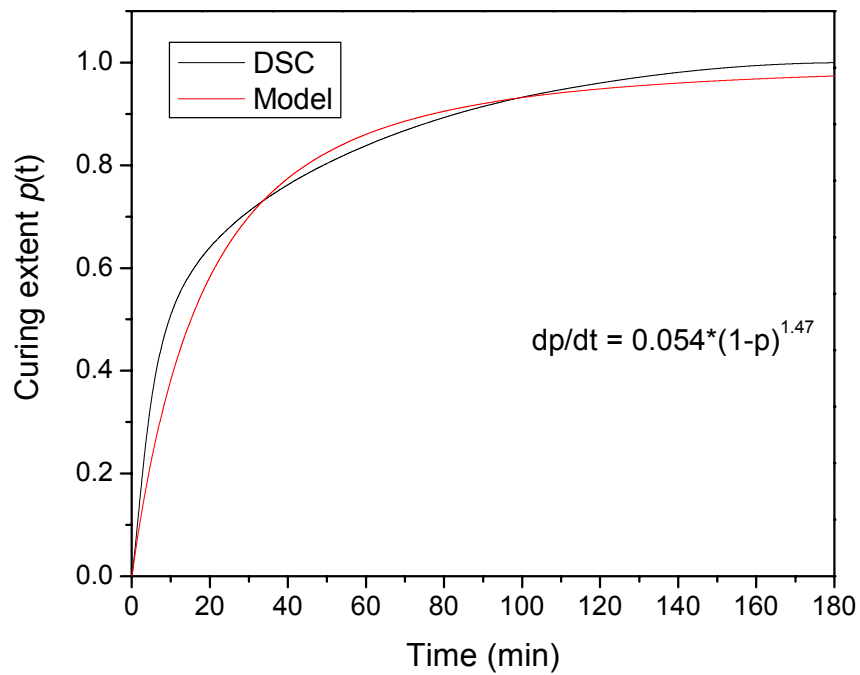
(b)

Fig. 4.39 Curing kinetics of UF-1 measured by DSC

4.5 Prediction of Property Evolutions at Arbitrary Temperatures

The above experimental procedure provides a means of measuring the property evolutions at a specific curing temperature. A modeling approach is proposed to estimate the property evolutions at other curing temperatures.

4.5.1 Theoretical basis

A general model for the curing kinetics of polymers can be written as [91, 99, 103, 107, 131]

$$\frac{dp}{dt} = k(T)f(p) \tag{4-16}$$

where p is the curing extent, t is the time, $k(T)$ is the rate constant that depends on the temperature and $f(p)$ is the conversion-dependent function. The rate constant is related to the temperature through an Arrhenius relationship and can be expressed as

$$k(T) = Ae^{-\frac{E_a}{RT}} \tag{4-17}$$

where A is a material constant, E_a is the activation energy and R is the ideal gas constant ($8.314 \ J/mol \cdot K$). It is important to noted that the function $f(p)$ can take any mathematical form of p. Substituting Eqn. (4-17) into Eqn. (4-16) and integrating on both sides yields

$$\int_0^p \frac{dp}{f(p)} = \int_0^t Ae^{-\frac{E_a}{RT}}dt \tag{4-18}$$

Consider a case where the polymer is isothermally cured at two different temperatures T_1 and T_2. From Eqn. (4-18),

$$\int_0^{p_0} \frac{dp}{f(p)} = Ae^{-\frac{E_a}{RT_1}}t_1 = Ae^{-\frac{E_a}{RT_2}}t_2 \qquad (4\text{-}19)$$

where t_1 and t_2 are the time to reach a curing extent of p_0 under the corresponding curing temperatures T_1 and T_2, respectively. Equation (4-19) can be rewritten as

$$t_2 = e^{-\frac{E_a}{R}\left(\frac{1}{T_1} - \frac{1}{T_2}\right)}t_1 \qquad (4\text{-}20)$$

Equation (4-20) relates the time to reach a same curing extent of p_0 when the polymer is cured at different temperatures.

The relation between the effective chemical shrinkage and the curing extent can be modeled as

$$\varepsilon^{ch}(t) = \varepsilon_\infty^{ch} \cdot G(p) \qquad (4\text{-}21)$$

where ε_∞^{ch} is the effective chemical shrinkage after the complete curing. The function $G(p)$, can take any mathematical form of p (e.g. a linear function [4, 17, 112]). The polymer has a same curing extent of p_0 at time t_1 when cured at T_1 and time t_2 when cured at T_2; mathematically

$$\frac{\varepsilon_{T_1}^{ch}(t_1)}{\varepsilon_{T_2}^{ch}(t_2)} = 1 \qquad (4\text{-}22)$$

where $\varepsilon_{T_1}^{ch}$ and $\varepsilon_{T_2}^{ch}$ are the effective chemical shrinkage when cured at T_1 and T_2, respectively.

The relation between the modulus and the curing extent can be modeled as

$$E(t) = E_\infty^0(T) \cdot H(p) \qquad (4\text{-}23)$$

where E_∞^0 is a temperature-dependent equilibrium modulus when the polymer is fully cured. The function, $H(p)$, can also take any mathematical form of p (e.g., percolation theory). From Eqn. (4-23),

$$\frac{E_{T_2}(t_2)}{E_{T_1}(t_1)} = \frac{E_\infty^0(T_2)}{E_\infty^0(T_1)} \tag{4-24}$$

where E_{T_1} and E_{T_2} are the modulus when cured at T_1 and T_2, respectively.

4.5.2 Implementation

The above approach was implemented with the material UF-2. Using DSC, the curing kinetics of UF-2 was measured at three temperatures: 195 °C, 185 °C and 175 °C. The results are shown in Fig. 4.40.
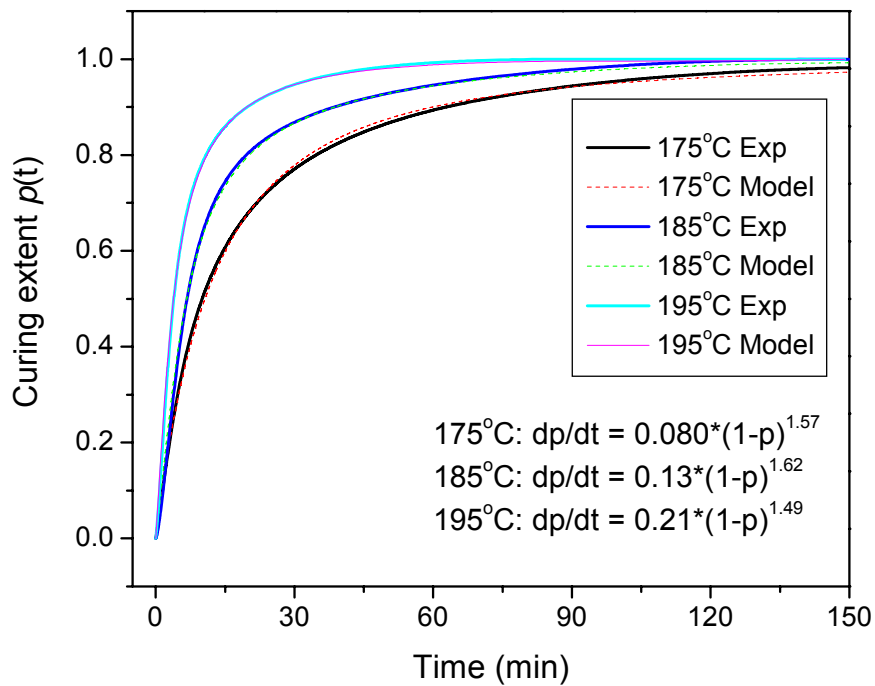
Fig. 4.40 DSC results of UF-2 at 195 °C, 185 °C and 175 °C

127

The curing rates change significantly at different curing temperatures. An nth order modeling was used to fit the curing kinetics. The result is also shown in Fig. 4.40. The rate constant, k, increases by several times when the temperature increases from 175 °C to 195 °C. On the other hand, the reaction order, n, remains virtually the same within the temperature range and it is assumed to be independent of the temperature. The rate constant versus $1/T$ is plotted in Fig. 4.41. The activation energy, E_a, is obtained through the linear fitting of the data point; it is 89 kJ/mol.
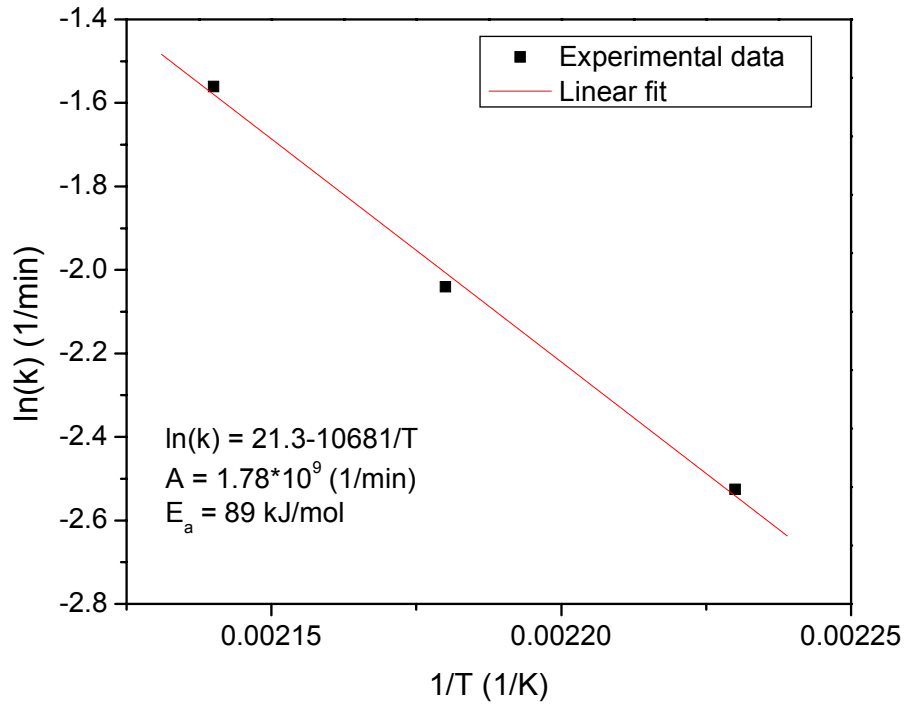
Fig. 4.41 Determination of activation energy of UF-2

The property evolutions of UF-2 measured at 175 °C (plotted in Fig. 4.19) was used as the data at the reference temperature T_{ref}. From Eqn. (4-20),

$$\ln(t) = \frac{E_a}{R}\left(\frac{1}{T} - \frac{1}{T_{ref}}\right) + \ln(t_{ref}) = \ln\left(S(T)\right) + \ln(t_{ref}) \qquad (4\text{-}25)$$

where $S(T)$ is the shift factor which is defined as

$$\ln\left(S(T)\right) \equiv \frac{E_a}{R}\left(\frac{1}{T} - \frac{1}{T_{ref}}\right) \qquad (4\text{-}26)$$

Equation (4-25) shows that, for any other curing temperature of T, the modulus and effective chemical shrinkage evolutions can be obtained by shifting the reference data by the shift factor along the log time axis; to the left (when $T > T_{ref}$) or to the right (when $T < T_{ref}$). The shift factor of UF-2 was calculated for different temperatures and is plotted in Fig. 4.42.
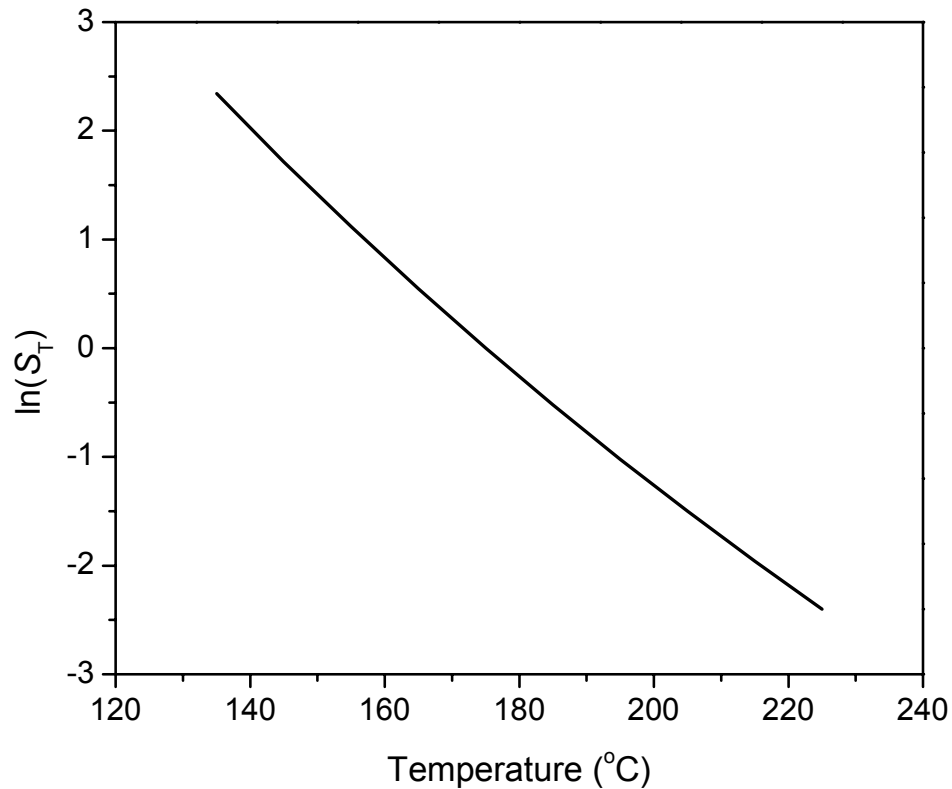
Fig. 4.42 Shift factor of UF-2 at various temperatures

The shift factors for 165 °C and 185 °C are 0.55 and -0.52, respectively. The effective chemical shrinkage at the two temperatures can be obtained by shifting the reference data at 175 °C, as shown in Fig. 4.43.
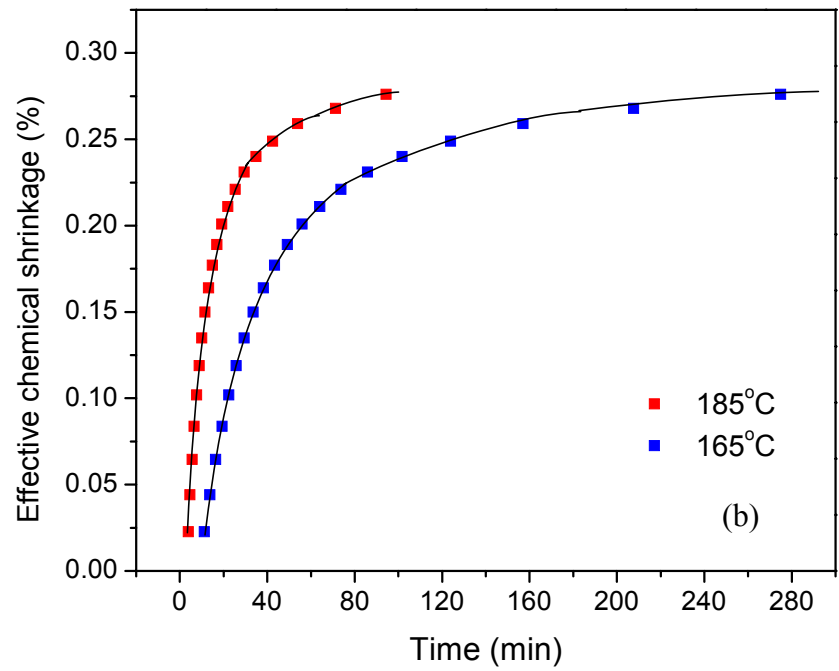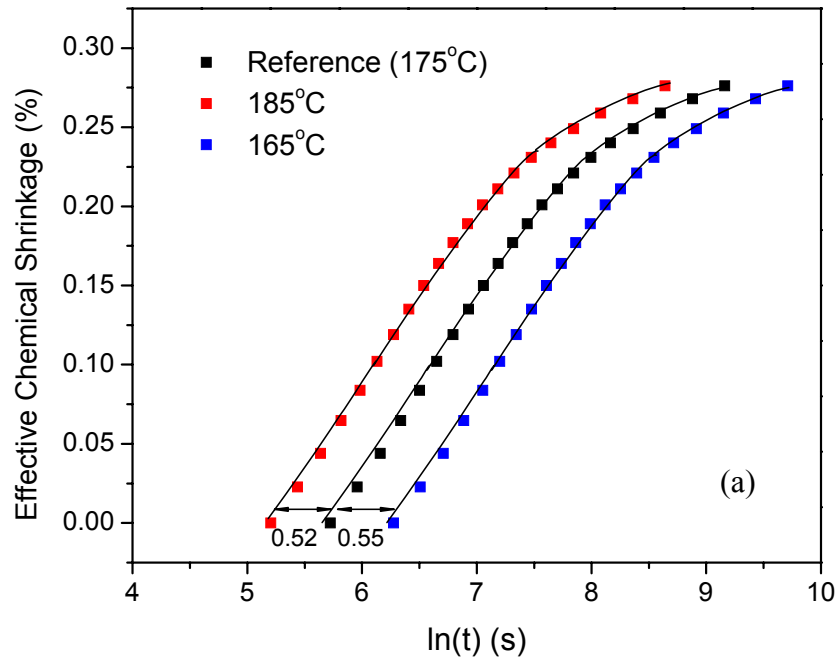
Fig. 4.43 Effective chemical shrinkage evolutions at 185 °C and 165 °C at (a) log time

scale and (b) regular time scale

The final equilibrium modulus was measured to be 0.26 GPa at 185 °C and 0.28 GPa at 165 °C followed the method introduced in Section 3.5. Using the same shift factors and Eqn. 4-24, the modulus evolutions of UF-2 at temperatures 185 °C and 165°C can be obtained. The result is shown in Fig. 4.44.
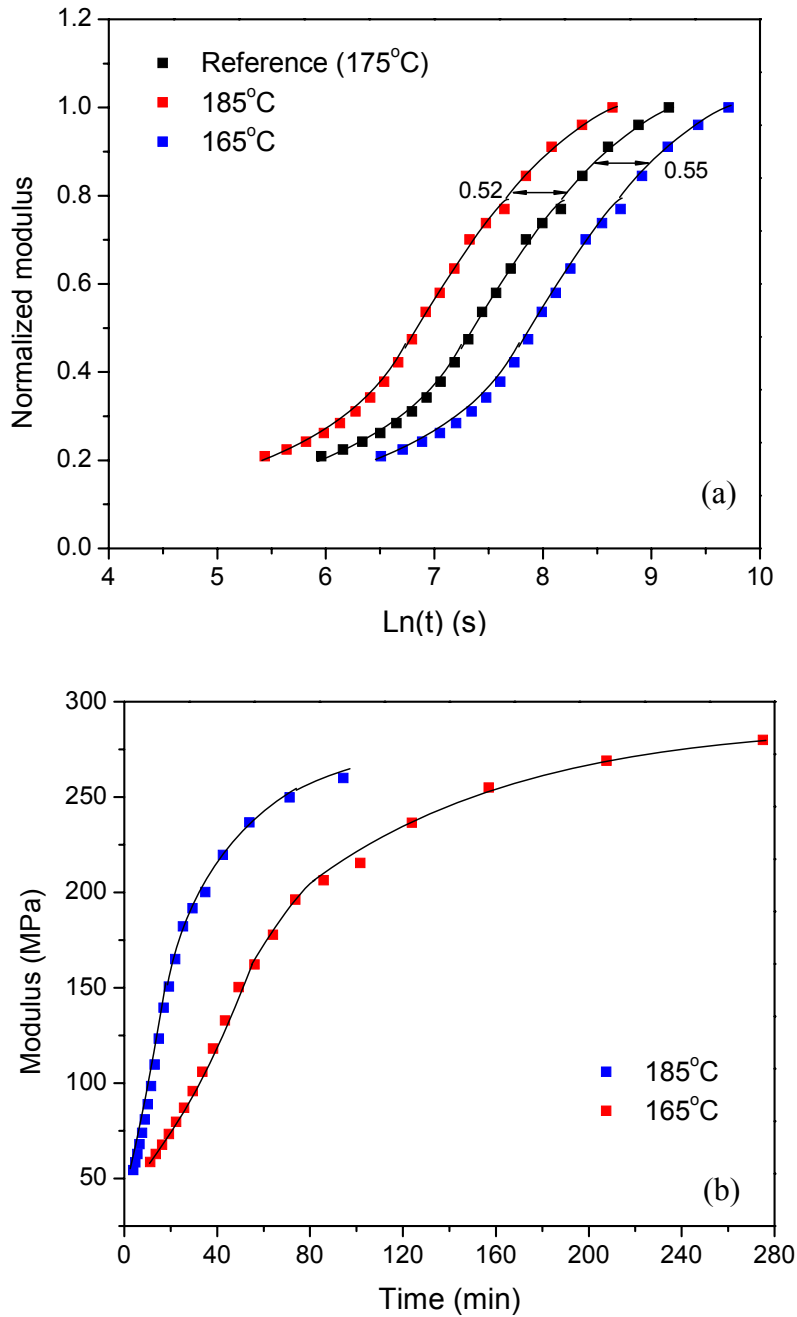
Fig. 4.44 Predicted modulus evolutions at 185 °C and 165 °C at (a) log time scale and (b) regular time scale

The concept of the shift factor is similar to the shift function widely used in the formation of the master curve in visco-elasticity. It is proved to be a powerful tool in the property evolution predictions.

Chapter 5 Measurement of Properties after Curing

5.1 Determination of CTE and T_g

5.1.1 Experimental results and data analysis

After the polymer was cured and the evolutions of effective chemical shrinkage and modulus were measured, the cured specimens of configuration C-1 and C-2 were taken out of the silicone rubber tubing and simultaneously subjected to a temperature excursion. The BW was continuously documented during the temperature ramping. The CTE of the polymer was then evaluated using the method introduced previously in section 3.4.

Figure 5.1 shows the temperature profiles of C-1 and C-2 of UF-1 recorded during the temperature ramping. To ensure the synchronization and uniformity of the specimen temperature, a slow ramp rate of 1.5 °C/min was used.
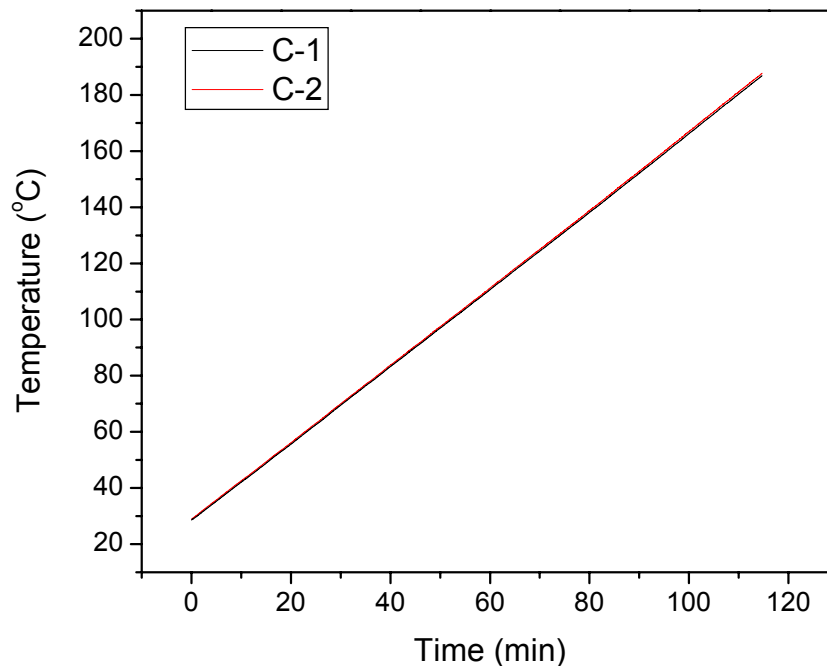
Fig. 5.1 Temperature profile of the two specimens of material UF-1

From the figure, it can be seen that the temperature of the two specimens increases with time at the same speed. The total BW and the deformation induced BW shifts of the two configurations during the ramping are shown in Fig. 5.2 and Fig. 5.3, respectively.

Fig. 5.2 Total BW of the two specimens of material UF-1 during the ramping
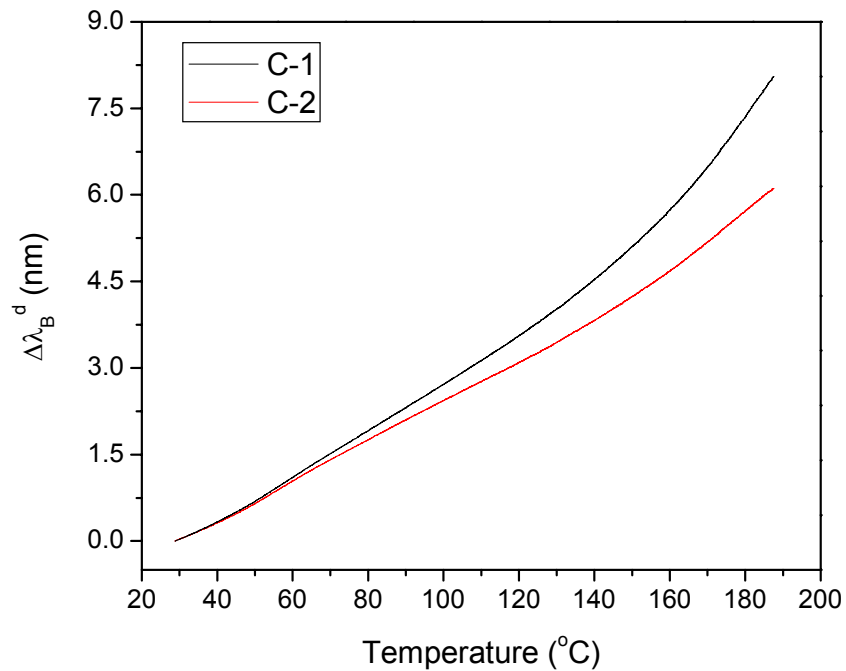
Fig. 5.3 Deformation induced BW of material UF-1 during the ramping

134

Due to the large modulus of the material at low temperature, the BW shifts of the two configurations exhibit the same slope at the initial stage of the temperature ramping. As the modulus gradually decreases, the measured BW shift of configuration C-1 starts to deviate from that of configuration C-2. The slope of BW increase is larger in configuration C-1 because of the larger volume stiffness.

Based on Eqns. (3-30) and (3-31), the deformation induced BW shift of configuration C-inf was calculated and the result is shown in Fig. 5.4.
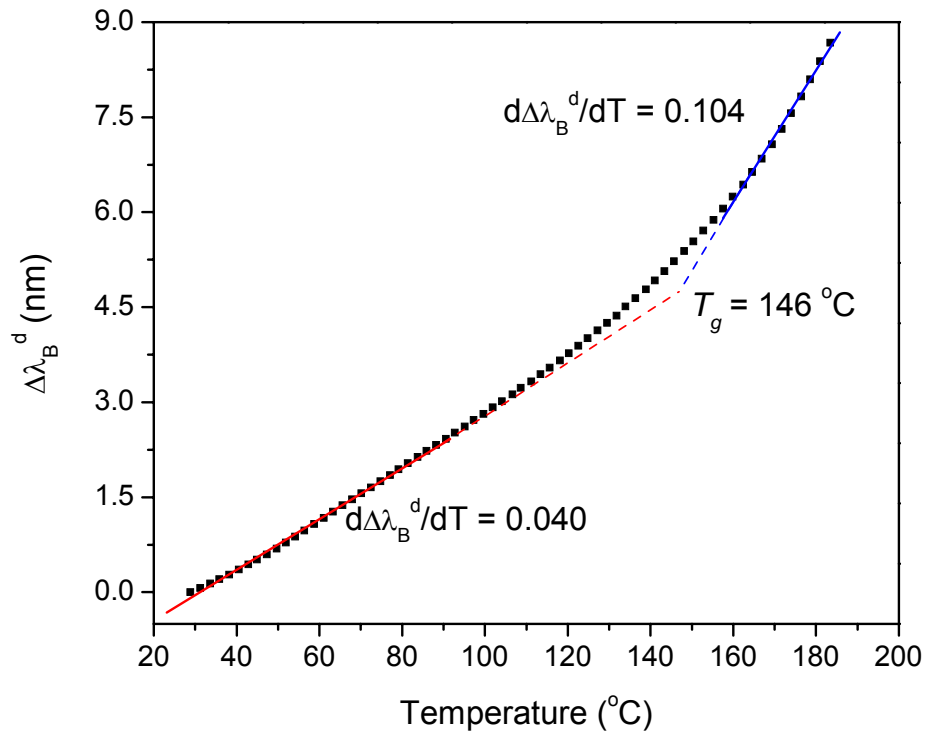
Fig. 5.4 BW of material UF-1 of configuration C-inf and determination of CTE and T_g

A transitional area can be clearly identified in the curve. The slope before the transition was fitted to be 0.040 nm/°C and the slope after the transition was fitted to be 0.104 nm/°C. According to Eqn. (3-28), the CTE was determined to be

135

$$\alpha_1 = \frac{0.040}{1540 \cdot (1 - 0.216)} + 0.55 \cdot 10^{-6} = 33.7 \cdot 10^{-6} / {}^{\circ}C$$

$$\alpha_2 = \frac{0.104}{1540 \cdot (1 - 0.216)} + 0.55 \cdot 10^{-6} = 86.7 \cdot 10^{-6} / {}^{\circ}C$$

The glass transition temperature was located at the inflection point of the BW shift curve and was determined to be 146 °C.

The same procedure was repeated for UF-2. Figure 5.5 shows the temperature profile of the two specimens of UF-2 recorded during the temperature ramping.
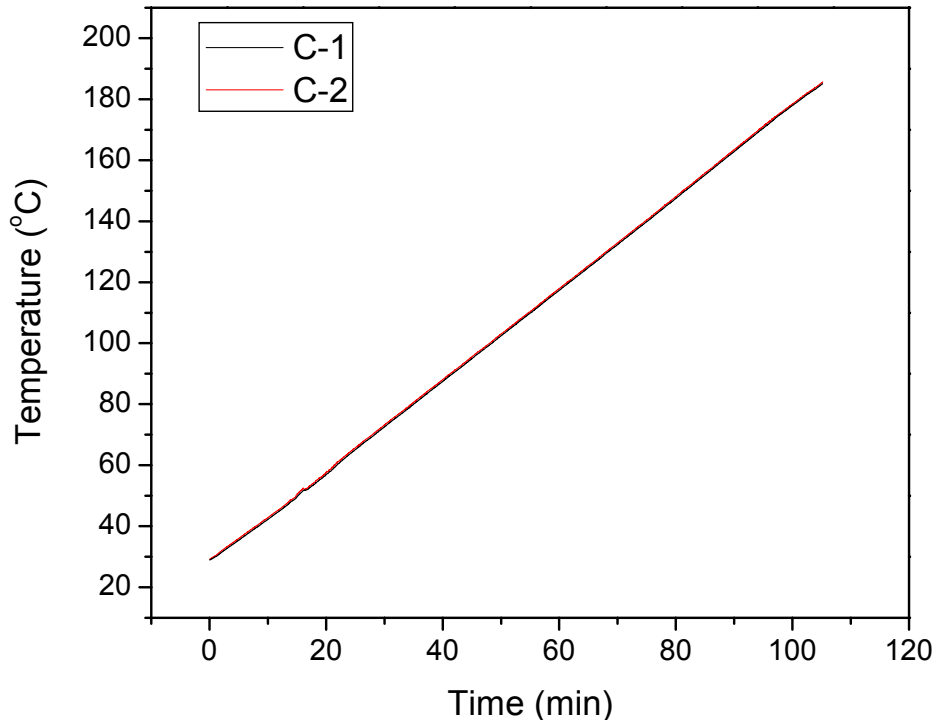
Fig. 5.5 Temperature profile of the two specimens of UF-2

The total BW of the specimens during the ramping was documented and the results are shown in Fig. 5.6. After subtraction of the intrinsic BW shift, the deformation induced BW shift was calculated and the result is shown in Fig. 5.7. It can be seen that the

measured BW shift of configuration C-1 overlaps with that of C-2 within a wide range at low temperature.
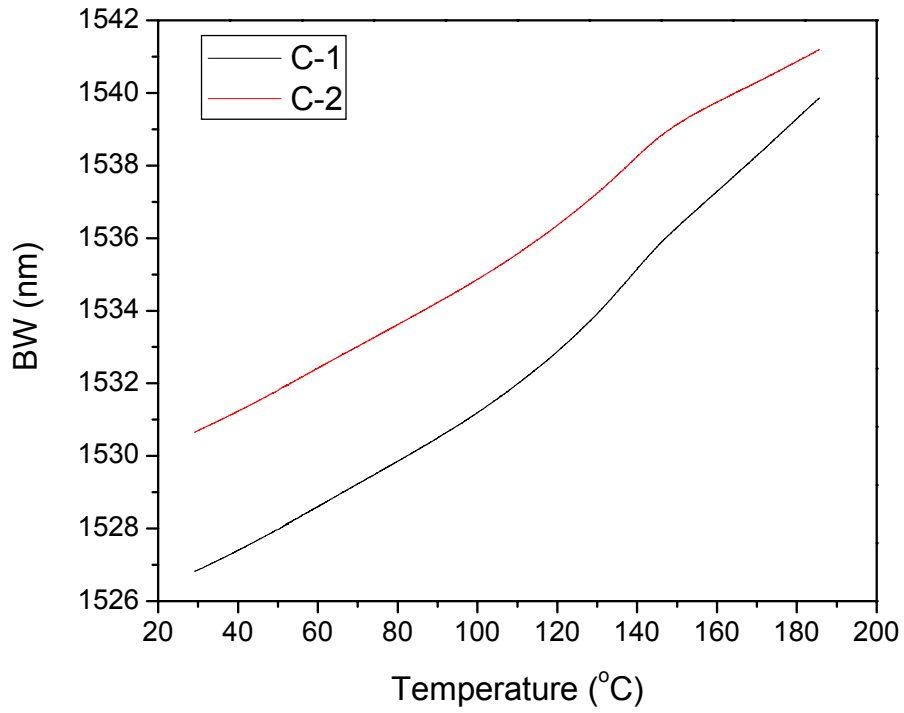
Fig. 5.6 Total BW of the two specimens of material UF-2 during the ramping
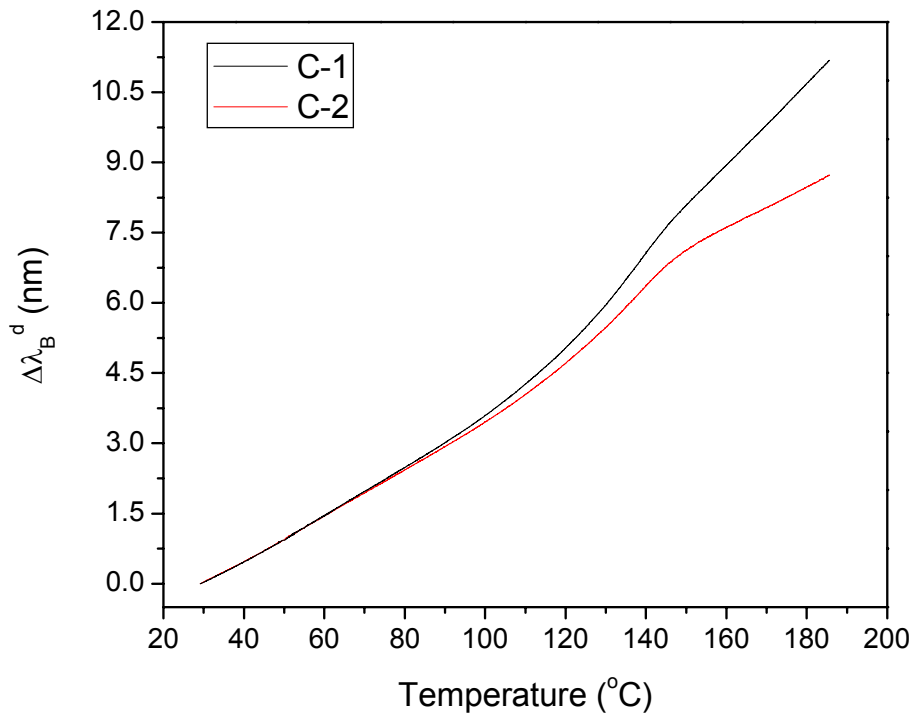
Fig. 5.7 Deformation induced BW of material UF-2 during the ramping

Based on Eqns. (3-30) and (3-31), the deformation induced BW shift of configuration C-inf was calculated and the result is shown in Fig. 5.8. The slope before the transition was fitted to be 0.0512 nm/°C and the slope after the transition was fitted to be 0.128 nm/°C. According to Eqn. (3-28), the CTE was determined to be

$$\alpha_1 = \frac{0.0512}{1540 \cdot (1 - 0.216)} + 0.55 \cdot 10^{-6} = 42.5 \cdot 10^{-6} / °C$$

$$\alpha_2 = \frac{0.128}{1540 \cdot (1 - 0.216)} + 0.55 \cdot 10^{-6} = 106 \cdot 10^{-6} / °C$$

The glass transition temperature was located at the inflection point of the BW shift curve and was determined to be 120 °C.
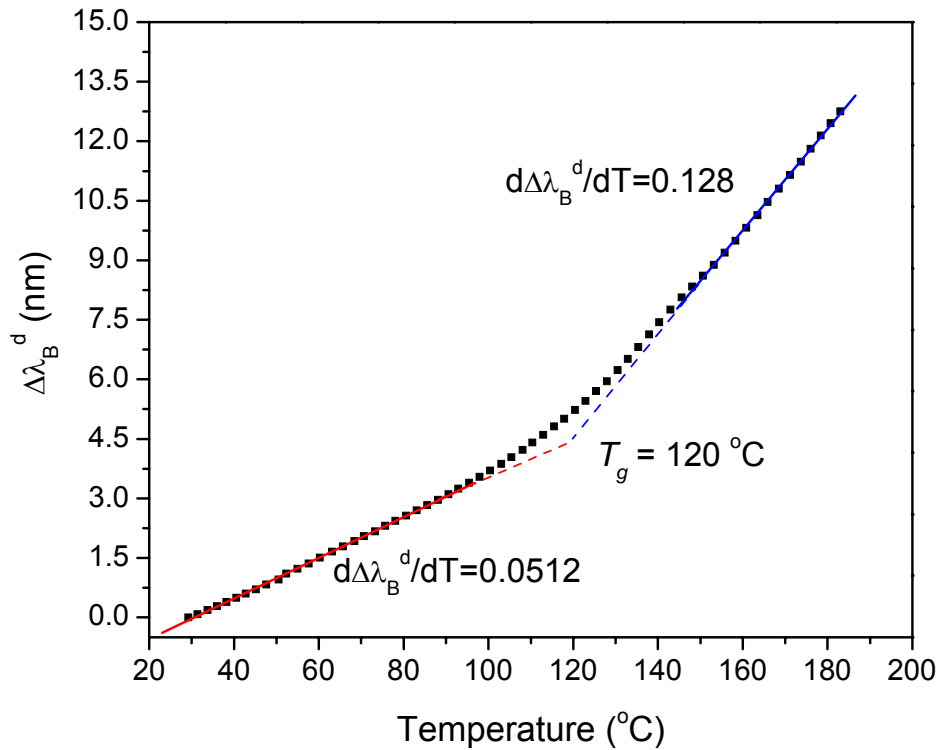
Fig. 5.8 BW of UF-2 of configuration C-inf and determination of CTE and T_g

The CTE and T_g of the material Epoxy-1 was also measured. Figure 5.9 shows the temperature profile of the two specimens recorded during the temperature ramping.
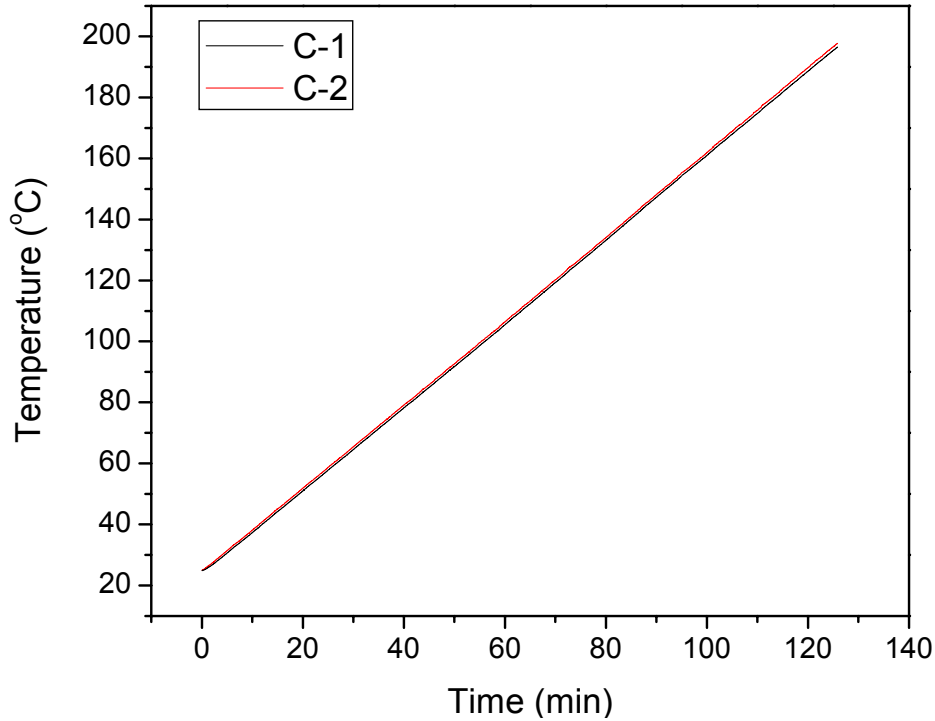
Fig. 5.9 Temperature profile of the two specimens of material Epoxy-1

The result of the measured total BW is shown in Fig. 5.10. The deformation induced BW shift was calculated and the result is shown in Fig. 5.11. At low temperature, the measured BW shift of configuration C-1 overlaps with that of C-2 within a wide range. According to Eqns. (3-30) and (3-31), the deformation induced BW shift of configuration C-inf was calculated and the result is shown in Fig. 5.12. Two different slopes are identified in the curve: 0.0632 nm/°C and 0.0985 nm/°C. Using Eqn. (3-28), the CTE was determined as

$$\alpha_1 = \frac{0.0632}{1540 \cdot (1-0.216)} + 0.55 \cdot 10^{-6} = 52.9 \cdot 10^{-6} /^{\circ} C$$

$$\alpha_2 = \frac{0.0985}{1540 \cdot (1 - 0.216)} + 0.55 \cdot 10^{-6} = 82.1 \cdot 10^{-6} /^{\circ}C$$

The glass transition temperature was determined to be 130 °C.
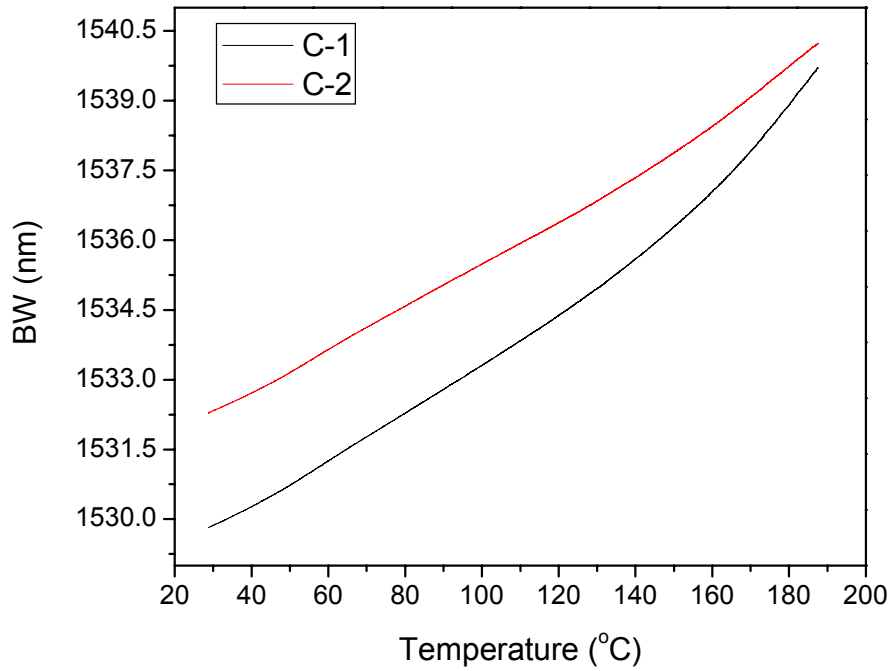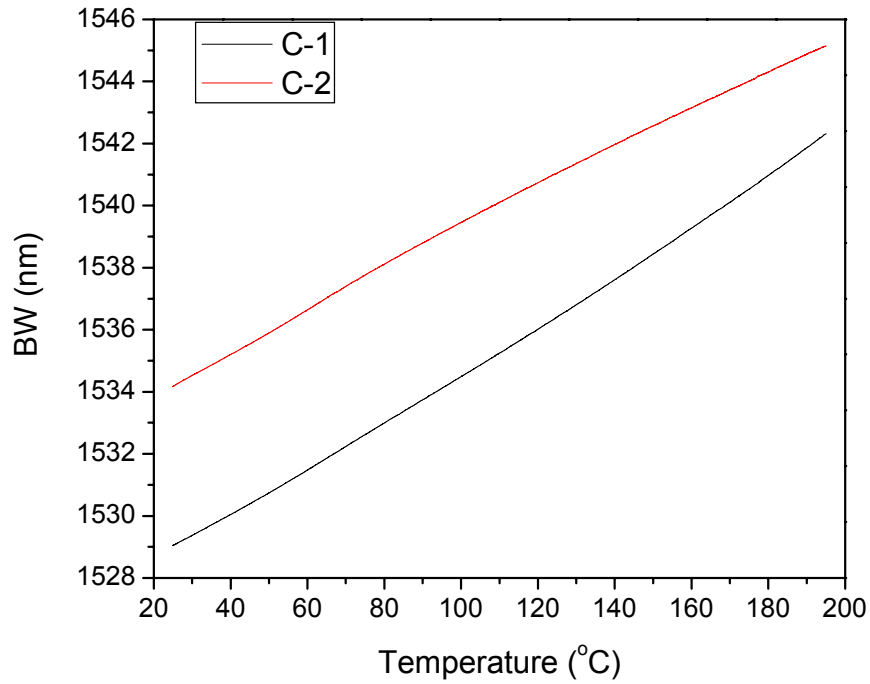

Fig. 5.10 Total BW of the two specimens of material Epoxy-1 during the ramping
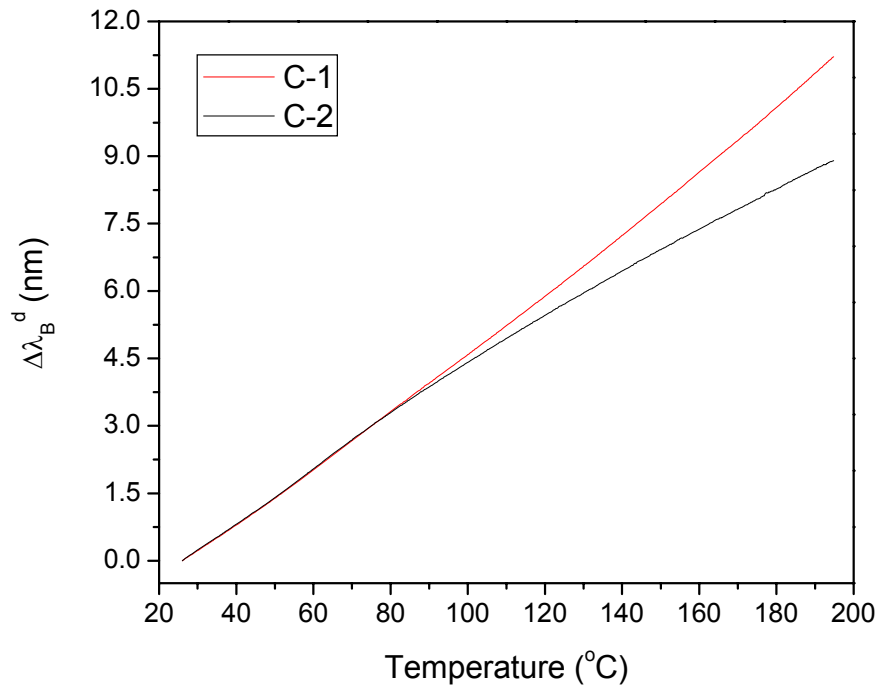
Fig. 5.11 Deformation induced BW of material Epoxy-1 during the ramping
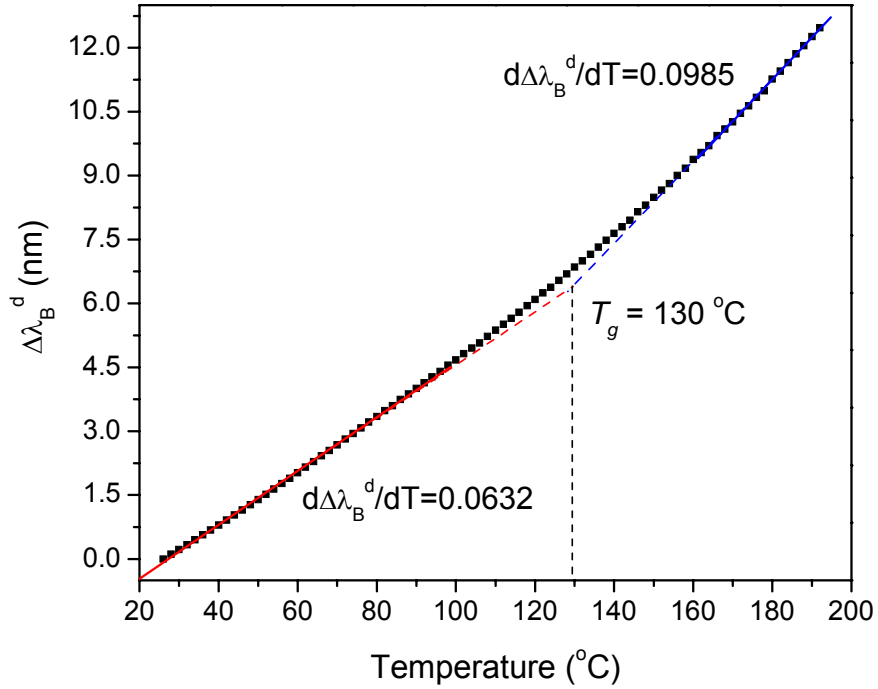
Fig. 5.12 BW of material Epoxy-1 and determination of CTE and T_g

5.1.2 Verification of the CTE and T_g measurement

The CTE and T_g of the tested polymer was also measured by a thermo-mechanical analyzer (TMA) for the purpose of verification. The instrument employed is Perkin Elmer TMA-7. It can work in a wide temperature range from -60 °C to 500 °C. The raw data obtained from TMA for the material UF-1, UF-2 and Epoxy-1 are shown in Fig. 5.13, Fig. 5.14 and Fig. 5.15, respectively.
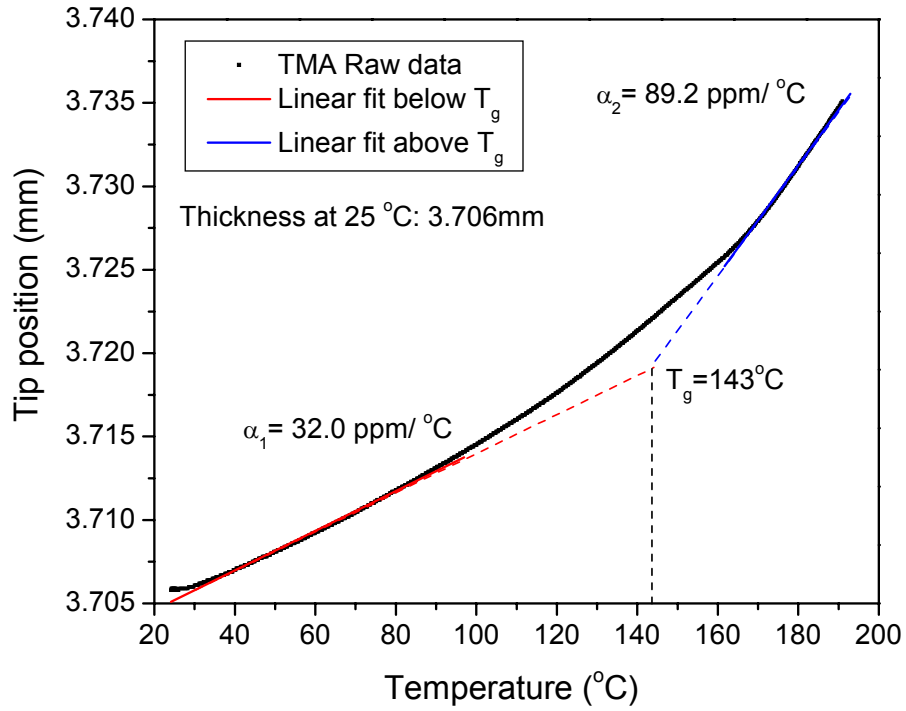
Fig. 5.13 Measurement of CTE and T_g of material UF-1 by TMA
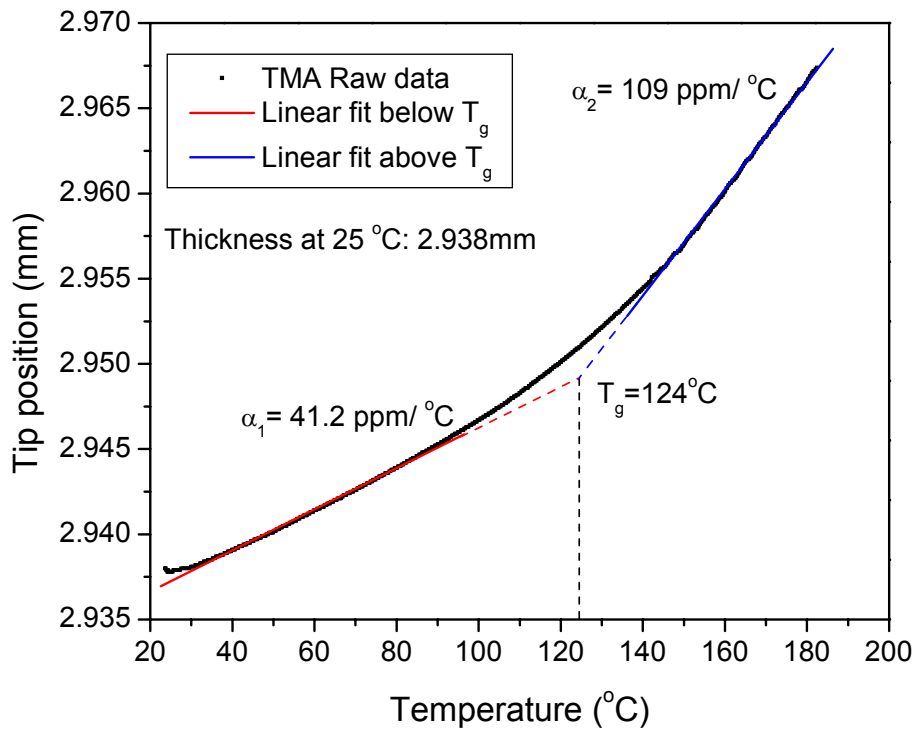
Fig. 5.14 Measurement of CTE and T_g of material UF-2 by TMA

142
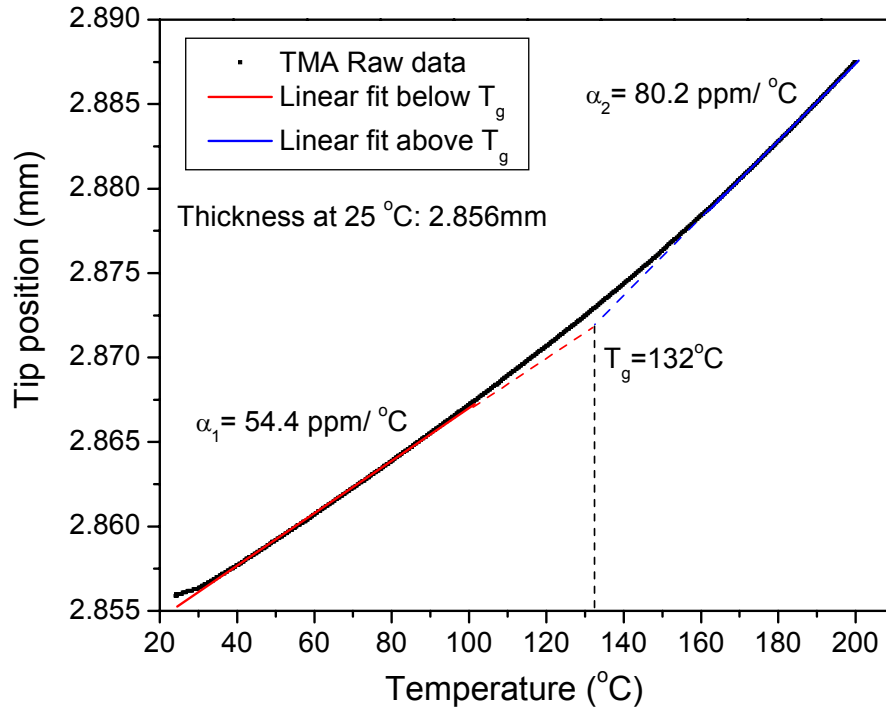
Fig. 5.15 Measurement of CTE and T_g of material Epoxy-1 by TMA

The CTE and T_g were calculated using Eqn. (2-9) and are compared with the values obtained from the proposed method. The results are summarized in the following table:

Table 5-1 Comparison of the results obtained from TMA and the proposed method

		CTE below T_g (ppm/°C)	CTE above T_g (ppm/°C)	T_g (°C)
UF-1	TMA	32.0	89.2	143
	Proposed Method	33.7	86.7	146
UF-2	TMA	41.2	109	124
	Proposed Method	42.5	106	120
Epoxy-1	TMA	54.4	80.2	132
	Proposed Method	52.9	82.1	130

143

As seen from the table, the results from the proposed method agree very well with the TMA results within the range of the experiment errors, which confirm the validity of the proposed method.

5.2 Determination of Visco-elastic Properties

5.2.1 Experimental setup and procedures

After the CTE and T_g were determined, the cured polymer/FBG specimen was used again for a creep test. The experimental setup is illustrated in Fig. 5.16.
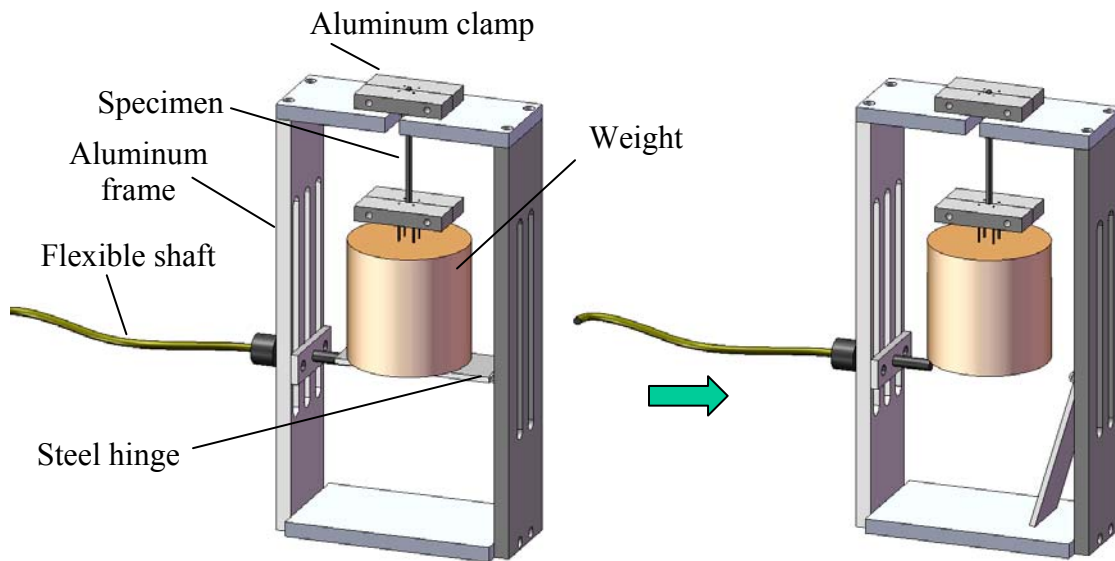
Fig. 5.16 Illustration of the creep testing setup and application of an instantaneous load

The experimental setup consists of an aluminum frame, two aluminum clamps, different weights, a steel hinge and a flexible shaft. Six brass cylinders with different dimensions

were fabricated as different weights. The dimensions and mass of those weights are summarized in Table 5-2,

Table 5-2 Dimensions and mass of different weights

	# 1	# 2	# 3	# 4	# 5	# 6
Diameter (")	2.5	2	1.5	1.25	1	1
Height (")	2.5	2	2	2	2	1
Mass (g)	1370	878	493	338	220	118

The whole setup was placed in a computer-controlled environmental chamber. The flexible shaft was inserted through the opening in the wall of the oven. A suitable weight, attached to the specimen, was supported by the hinge, allowing the specimen to be in the stress-free state initially. After the specimen was heated to the target temperature and stabilized, the support to the hinge was removed by twisting the flexible shaft. An instantaneous uni-axial load was thus applied to the specimen. The load was maintained for ten to twenty minutes and the BW shift was measured during the whole process. The above procedure was repeated at different temperatures, starting with high temperatures and going to low temperatures. The temperature and time dependent compliance of the polymer was then obtained. It should be noted that the test temperature is arranged from high to low in order to counteract the effect of iterative tension of the specimen.

5.2.2 Experimental results

A pure epoxy (Epoxy-2, EMC-1) was tested by the proposed method. After being cured at 120 °C for two hours using the mold illustrated in Fig. 4.6, a specimen of configuration C-1 was obtained. The specimen was clamped and inserted into the creep test setup shown in Fig. 5.16. The creep test was then carried out at various temperatures from 20 °C to 100 °C. The weights of #5, #4, #3 and #2 were used for temperatures 100 °C – 60 °C, 50 °C, 40 °C and 30 °C – 20 °C, respectively. The result of the recorded BW shift is shown in Fig. 5.17.
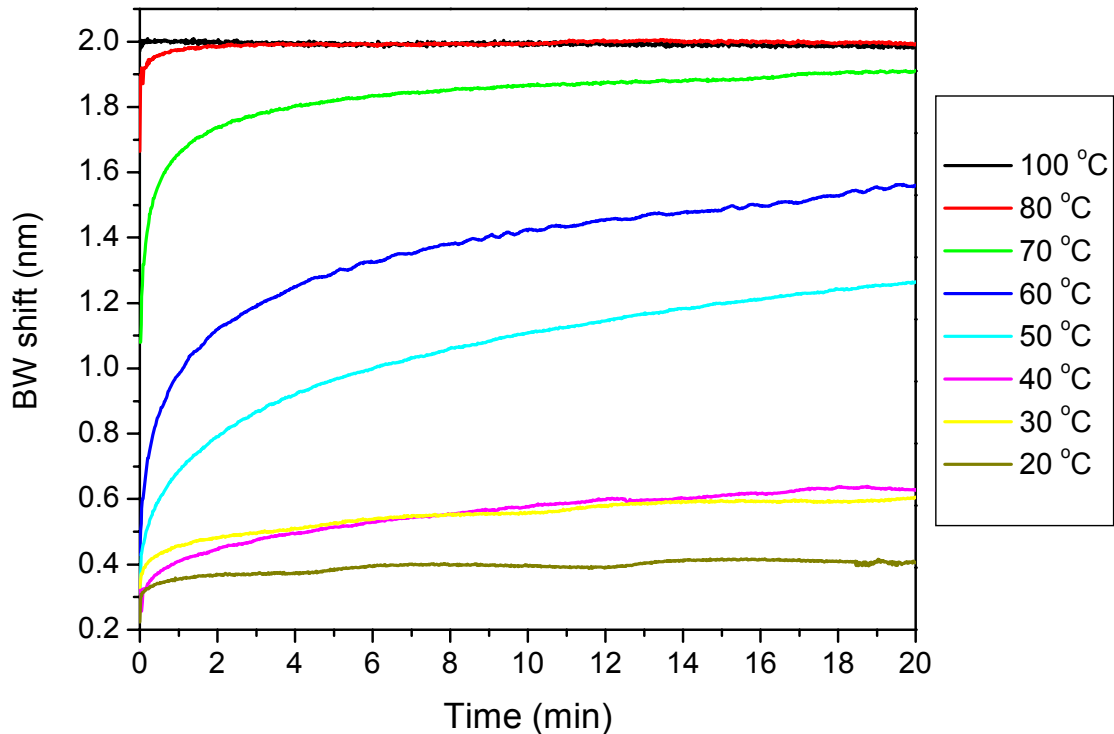
Fig. 5.17 BW shift of material Epoxy-2 recorded in the creep test

Using Eqn. (3-34), the time-dependent compliance at each temperature was calculated and the result is shown in Fig. 5.18. It can be seen from the figure that the compliance changes slowly at either low temperature or high temperature. At medial

temperature such as 60 °C, the compliance increases dramatically with the time. This is

because the polymer manifests a dramatic change at the vicinity of glass transition.
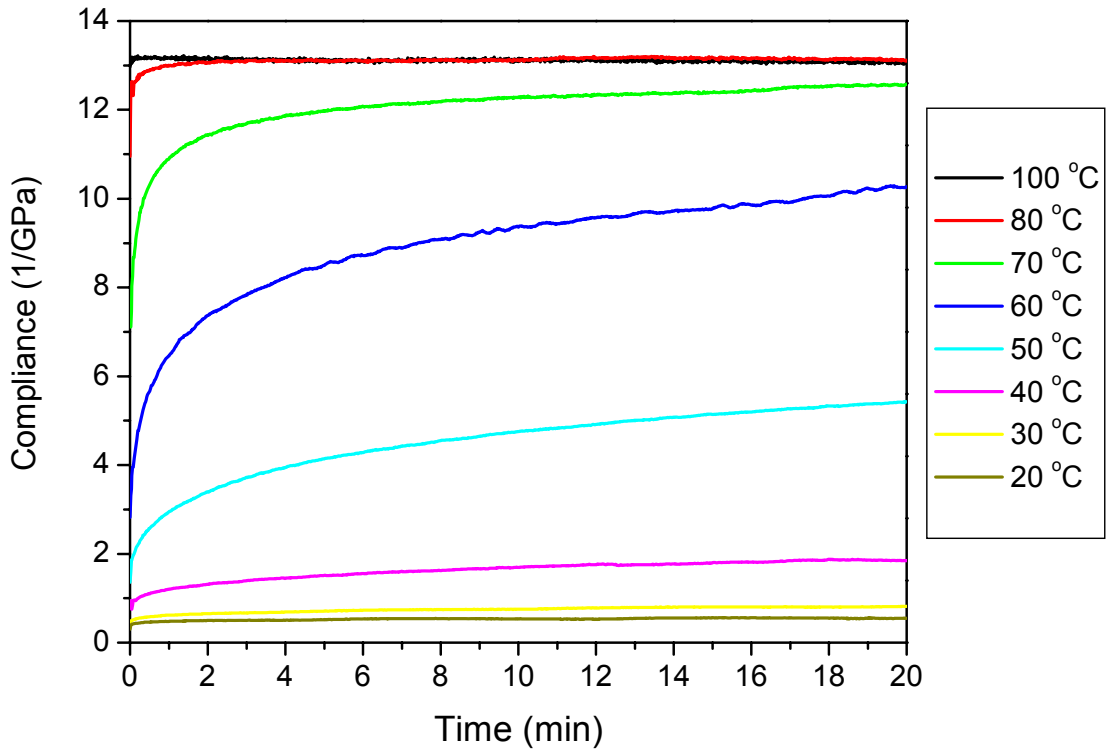
Fig. 5.18 Time-dependent compliance of material Epoxy-2 at different T

Through the de-convolution procedure described in Chapter 3.5, the measured

creep compliance can be transferred to the relaxation modulus. The de-convolution was

achieved by using a MATLAB program.   The program fits the compliance data,

approximates the integral by the sum of the series, and then calculates the modulus at

each time step using Eqn. (3-37). The result of obtained relaxation modulus at various

temperatures is shown in Fig. 5.19.

The relaxation modulus curves can be used to form a master curve. With 20 °C

chosen as the reference temperature, the assumption of "thermorheologically simple"

allows the modulus curves at other temperatures to be horizontally shifted along the

logarithmic time axis. The shifted was manually done to produce as smooth of a curve as

possible. The result is shown in Fig. 5.20.
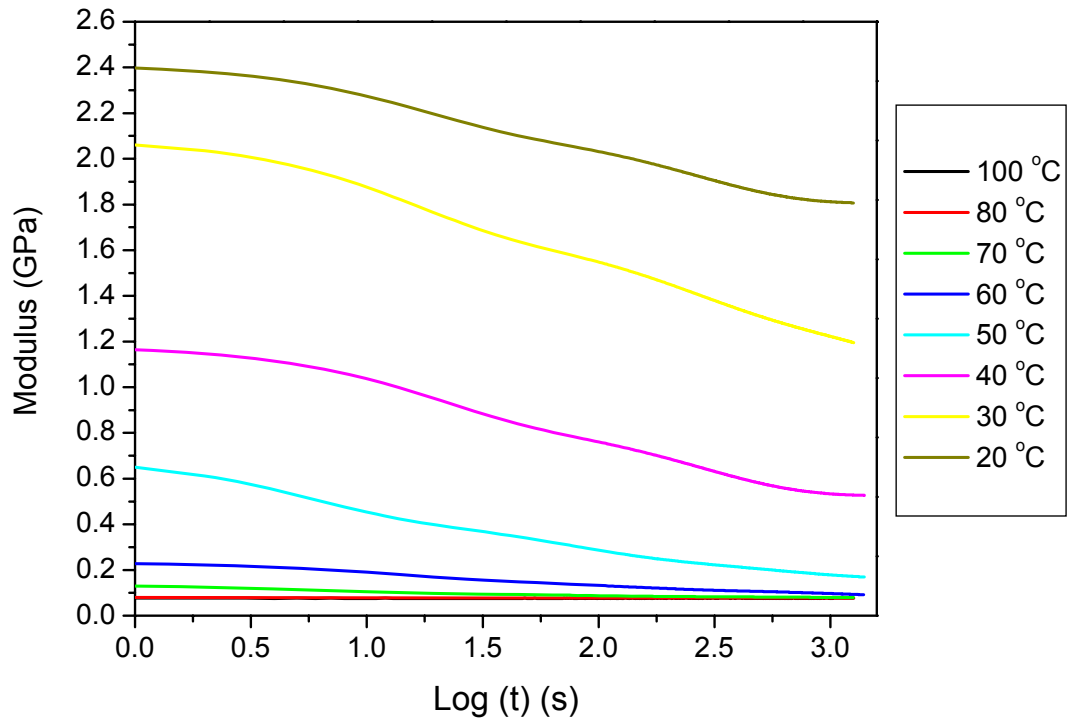
Fig. 5.19 Relaxation modulus of material Epoxy-2 at different T
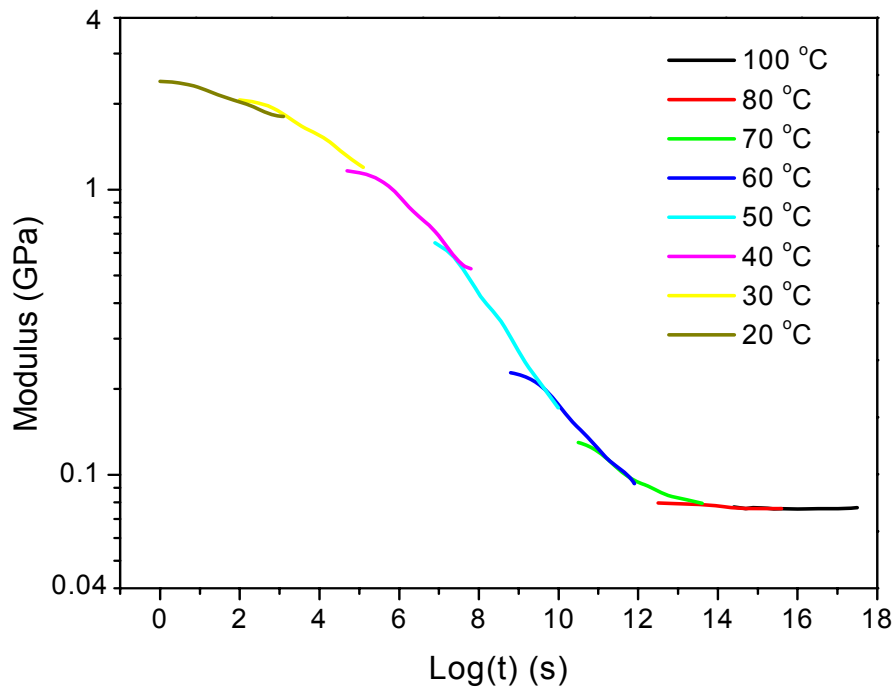
Fig. 5.20 Shifted relaxation modulus curves around a reference temperature of 20 °C

The shift factor which was used to shift the curves is plotted with the temperature in Fig. 5.21. The WLF function (see Eqn. (2-17)) was employed to fit the curve. The result is also shown in Fig. 5.21, which clearly indicates that the WLF function fits the shift factors well. The two constants, C_1 and C_2, are determined to be 47.0 and 175, respectively.
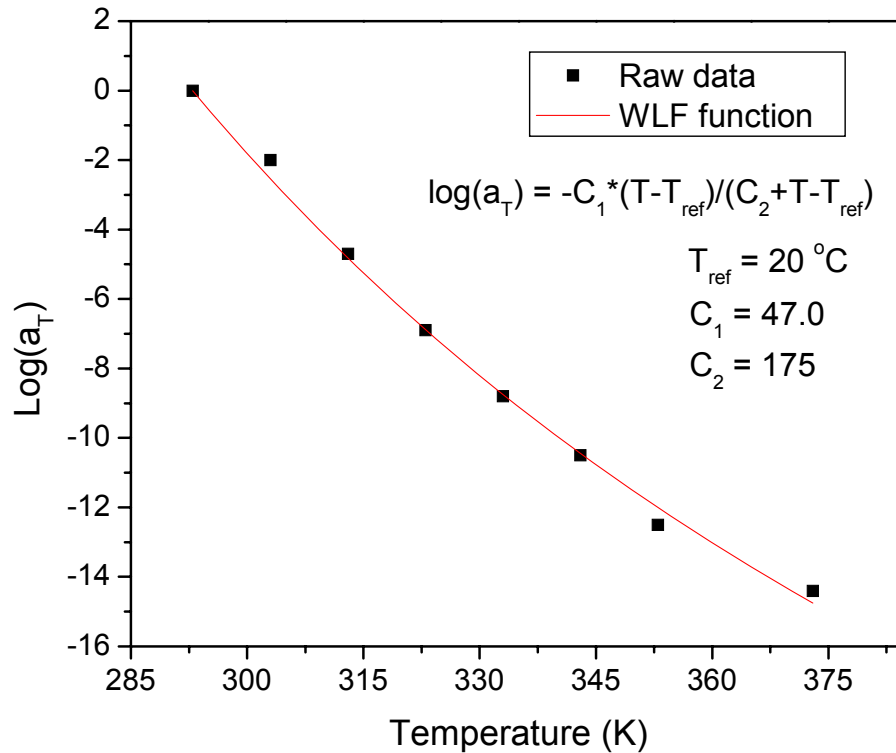
Fig. 5.21 Shift factors at various temperatures and fitted results using WLF function

The master curve can then be approximated by using several Prony Series terms. By averaging overlapping relaxation curves, and approximating spaces in between, a continuous master curve of the average relaxation modulus values for all temperatures between 100 °C and 20 °C was obtained. The result is shown in Fig. 5.22. To be readily implemented in commercial FEM software, the obtained master curve of relaxation

modulus was fitted by the Prony series (see Eqn. (3-42)) using a nonlinear regression scheme. The result is also shown in Fig. 5.22.

$$E(t) = E_\infty + \sum_{i=1}^{10} E_i \exp\left(-\frac{t}{\tau_i}\right)$$
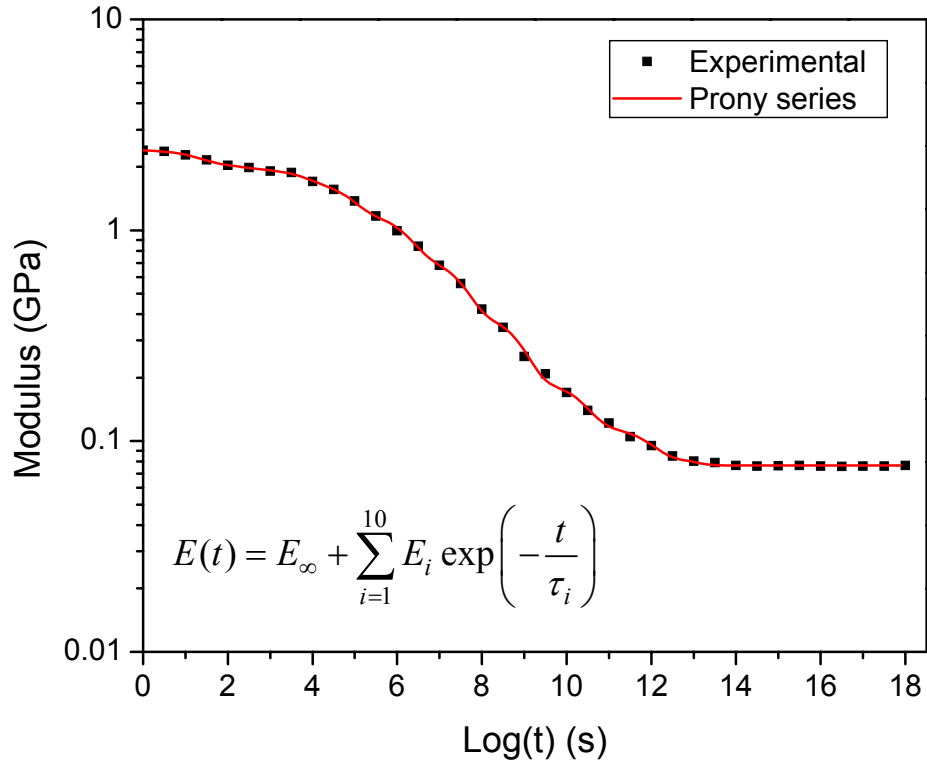
Fig. 5.22 Fitted result of master curve of Epoxy-2 using Prony series

Ten Prony pairs were employed in the fitting and they fit the master curve very well. The coefficients are tabled in the following

Table 5-3 Coefficients in the Prony series of material Epoxy-2

	i = 1	i = 2	i = 3	i = 4	i = 5	i = 6	i = 7	i = 8	i = 9	i = 10
E_i (GPa)	0.323	0.122	0.245	0.50	0.456	0.355	0.212	0.076	0.033	0.008
τ_i (s)	22	202	6800	$9*10^4$	$2*10^6$	$4*10^7$	$1*10^9$	$3*10^{10}$	$1*10^{12}$	$1*10^{13}$

with $E_\infty = 0.076 GPa$.

The above procedure was repeated for the material UF-2. The creep test was carried out at various temperatures from 175 °C to 30 °C. The weights of #5, #4, #3 and #2 were used for temperatures 175 °C – 145 °C, 135 °C, 125 °C and 115 °C – 30 °C, respectively. The result of the recorded BW shift is shown in Fig. 5.23.
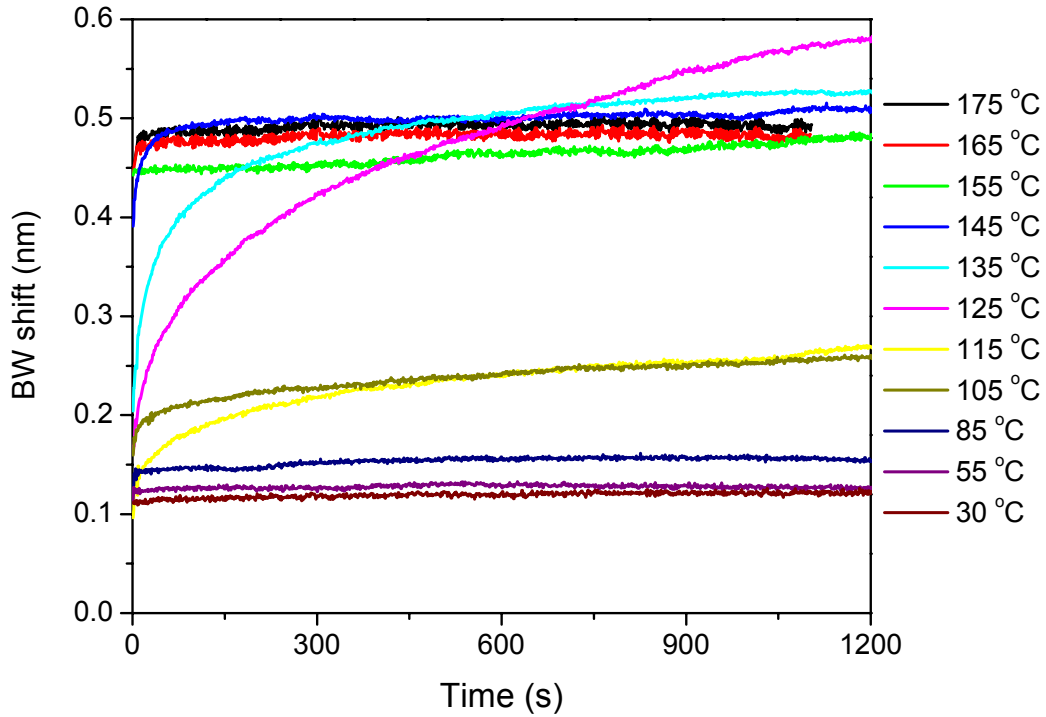
Fig. 5.23 BW shift of material UF-2 recorded in the creep test

After the de-convolution procedure, the relaxation modulus at various temperatures was obtained and the result is shown in Fig. 5.24. The master curve of the relaxation modulus was formed and the result is shown in Fig. 5.25 where the reference temperature is 30 °C.
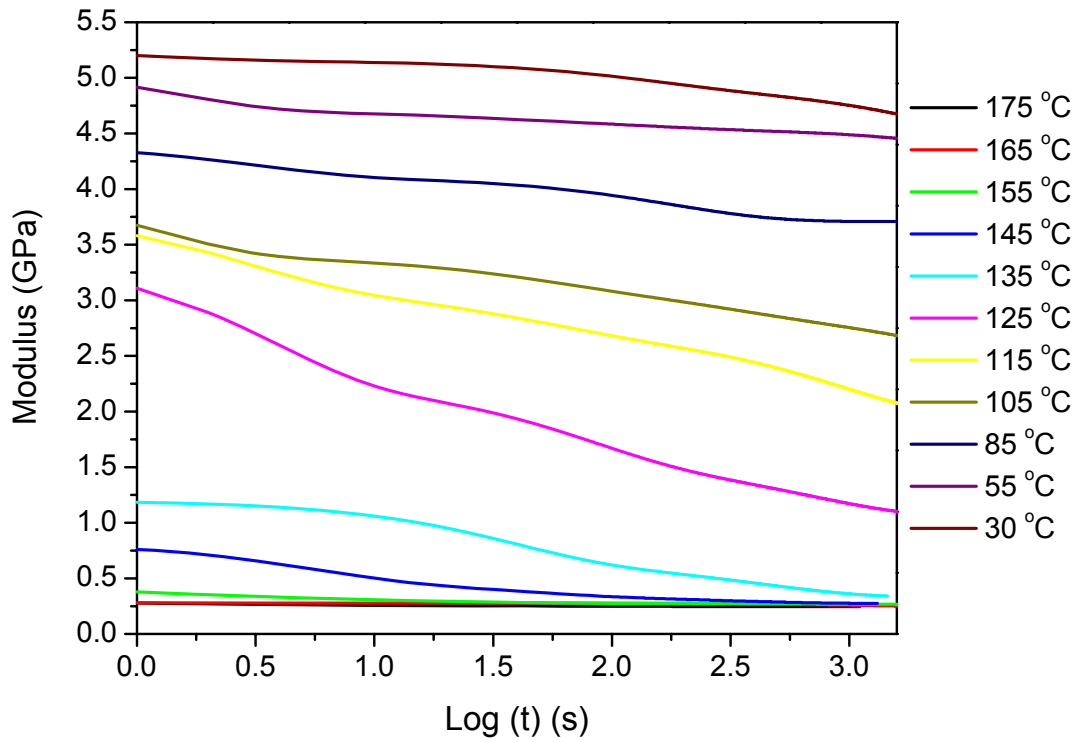
Fig. 5.24 Relaxation modulus of material UF-2 at different T
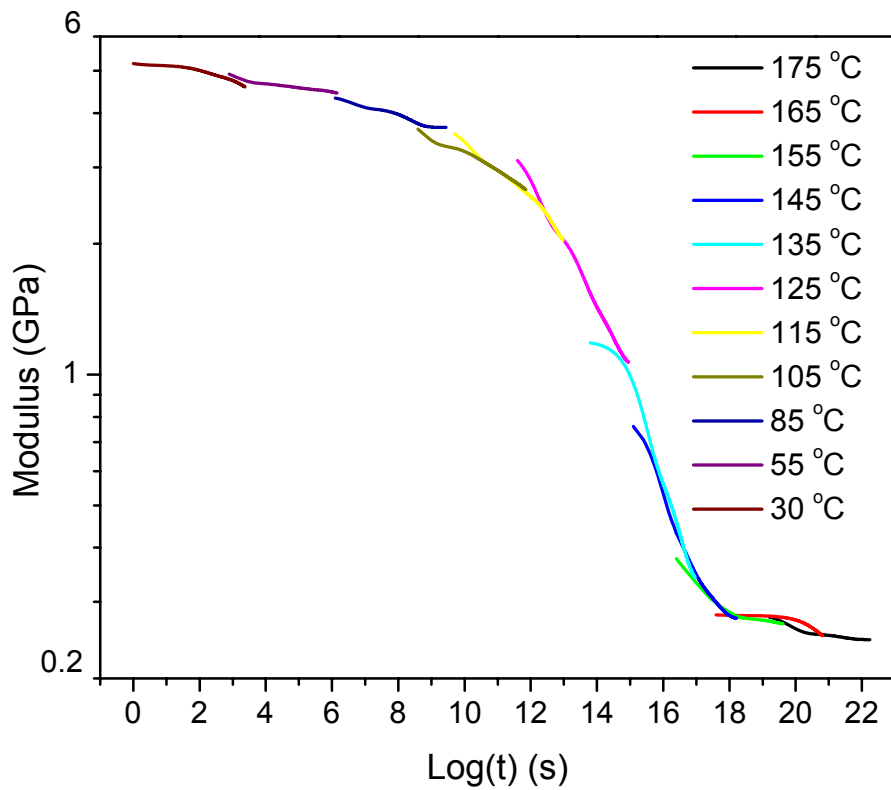
Fig. 5.25 Shifted relaxation modulus curves around a reference temperature of 30 °C

152

The shift factors and the 11 Prony Series results are shown in Figs. 5.26 and 5.27, respectively.
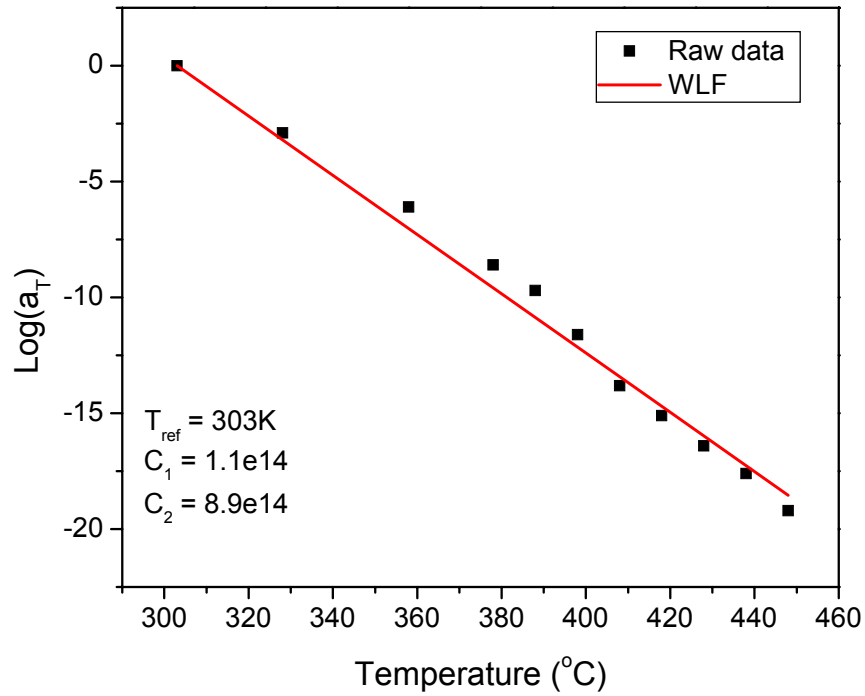
Fig. 5.26 Shift factors of UF-2 and fitted results using WLF function

$$E(t) = E_\infty + \sum_{i=1}^{11} E_i \exp\left(-\frac{t}{\tau_i}\right)$$
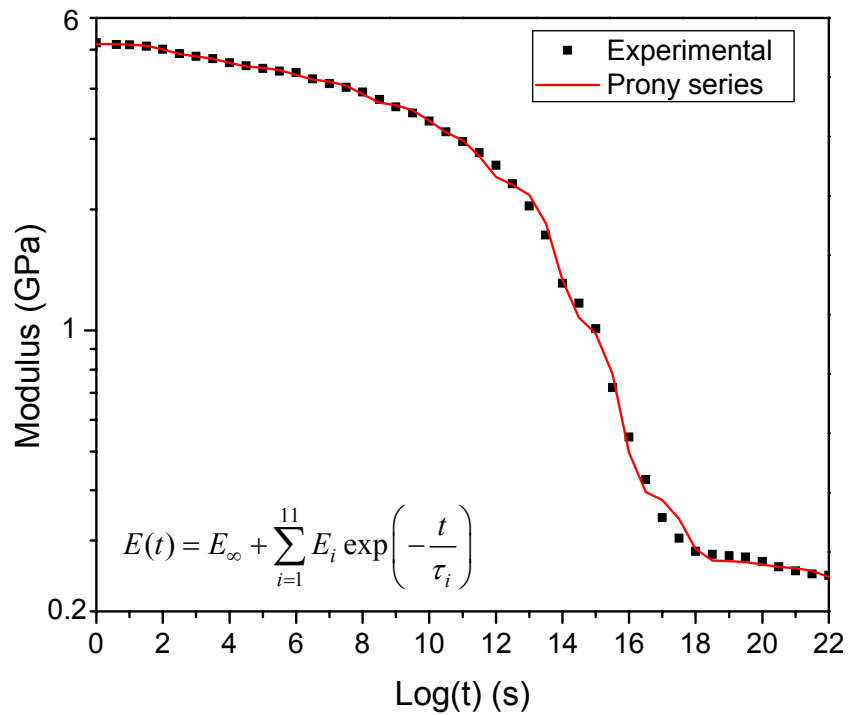
Fig. 5.27 Fitted result of master curve of UF-2 using Prony series

153

The coefficients are tabled in the following

Table 5-4 Coefficients in the Prony series of material UF-2

	i = 1	i = 2	i = 3	i = 4	i = 5	i = 6	i = 7	i = 8	i=9	i = 10	i = 11
E_i (GPa)	0.33	0.298	0.327	0.52	0.54	0.78	1.26	0.71	0.13	0.01	0.023
τ_i (s)	160	9500	$1*10^6$	$1*10^8$	$1*10^{10}$	$4*10^{11}$	$6*10^{13}$	$5*10^{15}$	$5*10^{17}$	$1*10^{20}$	$1*10^{22}$

with $E_\infty = 0.235 GPa$

5.3 Application of the Measured Properties

The material properties measured with the proposed technique include: the evolutions of effective chemical shrinkage and modulus during curing, temperature-dependent CTE and T_g, and visco-elastic properties. Those properties can be employed to assess the curing related residual stresses in electronic packages.

To calculate the residual stress or deformation of packages after the curing, the following numerical procedure can be used:

1. Geometry modeling of the package in finite element codes such as ANSYS.

2. Divide the curing process into small segments and determine the chemical shrinkage increment ($\Delta\varepsilon^{ch}$) and instantaneous modulus (E) in each segment. By the analogy between chemical shrinkage and thermal shrinkage, apply a pseudo-temperature decrease of $\Delta T = \dfrac{\Delta\varepsilon^{ch}}{\alpha}$ to the polymeric material with an elastic

modulus of E and no temperature change to the other materials, where α is the CTE of the polymer.

3. Calculate the stress/displacement field in each segment.

4. Superpose the stress/displacement field of all segments. The results will be the stress/displacement field in the package when the curing process ends. Record the new position of each node.

5. Re-model the package according to the recorded new position of each node.

6. Attribute the measured temperature-dependent CTE and relaxation modulus to the polymer. Apply the thermal loading conditions and calculate the final stress/displacement filed after the cooling from the curing temperature.

As an illustration, the curing induced warpage of a flip-chip package is simulated. The package is illustrated in Fig. 5.28. It comprises of a substrate, an underfill material (UF-2) and a chip. For simplicity, the solder balls were not modeled.
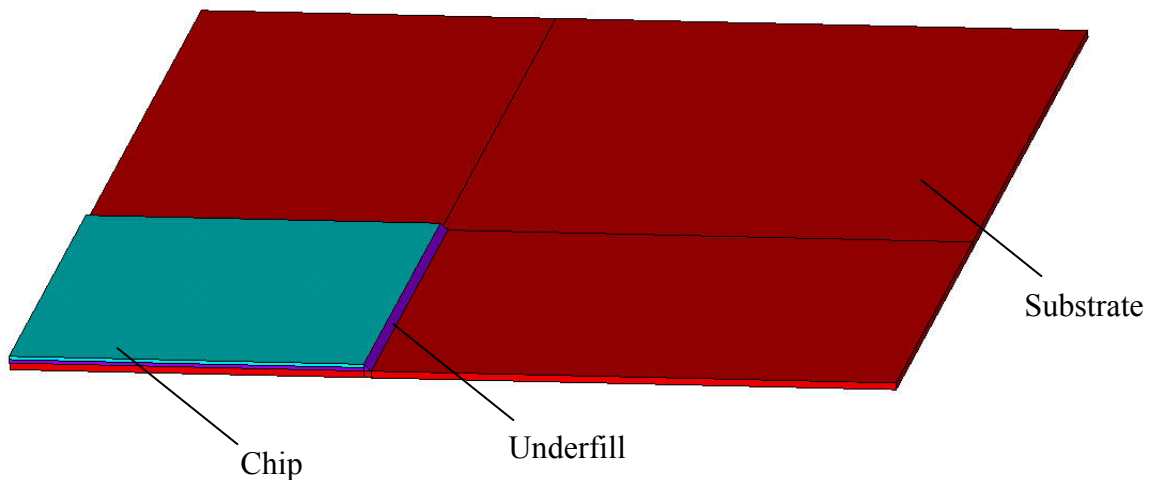
Fig. 5.28 Illustration of the flip-chip package

The substrate has a thickness of 200 μm and a width of 50 mm, the chip has a thickness of 100 μm and a width of 20 mm, and the thickness of the underfill is 100 μm. The commercial FEM software ANSYS was used to build the model. The mesh of the model is shown in Fig. 5.29.
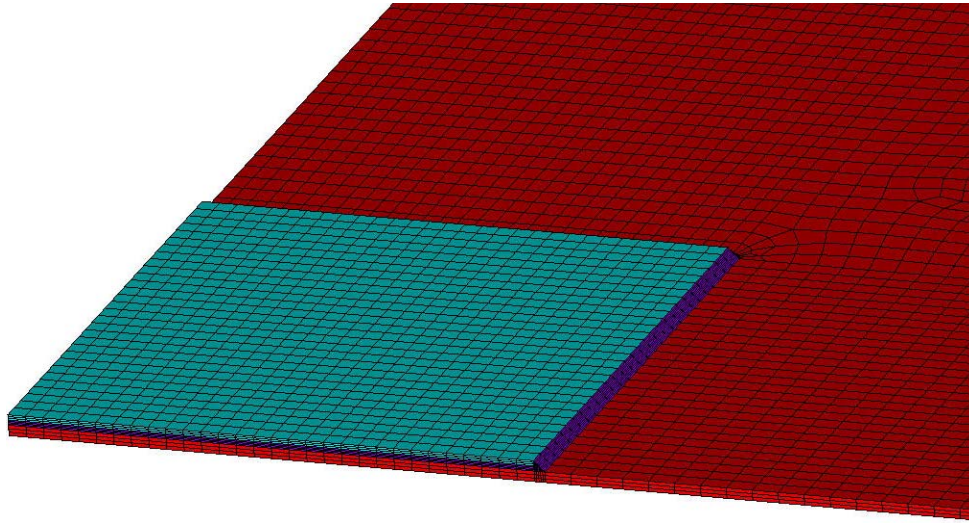
Fig. 5.29 Mesh of the flip-chip package modeling

The material properties of the substrate and chip used in the simulation are summarized in Table 5-5.

Table 5-5 Material properties of the substrate and chip

	Young's Modulus (GPa)	Poisson's ratio	CTE (ppm/°C)
Substrate	20	0.3	10
Chip	169	0.28	2.7

The effective chemical shrinkage and modulus evolutions of the underfill can be determined by following the procedure described in section 4.5. The temperature-dependent CTE and the master curve of the underfill can be found in Fig. 5.8 and Fig.5.27, respectively.

Assuming a constant cooling rate of 15°C/min to the room temperature of 25 °C after the curing, the final warpage of the flip-chip package was calculated when cured at various curing temperatures from 185 °C to 145 °C. Figure 5.30 shows a representative result of the final warpage when cured at 175 °C.

-.645356   -.501943   -.358531   -.215119   -.071706
      -.573649   -.430237   -.286825   -.143412   0
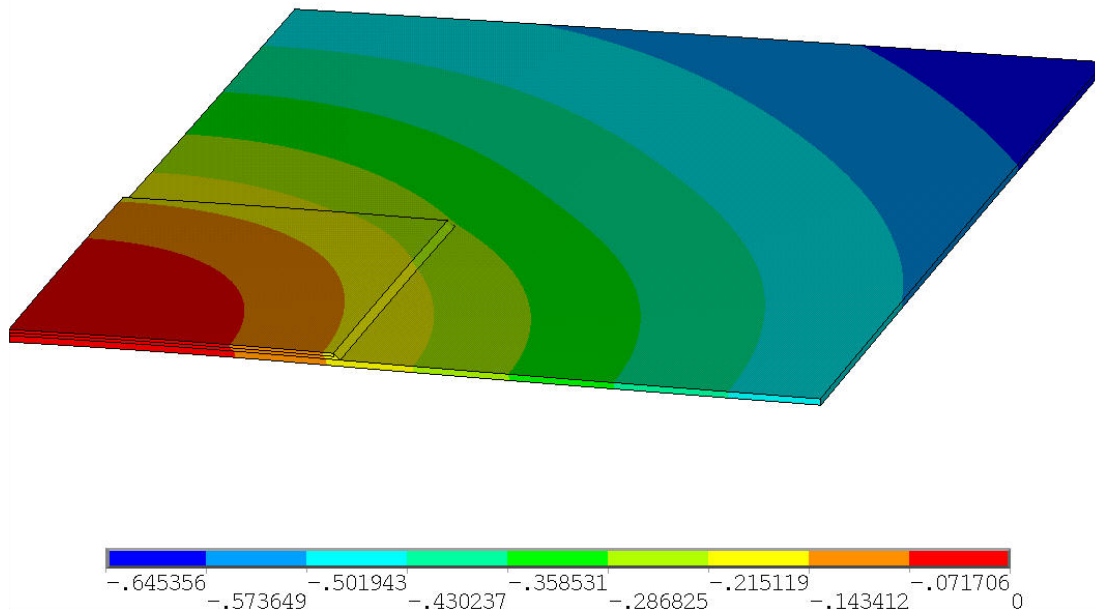
Fig. 5.30 Final warpage when cured at 175 °C (unit: mm)

Furthermore, the maximum warpage versus curing temperature is plotted in Fig. 5.31.

The curing time is also important in manufacturing. The characteristic curing time for the polymer's modulus to reach 90% of the one in the completely cured state was determined as a function of curing temperature. A gelation point of 0.5 is first assumed. Then Eqn. (4-1) yields the corresponding curing extent of 0.985.

The following differential equation was solved to determine the characteristic curing time, $\bar{t}$, corresponding the curing extent of 0.985.

$$\frac{dp}{dt} = 1.78 \cdot 10^9 \cdot \exp\left(-\frac{89000}{8.314 \cdot T}\right)(1-p)^{1.6}$$

(5-1)

B.C. $p(0) = 0$ *and* $p(\bar{t}) = 0.985$

(5-2)

The characteristic curing time was determined for various temperatures between 145 °C and 185 °C. The result is also plotted in Fig. 5.31.
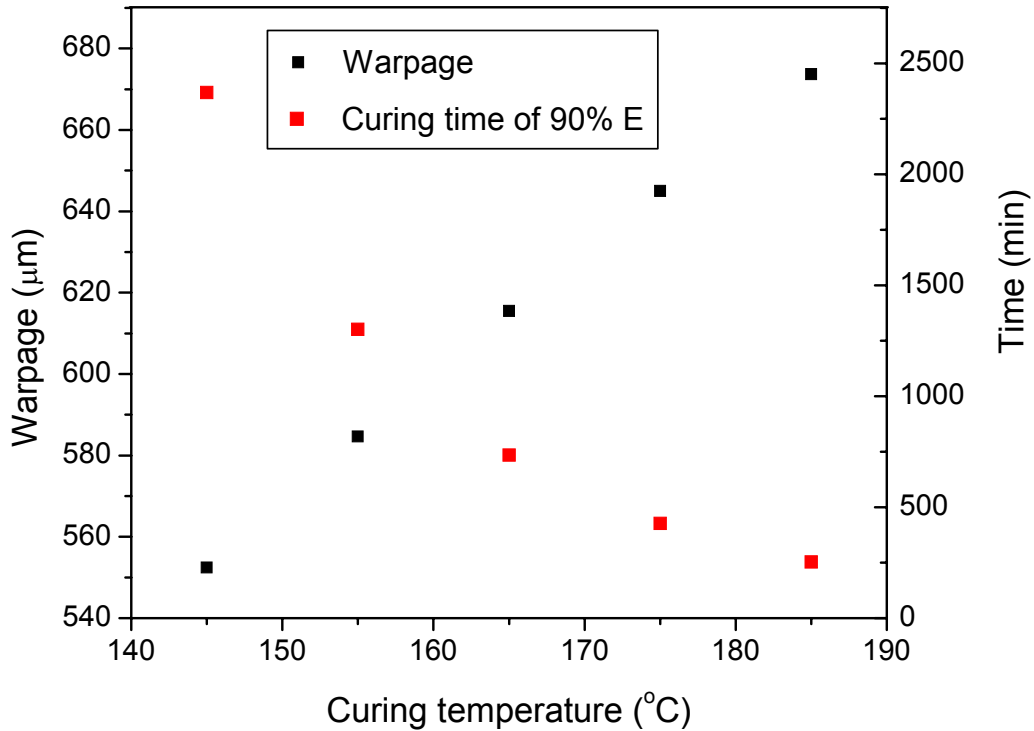
Fig. 5.31 Final warpage and characteristic curing time at different temperatures

Figure 5.31 shows tradeoffs between the final warpage and the curing time. A lower curing temperature can reduce the final package warpage, but the curing time is dramatically increased. An optimum curing schedule should be selected carefully.

Chapter 6 Conclusions and Future Work

6.1 Conclusions

An integrated measurement technique based on fiber Bragg grating (FBG) sensors was proposed to measure the critical properties of polymeric materials. An analytical solution of the FBG sensor's response when embedded in an annular substrate was first derived and validated, which served as the theoretical base for the proposed method. Then a systematic study was conducted to investigate the effect of curing induced heat generation and the sensitivity of the BW shift to the outer radius and Poisson's ratio of the polymer. Based on the results, two different specimen configurations were proposed for the measurement of properties. Theoretical formulations and numerical procedures to determine the properties were established for the two proposed specimen configurations.

The technique was implemented with various polymeric materials. In the experimental procedure, the polymer was cured around FBG sensors to form a cylindrical shape. Through the Bragg wavelength (BW) shifts measured during the curing of the polymer, the evolutions of effective chemical shrinkage and modulus of the polymer as a function of time were determined simultaneously. With the aid of curing kinetics modeling, the obtained results were used to predict the property evolutions at other curing temperatures. The specimens were then subjected to a temperature excursion. The temperature-dependent coefficient of thermal expansion (CTE) and glass transition temperature (T_g) were determined from the BW shifts documented during the ramping process. Finally, an instantaneous uni-axial mechanical load was applied to the specimen at different temperatures, and the corresponding creep compliance was determined. The

master curve of the relaxation modulus was then obtained through a de-convolution process.

The accuracy of the experimental raw data (BG shifts) was validated through a self-consistency test. The results confirmed the robustness of the experimental setup. The measured effective chemical shrinkage and modulus evolutions were validated through the curing induced bending deformation of a bi-material strip. The CTE and T_g were also verified using a TMA. All of these results confirm the validity of the proposed method.

The proposed technique will provide a much-needed tool for *rapid but accurate* assessment of polymer properties, which, in turn, will enhance the accuracy of predictive modeling for design optimization of a microelectronics product at the conceptual stage of product development.

6.2 Suggestions for Future Work

Polymers with extreme curing rates

Although optimized, the temperature overshoot can be large for polymers with extremely high curing rates. To reduce the uncertainty caused by the temperature overshoot, two possible solutions can be sought.

(1) By developing FBGs with a smaller radius, C-1 configuration can be proportionally smaller. The curing induced temperature overshoot will be diminished while the measurement sensitivity is maintained.

(2) Instead of using the convection oven, a conduction oven can be used to control the specimen temperature in such a way that the surface temperature control can compensate the temperature overshooting at the center.

Material degradation or aging

Although the work of this dissertation addresses only the key idea of being able to determine authentic material properties of polymers, other important applications would be realized from the versatility of the proposed method. One immediate spin-off is determination of material degradation or aging. The proposed approach can be extended to determine the effect of environmental conditions, such as temperature and humidity, as well as cyclic loading and mechanical impact, on the long-term durability of such polymers. Determination of material degradation parameters associated with the environmental conditions is possible from the time history of the measured Bragg wavelength shift.

Appendix

A. Analytical solution of the stress fields within the FBG

     The fiber is assumed to be a solid cylinder with outer radius a, while the substrate has inner radius a and outer radius b. The subscripts, "f" and "s" are used to identify the fiber and substrate parameters, respectively. The general elastic solution can be expressed as:

$$\sigma_{rr}(r) = -\frac{\alpha_f E_f}{1-\nu_f}\frac{1}{r^2}\int_0^r rT(r)dr + \frac{E_f}{1+\nu_f}\left[\frac{C_{1f}}{1-2\nu_f} - \frac{C_{2f}}{r^2}\right], \quad 0 \leq r \leq a, \tag{A-1}$$

$$\sigma_{\theta\theta}(r) = \frac{\alpha_f E_f}{1-\nu_f}\left[\frac{1}{r^2}\int_0^r rT(r)dr - T(r)\right] + \frac{E_f}{1+\nu_f}\left[\frac{C_{1f}}{1-2\nu_f} + \frac{C_{2f}}{r^2}\right], \quad 0 \leq r < a \tag{A-2}$$

$$\sigma_{rr}(r) = -\frac{\alpha_s E_s}{1-\nu_s}\frac{1}{r^2}\int_a^r rT(r)dr + \frac{E_s}{1+\nu_s}\left[\frac{C_{1s}}{1-2\nu_s} - \frac{C_{2s}}{r^2}\right], \quad a \leq r \leq b, \tag{A-3}$$

$$\sigma_{\theta\theta}(r) = \frac{\alpha_s E_s}{1-\nu_s}\left[\frac{1}{r^2}\int_a^r rT(r)dr - T(r)\right] + \frac{E_s}{1+\nu_s}\left[\frac{C_{1s}}{1-2\nu_s} + \frac{C_{2s}}{r^2}\right], \quad a < r \leq b \tag{A-4}$$

$$\sigma_{zz}(r) = \left[\nu\left(\sigma_{rr} + \sigma_{\theta\theta}\right) - E\alpha T(r)\right] + \sigma_{zz}^0. \tag{A-5}$$

In the loading condition of the piecewise constant temperature distribution,

$$T(r) = \begin{cases} T_f, & 0 \leq r < a \\ T_s, & a < r \leq b \end{cases} \tag{A-6}$$

The general solution given from (A-1) to (A-4) are reduced to

$$\sigma_{rr}(r) = -\frac{\alpha_f E_f T_f}{2(1-\nu_f)} + \frac{E_f}{1+\nu_f}\left[\frac{C_{1f}}{1-2\nu_f} - \frac{C_{2f}}{r^2}\right], \quad 0 \leq r \leq a, \tag{A-1'}$$

$$\sigma_{\theta\theta}(r) = -\frac{\alpha_f E_f T_f}{2(1-\nu_f)} + \frac{E_f}{1+\nu_f}\left[\frac{C_{1f}}{1-2\nu_f} + \frac{C_{2f}}{r^2}\right], \quad 0 \le r < a \tag{A-2'}$$

$$\sigma_{rr}(r) = -\frac{\alpha_s E_s T_s}{1-\nu_s}\frac{r^2-a^2}{2r^2} + \frac{E_s}{1+\nu_s}\left[\frac{C_{1s}}{1-2\nu_s} - \frac{C_{2s}}{r^2}\right], \quad a \le r \le b, \tag{A-3'}$$

$$\sigma_{\theta\theta}(r) = -\frac{\alpha_s E_s T_s}{1-\nu_s}\frac{r^2+a^2}{2r^2} + \frac{E_s}{1+\nu_s}\left[\frac{C_{1s}}{1-2\nu_s} + \frac{C_{2s}}{r^2}\right], \quad a < r \le b \tag{A-4'}$$

The coefficients can be expressed as

$$C_{1s} = \frac{A+B}{C+D}$$

$$C_{2s} = C_{1s}\frac{b^2}{1-2\nu_s} - \frac{1+\nu_s}{1-\nu_s}\frac{\alpha_s T_s}{2}\left(b^2-a^2\right)$$

$$C_{1f} = C_{1s}\left(1-\frac{b^2}{a^2}\right)\frac{E_s}{E_f}\frac{\left(1+\nu_f\right)\left(1-2\nu_f\right)}{\left(1+\nu_s\right)\left(1-2\nu_s\right)}$$

$$+\frac{\left(1+\nu_f\right)\left(1-2\nu_f\right)\alpha_f T_f}{1-\nu_f}\frac{\alpha_f T_f}{2} + \frac{E_s}{E_f}\left(\frac{b^2}{a^2}-1\right)\frac{\left(1+\nu_f\right)\left(1-2\nu_f\right)}{1-\nu_s}\frac{\alpha_s T_s}{2}$$

$$C_{2f} = 0$$

where

$$A = \left(\frac{b^2}{a^2}-1\right)\frac{\alpha_s T_s}{1-\nu_s}\left[\frac{1+\nu_s}{2} - \frac{\left(\nu_f-\nu_s\right)\dfrac{E_s}{E_f}}{1+\dfrac{E_s}{E_f}\left(\dfrac{b^2}{a^2}-1\right)}\right] + \frac{\alpha_f T_f}{1-\nu_f}\left[\frac{1+\nu_f}{2} - \frac{\left(\nu_f-\nu_s\right)}{1+\dfrac{E_s}{E_f}\left(\dfrac{b^2}{a^2}-1\right)}\right]$$

$$B = \left\{ \frac{E_s}{E_f}\left(\frac{b^2}{a^2} - 1\right)\frac{\alpha_s T_s}{2}\frac{(1+v_f)(1-2v_f)}{(1-v_s)} + \frac{\alpha_f T_f}{2}\frac{(1+v_f)(1-2v_f)}{(1-v_f)} \right\}$$

$$\times \left\{ 1 + \frac{2v_f(v_f - v_s)}{(1+v_f)(1-2v_f)\left[1 + \frac{E_s}{E_f}\left(\frac{b^2}{a^2} - 1\right)\right]} \right\}$$

$$C = 1 + \frac{b^2}{a^2}\frac{1}{1-2v_s} - \frac{E_s}{E_f}\frac{2v_s(v_f - v_s)\left(\frac{b^2}{a^2} - 1\right)}{(1+v_s)(1-2v_s)\left[1 + \frac{E_s}{E_f}\left(\frac{b^2}{a^2} - 1\right)\right]}$$

$$D = \frac{E_s}{E_f}\left(\frac{b^2}{a^2} - 1\right)\frac{(1+v_f)(1-2v_f)}{(1+v_s)(1-2v_s)}\left\{ 1 + \frac{2v_f(v_f - v_s)}{(1+v_f)(1-2v_f)\left[1 + \frac{E_s}{E_f}\left(\frac{b^2}{a^2} - 1\right)\right]} \right\}$$

B. Analytical solution of curing induced warpage of a bi-material strip

For the bi-material strip shown in Fig. 4.28, a bending deformation will occur when a chemical shrinkage of $\Delta\varepsilon^{ch}$ develops in the polymer layer. Assume the bending curvature is κ and the strain on the layer boundary is ε_0 after the bending. Then the stresses in the top and bottom layers can be calculated as

$$\sigma_1 = E_1(\varepsilon_0 + \kappa y - \Delta\varepsilon^{ch}) \tag{B-1}$$

$$\sigma_2 = E_2(\varepsilon_0 + \kappa y) \tag{B-2}$$

From the boundary conditions of zero net force and moment in the cross-section,

$$\int_0^{t_1} \sigma_1 dy + \int_{-t_2}^0 \sigma_2 dy = 0 \tag{B-3}$$

$$\int_0^{t_1} \sigma_1 y dy + \int_{-t_2}^0 \sigma_2 y dy = 0 \tag{B-4}$$

Substituting Eqs. (B-1) and (B-2) into (B-3) and (B-4) will yield

$$E_1(\varepsilon_0 - \Delta\varepsilon^{ch})t_1 + E_2\varepsilon_0 t_2 + \frac{E_1 t_1^2 - E_2 t_2^2}{2}\kappa = 0 \tag{B-5}$$

$$E_1(\varepsilon_0 - \Delta\varepsilon^{ch})\frac{t_1^2}{2} - E_2\varepsilon_0 \frac{t_2^2}{2} + \frac{E_1 t_1^3 + E_2 t_2^3}{3}\kappa = 0 \tag{B-6}$$

Solving the simultaneous Eqns. (B-5) and (B-6) yields the curvature as

$$y'' = \kappa = \frac{6(t_1 + t_2)E_1 E_2 t_1 t_2 \Delta\varepsilon^{ch}}{E_1^2 t_1^4 + 6E_1 E_2 t_1^2 t_2^2 + E_2^2 t_2^4 + 4E_1 E_2 t_1^3 t_2 + 4E_1 E_2 t_1 t_2^3} \tag{B-7}$$

Integrating the curvature yields the warpage at $x = L$ as

$$y\big|_{x=L} = \frac{3(t_1 + t_2)E_1 E_2 t_1 t_2 L^2}{E_1^2 t_1^4 + 6E_1 E_2 t_1^2 t_2^2 + E_2^2 t_2^4 + 4E_1 E_2 t_1^3 t_2 + 4E_1 E_2 t_1 t_2^3}\Delta\varepsilon^{ch} \tag{B-8}$$

References

[1]   D. Chung, "Materials for electronic packaging," *Butterworth-Heinemann,* 1995.

[2]   T. A. Osswald and G. Menges, "Materials science of polymers for engineers," *Hanser Gardner Publications, Inc., Cincinnati,* 2003.

[3]   F. Rodriguez, "Principles of polymer systems," *Taylor & Francis Inc., Washington DC,* 1996.

[4]   T. A. Bogetti and J. W. Gillespie, "Process-induced stress and deformation in thick-section thermoset composite laminates," *Journal of Composite Materials,* vol. 26, pp. 626-660, 1992.

[5]   F. Su, L. Liu, and T. Wang, "Evaluation of residual stress in flip chip using 3-D optical Interferometry/FEM hybrid technique," *Strain,* vol. 43, pp. 289-298, Nov 2007.

[6]   M. Y. Tsai, C. H. J. Hsu, and C. T. O. Wang, "Investigation of thermomechanical behaviors of flip chip BGA packages during manufacturing process and thermal cycling," *Ieee Transactions on Components and Packaging Technologies,* vol. 27, pp. 568-576, Sep 2004.

[7]   M. Y. Tsai, Y. C. Lin, C. Y. Huang, and J. D. Wu, "Thermal deformations and stresses of flip-chip BGA packages with low- and high-T-g underfills," 2005, pp. 328-337.

[8]   W. G. Zhang, D. Wu, B. Z. Su, S. A. Hareb, Y. C. Lee, and B. P. Masterson, "The effect of underfill epoxy on warpage in flip-chip assemblies," *Ieee Transactions on Components Packaging and Manufacturing Technology Part A,* vol. 21, pp. 323-329, Jun 1998.

[9]   G. Kelly, C. Lyden, W. Lawton, J. Barrett, A. Saboui, H. Pape, and H. J. B. Peters, "Importance of molding compound chemical shrinkage in the stress and warpage analysis of PQFP's," *Ieee Transactions on Components Packaging and Manufacturing Technology Part B-Advanced Packaging,* vol. 19, pp. 296-300, May 1996.

[10]   D. G. Yang, L. J. Ernst, C. van't Hof, M. S. Kiasat, J. Bisschop, J. Janssen, F. Kuper, Z. N. Liang, R. Schravendeel, and F. Q. Zhang, "Vertical die crack stresses of Flip Chip induced in major package assembly processes," 2000, pp. 1533-1538.

[11]   K. Oota and M. Saka, "Cure shrinkage analysis of epoxy molding compound," *Polymer Engineering and Science,* vol. 41, pp. 1373-1379, Aug 2001.

[12]   M. C. Larson, M. A. Verges, and X. Liu, "Residual compression in area array packages induced by underfill shrinkage," *Microelectronics Reliability,* vol. 46, pp. 496-502, Feb-Apr 2006.

[13]   D. Lu and C. P. Wong, "Materials for Advanced Packaging," *Springer-Verlag New York, Inc.,* 2009.

[14]   C. Li, K. Potter, M. R. Wisnom, and G. Stringer, "In-situ measurement of chemical shrinkage of MY750 epoxy resin by a novel gravimetric method," *Composites Science and Technology,* vol. 64, pp. 55-64, Jan 2004.

[15]   A. S. f. T. a. M. (ASTM), "Standard test method for linear shrinkage of cured thermosetting casting resins during cure," *ASTM D2566-79*.

[16]   J. D. Russell, "Cure shrinkage of thermoset composites," *Sampe Quarterly,* vol. 24, pp. 28-33, Jan 1993.

[17]   Y. J. Huang and C. M. Liang, "Volume shrinkage characteristics in the cure of low-shrink unsaturated polyester resins," *Polymer,* vol. 37, pp. 401-412, Feb 1996.

[18]   R. R. Braga and J. L. Ferracane, "Contraction stress related to degree of conversion and reaction kinetics," *Journal of Dental Research,* vol. 81, pp. 114-118, Feb 2002.

[19]   S. J. Hwang and Y. S. Chang, "Isobaric cure shrinkage behaviors of epoxy molding compound in isothermal state," *Journal of Polymer Science Part B-Polymer Physics,* vol. 43, pp. 2392-2398, Sep 2005.

[20]   H. Ishida and H. Y. Low, "A study on the volumetric expansion of benzoxazine-based phenolic resin," *Macromolecules,* vol. 30, pp. 1099-1106, Feb 1997.

[21]   A. W. Snow and J. P. Armistead, "A simple dilatometer for thermoset cure shrinkage and thermal expansion measurements," *Journal of Applied Polymer Science,* vol. 52, pp. 401-411, Apr 1994.

[22]   V. Fano, I. Ortalli, S. Pizzi, and M. Bonanini, "Polymerization shrinkage of microfilled composites determined by laser beam scanning," *Biomaterials,* vol. 18, pp. 467-470, 1997.

[23]   W. D. Cook, M. Forrest, and A. A. Goodwin, "A simple method for the measurement of polymerization shrinkage in dental composites," *Dental Materials,* vol. 15, pp. 447-449, Nov 1999.

[24]   C. L. Thomas and A. J. Bur, "In-situ monitoring of product shrinkage during injection molding using an optical sensor," *Polymer Engineering and Science,* vol. 39, pp. 1619-1627, Sep 1999.

[25] S. H. Park, I. Krejci, and F. Lutz, "Consistency in the amount of linear polymerization shrinkage in syringe-type composites," *Dental Materials,* vol. 15, pp. 442-446, Nov 1999.

[26] M. Rosin, A. D. Urban, C. Gartner, O. Bernhardt, C. Splieth, and G. Meyer, "Polymerization shrinkage-strain and microleakage in dentin-bordered cavities of chemically and light-cured restorative materials," *Dental Materials,* vol. 18, pp. 521-528, Nov 2002.

[27] A. J. Hudson, S. C. Martin, M. Hubert, and J. K. Spelt, "Optical measurement of shrinkage in UV-cured adhesives," *Journal of Electronic Packaging,* vol. 124, pp. 352-354, 2002.

[28] H. Yu, S. G. Mhaisalkar, and E. H. Wong, "Cure shrinkage measurement of nonconductive adhesives by means of a thermomechanical analyzer," *Journal of Electronic Materials,* vol. 34, pp. 1177-1182, Aug 2005.

[29] I. M. Daniel, T. M. Wang, D. Karalekas, and J. T. Gotro, "Determination of chemical cure shrinkage in composite laminates," *Journal of Composites Technology & Research,* vol. 12, pp. 172-176, Fal 1990.

[30] A. Aggelopoulos and D. Karalekas, "Determination of cure shrinkage in SL layer built plates using lamination theory," *Advanced Composites Letters,* vol. 10, pp. 7-12, 2001.

[31] D. Karalekas and A. Aggelopoulos, "Study of shrinkage strains in a stereolithography cured acrylic photopolyrner resin," *Journal of Materials Processing Technology,* vol. 136, pp. 146-150, May 2003.

[32] A. B. Spoelstra, G. W. M. Peters, and H. E. H. Meijer, "Chemorheology of a highly filled epoxy compound," *Polymer Engineering and Science,* vol. 36, pp. 2153-2162, Aug 1996.

[33] S. A. Newman, G. Forgacs, B. Hinner, C. W. Maier, and E. Sackmann, "Phase transformations in a model mesenchymal tissue," *Physical Biology,* vol. 1, pp. 100-109, Jun 2004.

[34] A. A. Stolov, T. Xie, J. Penelle, and S. L. Hsu, "Simultaneous measurement of polymerization kinetics and stress development in radiation-cured coatings: A new experimental approach and relationship between the degree of conversion and stress," *Macromolecules,* vol. 33, pp. 6970-6976, Sep 2000.

[35] E. Riande, R. Diaz-Calleja, M. G. Prolongo, R. M. Masegosa, and C. Salom, "Polymer viscoelasticity," *Marcel Dekker Inc.,* 2000.

[36] J. Bicerano, "Prediction of polymer properties," *Marcel Dekker Inc.,* 2002.

[37] G. E. Dieter, H. A. Kuhn, and S. L. Semiatin, "Handbook of workability and process design," *ASM International,* 2003.

[38] H. Neubert, E. Bindl, M. Mehnert, H. Radel, and C. Linseis, "A high-speed interferometric dilatometer based on the inductive heating of a specimen," *Measurement Science & Technology,* vol. 20, p. 5, Apr 2009.

[39] M. Okaji, N. Yamada, and H. Moriyama, "Ultra-precise thermal expansion measurements of ceramic and steel gauge blocks with an interferometric dilatometer," *Metrologia,* vol. 37, pp. 165-171, 2000.

[40] H. Watanabe, N. Yamada, and M. Okaji, "Laser interferometric dilatometer applicable to temperature range from 1300 to 2000K," *International Journal of Thermophysics,* vol. 22, pp. 1185-1200, 2001.

[41] C. G. Tseng and Y. S. Jiang, "Optical interference dilatometer," *Measurement Science & Technology,* vol. 16, pp. 2114-2120, Oct 2005.

[42] P. Tsao, C. Huang, M. Li, B. Su, and N. Tsai, "Underfill Characterization for Low-k Dielectric / Cu Interconnect IC Flip-chip Package Reliability," *Electronic Components and Technology Conference,* vol. 54, pp. 767-769, 2004.

[43] Wunderlich, "Thermal analysis of polymeric materials," *Springer Berlin Heidelberg Media,* 2005.

[44] C. P. Wong, S. H. H. Shi, and G. Jefferson, "High performance no-flow underfills for low-cost flip-chip applications: Material characterization," *Ieee Transactions on Components Packaging and Manufacturing Technology Part A,* vol. 21, pp. 450-458, Sep 1998.

[45] K. C. Yung, B. L. Zhu, J. Wu, T. M. Yue, and C. S. Xie, "Effect of AlN content on the performance of brominated epoxy resin for printed circuit board substrate," *Journal of Polymer Science Part B-Polymer Physics,* vol. 45, pp. 1662-1674, Jul 2007.

[46] E. A. Grulke, "Polymer process engineering," *Prentice-Hall Inc., New Jersey,* 1994.

[47] C. F. Jasso, J. J. Martinez, E. Mendizabal, and O. Laguna, "Mechanical and rheological properties of styrene/acrylic gradient polymers," *Journal of Applied Polymer Science,* vol. 58, pp. 2207-2212, Dec 1995.

[48] J. R. Davis, "Tensile testing," *ASM International,* 2004.

[49]   J. Lange, S. Toll, J. A. E. Manson, and A. Hult, "Residual stress build-up in thermoset films cured above their ultimate glass transition temperature," *Polymer,* vol. 36, pp. 3135-3141, Aug 1995.

[50]   Y. M. Alexander and I. I. Avraam, *Rheology: Concepts, Methods and Applications*, 2006.

[51]   D. Adolf and J. E. Martin, "Time-cure superposition during cross-linking," *Macromolecules,* vol. 23, pp. 3700-3704, Jul 1990.

[52]   Y. Eom, L. Boogh, V. Michaud, P. Sunderland, and J. A. Manson, "Time-cure-temperature superposition for the prediction of instantaneous viscoelastic properties during cure," *Polymer Engineering and Science,* vol. 40, pp. 1281-1292, Jun 2000.

[53]   S. Markovic, B. Dunjic, A. Zlatanic, and J. Djonlagic, "Dynamic mechanical analysis study of the curing of phenol-formaldehyde novolac resins," *Journal of Applied Polymer Science,* vol. 81, pp. 1902-1913, Aug 2001.

[54]   W. F. Vandenbogert, D. J. Belton, M. J. Molter, D. S. Soane, and R. W. Biernath, "THERMAL-STRESS IN SEMICONDUCTOR ENCAPSULATING MATERIALS," *Ieee Transactions on Components Hybrids and Manufacturing Technology,* vol. 11, pp. 245-252, Sep 1988.

[55]   L. J. Ernst, G. Q. Zhang, K. M. B. Jansen, and H. J. L. Bressers, "Time- and temperature-dependent thermo-mechanical modeling of a packaging molding compound and its effect on packaging process stresses," 2003, pp. 539-548.

[56]   R. H. Krondorfer and Y. K. Kim, "Packaging effect on MEMS pressure sensor performance," *Ieee Transactions on Components and Packaging Technologies,* vol. 30, pp. 285-293, Jun 2007.

[57]   J. D. Ferry, "Viscoelastic Properties of Polymers," *John Wiley & Sons Ltd, New York, NY.,* 1980.

[58]   N. G. McCrum, C. P. Buckley, and C. B. Bucknall, "Principles of polymer engineering," *Oxford University Press, USA,* 1997.

[59]   W. Grellmann and S. Seidler, "Polymer testing," *Hanser Gardner Publications, Inc., Cincinnati,* 2007.

[60]   A. Nikonov, A. R. Davies, and I. Emri, "The determination of creep and relaxation functions from a single experiment," *Journal of Rheology,* vol. 49, pp. 1193-1211, Nov-Dec 2005.

[61] M. L. Williams, R. F. Landel, and J. D. Ferry, "MECHANICAL PROPERTIES OF SUBSTANCES OF HIGH MOLECULAR WEIGHT .19. THE TEMPERATURE DEPENDENCE OF RELAXATION MECHANISMS IN AMORPHOUS POLYMERS AND OTHER GLASS-FORMING LIQUIDS," *Journal of the American Chemical Society,* vol. 77, pp. 3701-3707, 1955.

[62] V. H. Kenner, B. D. Harper, and V. Y. Itkin, "Stress relaxation in molding compounds," 1997, pp. 821-826.

[63] R. Z. Li, "Time-temperature superposition method for glass transition temperature of plastic materials," *Materials Science and Engineering a-Structural Materials Properties Microstructure and Processing,* vol. 278, pp. 36-45, Feb 2000.

[64] W. K. Goertzen and M. R. Kessler, "Creep behavior of carbon fiber/epoxy matrix composites," *Materials Science and Engineering a-Structural Materials Properties Microstructure and Processing,* vol. 421, pp. 217-225, Apr 2006.

[65] D. Roylance, "Engineering viscoelasticity," *http://web.mit.edu/course/3/3.11/www /modules/visco.pdf,* 2001.

[66] R. Brown, "Handbook of polymer testing," *Rapra Technology Limited, UK,* 2002.

[67] W. W. Morey, C. W. Maier, and W. H. Glenn, "Fiber optic Bragg grating sensors," *Proceeding SPIE, Fiber Optics and Laser Sensors VII,* vol. 1169, p. 10, 1989.

[68] A. D. Kersey, M. A. Davis, H. J. Patrick, M. LeBlanc, K. P. Koo, C. G. Askins, M. A. Putnam, and E. J. Friebele, "Fiber grating sensors," *Journal of Lightwave Technology,* vol. 15, pp. 1442-1463, Aug 1997.

[69] K. O. Hill and G. Meltz, "Fiber Bragg grating technology fundamentals and overview," *Journal of Lightwave Technology,* vol. 15, pp. 1263-1276, Aug 1997.

[70] R. Gafsi and M. A. El-Sherif, "Analysis of induced-birefringence effects on fiber Bragg gratings," *Optical Fiber Technology,* vol. 6, pp. 299-323, Jul 2000.

[71] H. K. Kang, D. H. Kang, H. J. Bang, C. S. Hong, and C. G. Kim, "Cure monitoring of composite laminates using fiber optic sensors," *Smart Materials & Structures,* vol. 11, pp. 279-287, Apr 2002.

[72] T. H. T. Chan, L. Yu, H. Y. Tam, Y. Q. Ni, W. H. Chung, and L. K. Cheng, "Fiber Bragg grating sensors for structural health monitoring of Tsing Ma bridge: Background and experimental observation," *Engineering Structures,* vol. 28, pp. 648-659, Apr 2006.

[73]   A. Kenel, P. Nellen, A. Frank, and P. Marti, "Reinforcing steel strains measured by Bragg grating sensors," *Journal of Materials in Civil Engineering,* vol. 17, pp. 423-431, Jul-Aug 2005.

[74]   J. M. Lopez-Higuera, "Handbook of optical fibre sensing technology," *John Wiley & Sons Ltd, England,* 2002.

[75]   Q. Z. Sun, D. M. Liu, L. Xia, J. Wang, H. R. Liu, and P. Shum, "Experimental demonstration of multipoint temperature warning sensor using a multichannel matched fiber Bragg grating," *Ieee Photonics Technology Letters,* vol. 20, pp. 933-935, May-Jun 2008.

[76]   M. G. Xu, J. L. Archambault, L. Reekie, and J. P. Dakin, "DISCRIMINATION BETWEEN STRAIN AND TEMPERATURE EFFECTS USING DUAL-WAVELENGTH FIBER GRATING SENSORS," *Electronics Letters,* vol. 30, pp. 1085-1087, Jun 1994.

[77]   H. J. Patrick, G. M. Williams, A. D. Kersey, J. R. Pedrazzani, and A. M. Vengsarkar, "Hybrid fiber Bragg grating/long period fiber grating sensor for strain/temperature discrimination," *Ieee Photonics Technology Letters,* vol. 8, pp. 1223-1225, Sep 1996.

[78]   N. Tanaka, Y. Okabe, and N. Takeda, "Temperature-compensated strain measurement using fiber Bragg grating sensors embedded in composite laminates," *Smart Materials & Structures,* vol. 12, pp. 940-946, Dec 2003.

[79]   P. Sivanesan, J. S. Sirkis, Y. Murata, and S. G. Buckley, "Optimal wavelength pair selection and accuracy analysis of dual fiber grating sensors for simultaneously measuring strain and temperature," *Optical Engineering,* vol. 41, pp. 2456-2463, Oct 2002.

[80]   C. M. Lawrence, D. V. Nelson, J. R. Springarn, and T. E. Bennett, "Measurement of process-induced strains in composite materials using embedded fiber optic sensors," *Proceeding SPIE,* vol. 2718, pp. 60-67, 1996.

[81]   M. J. O'Dwyer, G. M. Maistros, S. W. James, R. P. Tatam, and I. K. Partridge, "Relating the state of cure to the real-time internal strain development in a curing composite using in-fibre Bragg gratings and dielectric sensors," *Measurement Science & Technology,* vol. 9, pp. 1153-1158, Aug 1998.

[82]   V. M. Murukeshan, P. Y. Chan, L. S. Ong, and L. K. Seah, "Cure monitoring of smart composites using Fiber Bragg Grating based embedded sensors," *Sensors and Actuators a-Physical,* vol. 79, pp. 153-161, Feb 2000.

[83] Y. B. Lin, K. C. Chang, J. C. Chern, and L. A. Wang, "The health monitoring of a prestressed concrete beam by using fiber Bragg grating sensors," *Smart Materials & Structures,* vol. 13, pp. 712-718, Aug 2004.

[84] M. Giordano, L. Nicolais, A. M. Calabro, S. Cantoni, A. Cusano, G. Breglio, and A. Cutolo, "A fiber optic thermoset cure monitoring sensor," 2000, pp. 523-530.

[85] M. Giordano, A. Laudati, M. Russo, J. Nasser, G. V. Persiano, and A. Cusano, "Advanced cure monitoring by optoelectronic multifunction sensing system," *Thin Solid Films,* vol. 450, p. 4, 2004.

[86] J. S. Leng and A. Asundi, "Real-time cure monitoring of smart composite materials using extrinsic Fabry-Perot interferometer and fiber Bragg grating sensors," *Smart Materials & Structures,* vol. 11, pp. 249-255, Apr 2002.

[87] P. Childs, A. C. L. Wong, N. Gowripalan, and G. D. Peng, "Measurement of the coefficient of thermal expansion of ultra-high strength cementitious composites using fibre optic sensors," *Cement and Concrete Research,* vol. 37, pp. 789-795, May 2007.

[88] S. H. McGee, "CURING CHARACTERISTICS OF PARTICULATE-FILLED THERMOSETS," *Polymer Engineering and Science,* vol. 22, pp. 484-491, 1982.

[89] P. K. Maji and A. K. Bhowmick, "Influence of Number of Functional Groups of Hyperbranched Polyol on Cure Kinetics and Physical Properties of Polyurethanes," *Journal of Polymer Science Part a-Polymer Chemistry,* vol. 47, pp. 731-745, Feb 2009.

[90] Z. H. Luo, L. H. Wei, W. W. Li, F. Liu, and T. Zhao, "Isothermal differential scanning calorimetry study of the cure kinetics of a novel aromatic maleimide with an acetylene terminal," *Journal of Applied Polymer Science,* vol. 109, pp. 525-529, Jul 2008.

[91] Z. Q. Zhang and C. P. Wong, "Modeling of the curing kinetics of no-flow underfill in flip-chip applications," *Ieee Transactions on Components and Packaging Technologies,* vol. 27, pp. 383-390, Jun 2004.

[92] W. W. Li, F. Liu, L. H. Wei, and T. Zhao, "Curing behavior study of polydimethylsiloxane-modified allylated novolac/4,4 '-bismaleimidodiphenylmethane resin," *Journal of Applied Polymer Science,* vol. 107, pp. 554-561, Jan 2008.

[93] L. Gonzalez, X. Ramis, J. M. Salla, A. Mantecon, and A. Serra, "Kinetic analysis by DSC of the cationic curing of mixtures of DGEBA and 6,6-dimethyl (4,8-dioxaspiro[2.5]octane-5,7-dione)," *Thermochimica Acta,* vol. 464, pp. 35-41, Nov 2007.

[94]   J. E. Mark, "Physical properties of polymers handbook," *Springer-Verlag New York, Inc.,* 2007.

[95]   M. L. Costa, E. C. Botelho, and M. C. Rezende, "Monitoring of cure kinetic prepreg and cure cycle modeling," *Journal of Materials Science,* vol. 41, pp. 4349-4356, Jul 2006.

[96]   Z. Q. Zhang, E. Beatty, and C. P. Wong, "Study on the curing process and the gelation of epoxy/anhydride system for no-flow underfill for flip-chip applications," *Macromolecular Materials and Engineering,* vol. 288, pp. 365-371, Apr 2003.

[97]   M. A. Stone, B. K. Fink, T. A. Bogetti, and J. W. Gillespie, "Thermo-chemical response of vinyl-ester resin," *Polymer Engineering and Science,* vol. 40, pp. 2489-2497, Dec 2000.

[98]   S. J. Han and K. K. Wang, "Analysis of the flow of encapsulant during underfill encapsulation of flip-chips," *Ieee Transactions on Components Packaging and Manufacturing Technology Part B-Advanced Packaging,* vol. 20, pp. 424-433, Nov 1997.

[99]   Y. He, "Chemical and diffusion-controlled curing kinetics of an underfill material," *Microelectronics Reliability,* vol. 45, pp. 689-695, Mar-Apr 2005.

[100]   X. Fernandez-Francos, J. M. Salla, A. Mantecon, A. Serra, and X. Ramis, "Crosslinking of mixtures of DGEBA with 1,6-dioxaspiro[4,4]nonan-2,7-dione initiated by tertiary amines. I. Study of the reaction and kinetic analysis," *Journal of Applied Polymer Science,* vol. 109, pp. 2304-2315, Aug 2008.

[101]   R. L. Pagano, V. M. A. Calado, F. W. Tavares, and E. C. Biscaia, "Cure kinetic parameter estimation of thermosetting resins with isothermal data by using particle swarm optimization," *European Polymer Journal,* vol. 44, pp. 2678-2686, Aug 2008.

[102]   A. Omrani, L. C. Simon, A. A. Rostami, and M. Ghaemy, "Cure kinetics, dynamic mechanical and morphological properties of epoxy resin-IM6NiBr2 system," *European Polymer Journal,* vol. 44, pp. 769-779, Mar 2008.

[103]   H. Y. Cai, P. Li, G. Sui, Y. H. Yu, G. Li, X. P. Yang, and S. Ryu, "Curing kinetics study of epoxy resin/flexible amine toughness systems by dynamic and isothermal DSC," *Thermochimica Acta,* vol. 473, pp. 101-105, Jul 2008.

[104]   D. C. Watts and A. J. Cash, "DETERMINATION OF POLYMERIZATION SHRINKAGE KINETICS IN VISIBLE-LIGHT-CURED MATERIALS - METHODS DEVELOPMENT," *Dental Materials,* vol. 7, pp. 281-287, Oct 1991.

[105] T. Attin, W. Buchalla, A. M. Kielbassa, and E. Hellwig, "Curing shrinkage and volumetric changes of resin-modifed glass ionomer restorative materials," *Dental Materials,* vol. 11, pp. 359-362, Sep-Nov 1995.

[106] M. V. Alonso, M. Oliet, J. Garcia, F. Rodriguez, and J. Echeverria, "Gelation and isoconversional kinetic analysis of lignin-phenol-formaldehyde resol resins cure," *Chemical Engineering Journal,* vol. 122, pp. 159-166, Sep 2006.

[107] D. J. O'Brien and S. R. White, "Cure kinetics, gelation, and glass transition of a bisphenol F epoxide," *Polymer Engineering and Science,* vol. 43, pp. 863-874, Apr 2003.

[108] H. Yu, S. G. Mhaisalkar, and E. H. Wong, "Observations of gelation and vitrification of a thermosetting resin during the evolution of polymerization shrinkage," *Macromolecular Rapid Communications,* vol. 26, pp. 1483-1487, Sep 2005.

[109] H. Yu, S. G. Mhaisalkar, E. H. Wong, and G. Y. Khoo, "Time-temperature transformation (TTT) cure diagram of a fast cure non-conductive adhesive," 2006, pp. 331-335.

[110] Z. Q. Zhang, T. Yamashita, and C. P. Wong, "Study on the gelation of a no-flow underfill through Monte Carlo simulation," *Macromolecular Chemistry and Physics,* vol. 206, pp. 869-877, Apr 2005.

[111] M. Kluppel and R. H. Schuster, "Structure and properties of reinforcing fractal filler networks in elastomers," *Rubber Chemistry and Technology,* vol. 70, pp. 243-255, 1997.

[112] D. B. Adolf, J. E. Martin, R. S. Chambers, S. N. Burchett, and T. R. Guess, "Stresses during thermoset cure," *Journal of Materials Research,* vol. 13, pp. 530-550, Mar 1998.

[113] K. M. Chen, D. S. Jiang, N. H. Kao, and J. Y. Lai, "Effects of underfill materials on the reliability of low-K flip-chip packaging," *Microelectronics Reliability,* vol. 46, pp. 155-163, Jan 2006.

[114] J. Lange, S. Toll, J. A. E. Manson, and A. Hult, "Residual stress build-up in thermoset films cured below their ultimate glass transition temperature," *Polymer,* vol. 38, pp. 809-815, Feb 1997.

[115] M. H. H. Meuwissen, H. A. de Boer, H. Steijvers, K. M. B. Jansen, P. J. G. Schreurs, and M. G. D. Geers, "Prediction of mechanical stresses induced by flip-chip underfill encapsulants during cure," *International Journal of Adhesion and Adhesives,* vol. 26, pp. 212-225, Jul 2006.

[116] M. L. Sham and J. K. Kim, "Experiment and numerical analysis of the residual stresses in underfill resins for flip chip package applications," *Journal of Electronic Packaging,* vol. 127, pp. 47-51, Mar 2005.

[117] D. G. Yang, K. M. B. Jansen, L. J. Ernst, Z. G.Q., W. D. v. Driel, H. J. L. Bressers, and X. J. Fan, "Prediction of process-induced warpage of IC packages encapsulated with thermosetting polymers," *Electronic Components and Technology Conference,* pp. 98-105, 2004.

[118] H. Yu, S. G. Mhaisalkar, E. H. Wong, and J. F. J. Caers, "Evolution of Mechanical Properties and Cure Stresses in Non-Conductive Adhesives Used for Flip Chip Interconnects," *Electronic Packaging Technology Conference,* pp. 468-472, 2004.

[119] F. T. S. Yu and S. Yin, "Fiber optic sensors," *Marcel Dekker Inc., New York,* 2002.

[120] X. M. Tao, L. Q. Tang, W. C. Du, and C. L. Choy, "Internal strain measurement by fiber Bragg grating sensors in textile composites," *Composites Science and Technology,* vol. 60, pp. 657-669, 2000.

[121] X. C. Li, F. Prinz, and J. Seim, "Thermal behavior of a metal embedded fiber Bragg grating sensor," *Smart Materials & Structures,* vol. 10, pp. 575-579, Aug 2001.

[122] D. A. Pereira, O. Frazao, and J. L. Santos, "Fiber Bragg grating sensing system for simultaneous measurement of salinity and temperature," *Optical Engineering,* vol. 43, pp. 299-304, Feb 2004.

[123] M. B. Reid and M. Ozcan, "Temperature dependence of fiber optic Bragg gratings at low temperatures," *Optical Engineering,* vol. 37, pp. 237-240, Jan 1998.

[124] A. Bertholds and R. Dandliker, "DETERMINATION OF THE INDIVIDUAL STRAIN-OPTIC COEFFICIENTS IN SINGLE-MODE OPTICAL FIBERS," *Journal of Lightwave Technology,* vol. 6, pp. 17-20, Jan 1988.

[125] Y. Okabe, N. Tanaka, and N. Takeda, "Effect of fiber coating on crack detection in carbon fiber reinforced plastic composites using fiber Bragg grating sensors," *Smart Materials & Structures,* vol. 11, pp. 892-898, Dec 2002.

[126] G. B. Hocker, "FIBEROPTIC SENSING OF PRESSURE AND TEMPERATURE," *Applied Optics,* vol. 18, pp. 1445-1448, 1979.

[127]   Y. Zhang, D. J. Feng, Z. G. Liu, Z. Y. Guo, X. Y. Dong, K. S. Chiang, and B. C. B. Chu, "High-sensitivity pressure sensor using a shielded polymer-coated fiber Bragg grating," *Ieee Photonics Technology Letters,* vol. 13, pp. 618-619, Jun 2001.

[128]   C. D. Rabil and J. A. Harrington, "Mechanical properties of hollow glass waveguides," *Optical Engineering,* vol. 38, pp. 1490-1499, Sep 1999.

[129]   F. Y. Tsai, T. N. Blanton, D. R. Harding, and S. H. Chen, "Temperature dependence of the properties of vapor-deposited polyimide," *Journal of Applied Physics,* vol. 93, pp. 3760-3764, Apr 2003.

[130]   D. Post, B. Han, and P. Ifju, "High sensitivity Moire," *Springer-Verlag New York, Inc.,* 1994.

[131]   X. Ramis, A. Cadenato, J. M. Morancho, and J. M. Salla, "Curing of a thermosetting powder coating by means of DMTA, TMA and DSC," *Polymer,* vol. 44, pp. 2067-2079, Mar 2003.